Assessing the sources, chemistry and trends of nitrogen oxides in the remote oceanic atmosphere

Anna Byrne Callaghan

Doctor of Philosophy

University of York
Chemistry

April 2025

Abstract

Nitrogen oxides (NO and NO_2, known as NO_x) are key species in the ozone cycle and thus indirectly affect the atmosphere's oxidising capacity, as ozone photolysis produces the hydroxyl radical, OH. In the tropical marine boundary layer (MBL), low emissions, high relative humidities and photochemical activity result in high OH production rates. Whilst it is important to understand the chemical processes that take place in the tropical MBL, this region is remote therefore mixing ratios are low and measurements are challenging.

NO_x has been measured at the Cabo Verde Atmospheric Observatory (CVAO) in the North Atlantic since 2006, using a high-sensitivity chemiluminescence instrument with low detection limits. The data processing steps used at the CVAO have been validated through comparison with those used at the Kennaook/Cape Grim Baseline Air Pollution Station in Tasmania. The long-term dataset from the CVAO was used to identify trends in NO_x mixing ratios, particularly the effects different air masses reaching the site have on NO_x values.

Photostationary state (PSS) analysis was performed on NO_2 and HONO measurements from the CVAO, revealing that our understanding of the chemistry in the remote MBL is incomplete. The underestimation of PSS NO_2 has been attributed to missing oxidants converting NO into NO_2, with measured peroxy radicals at the CVAO not sufficient to reconcile measured and PSS values. HONO PSS analysis indicates that the photolysis of particulate nitrate (pNO_3^-) is the main source of HONO in this environment, but more work needs to be done to determine the factors driving the enhancement of pNO_3^- photolysis compared to that of nitric acid.

Current NO_x mixing ratios are low enough that net ozone destruction is seen in the MBL, but understanding NO_x cycling over the oceans is necessary as increases in NO_x could result in a shift to an ozone production regime.

Contents

List of Acronyms

ACS absorption cross section.

AQD Air Quality Design.

ARNA Atmospheric Reactive Nitrogen over the remote Atlantic.

BLC blue light converter.

CE conversion efficiency.

CoV coefficient of variation.

cps counts per second.

CVAO Cabo Verde Atmospheric Observatory.

FAGE fluorescence assay by gas expansion.

GHG greenhouse gas.

GPT gas phase titration.

KCG BAPS Kennaook/Cape Grim Baseline Air Pollution Station.

LIF laser-induced fluorescence.

LOD limit of detection.

LOPAP Long Path Absorption Photometer.

MBL marine boundary layer.

MFC mass flow controller.

NCAS National Centre for Atmospheric Science.

NMB normalised mean bias.

PAG pure air generator.

PAN peroxyacetyl nitrate.

PBL planetary boundary layer.

PMT photomultiplier tube.

PSS photostationary state.

RH relative humidity.

SLR straight-and-level run.

STL seasonal and trend decomposition using Loess.

TROPOS Leibniz Institute for Tropospheric Research.

VOC volatile organic compound.

WDCRG World Data Centre for Reactive Gases.

WMO-GAW World Meteorological Organization-Global Atmospheric Watch.

ZA zero air.

List of Figures

List of Tables

Acknowledgements

I would like to thank my supervisors, Prof James Lee and Prof Lucy Carpenter, for their guidance during these three and a half years and for all the amazing opportunities they gave me during my PhD. I did not anticipate visiting four continents (five including a layover in Qatar) and the Arctic when I started this PhD, and I really appreciate all the unique opportunities I have been given.

I would also like to thank everyone in WACL for all their help during my PhD, I am grateful to have worked in such a friendly and supportive environment. In particular, I would like to thank the Cabo Verde team for all their support – the data presented in this thesis could not have been collected and analysed without Katie, Luis, Gisela, Shalini, Simone, Martyn, Matt, Jimmy or Beth, so a huge thank you to you all.

Another huge thank you to everyone who I got to work with during the SEANA and PEROXY research campaigns I went on. Special thanks needs to be extended to Roberto for teaching me how to use the LOPAP and offering support (both scientific and emotional) during my time working with that instrument.

I am grateful to the Wild Visiting Scholars Fund for funding my trip to visit Dr Ian Galbally, Dr Erin Dunne and Dr Emily Franklin at CSIRO in Melbourne. This was an incredible experience, during which I learnt a lot and got to visit some amazing places. I am grateful to everyone I met and collaborated with during this project.

Lastly, I would like to thank my family, my friends and Ross for being my support network. My parents and Sophie have always encouraged me and kept me grounded, my friends Georga and Susanna have cheered me on and inspired me from afar and my friends Beth, Loren, Rhi and Athina have been by my side through it all. Ross believed in me when I didn't believe in myself, and has been my rock. I honestly mean it when I say I could not have done this without all of you.

Author's declaration

I declare that this thesis is a presentation of original work and I am the sole author. This work has not previously been presented for an award at this, or any other, University. My contributions to each chapter are outlined below, with all sources acknowledged as References and all external contributions acknowledged in the text.

In Chapter 2, the instrument and the data processing described have been developed by the CVAO team working in the Wolfson Atmospheric Chemistry Laboratories. I was responsible for instrument management, data collection and processing between 2021 and 2024, and during this time I resolved instrumental issues and updated the treatment of measurement offsets and the processing code.

In Chapter 3, an original comparison of CVAO and KCG NO_x data is presented, with the data from KCG collected by scientists working at the Australian Nuclear Science and Technology Organisation (ANSTO), the Commonwealth Science and Industrial Research Organisation (CSIRO) and the University of Wollongong, as acknowledged in the chapter.

In Chapter 4, trends in NO_x data from the CVAO are presented. I performed all the analysis presented. Historical CVAO NO_x measurements (2006–2020) were carried out under the responsibility of previous CVAO staff (acknowledged in the NO_x dataset available from the World Data Centre for Reactive Gases (WDCRG)).

In Chapter 5, new HONO datasets, which I collected, are presented. The analysis performed and the results discussed were all carried out by myself, with external contributions acknowledged in the text.

Chapter 1

Introduction

The past ten years have been the warmest on record, with global mean temperatures rising above 1.5°C compared to pre-industrial levels for the first time in 2024 [1]. Wildfires, extreme weather events and flooding are becoming more frequent and severe as a result of global warming caused by greenhouse gases (GHGs) emitted when burning fossil fuels [2–4]. Anthropogenic emissions are also known to result in higher concentrations of air pollutants, including ozone (O_3), particulate matter with a diameter < 2.5 μm ($PM_{2.5}$), nitrogen dioxide (NO_2) and carbon monoxide (CO), with the adverse health effects following exposure to these species estimated to cause millions of excess deaths each year [5, 6].

In an increasingly polarised political landscape, where there is a growing scepticism surrounding expert credibility, the challenges of climate change and air pollution are two of the greatest that humanity has faced. Understanding the atmosphere's composition and chemical processes remains essential for addressing these challenges. Continuing to study the Earth's atmosphere and communicating clearly both with policymakers and the general public is necessary to ensure that scientific research informs critical decisions regarding fossil fuel emissions and their far-reaching impacts on both the Earth's climate and human health and well-being.

1.1 The atmosphere

The Earth's atmosphere is divided into five layers, characterised by specific altitude ranges and temperature profiles. The troposphere extends from the Earth's surface to between 6 and 20 km (20 km at the equator and 6 km at the

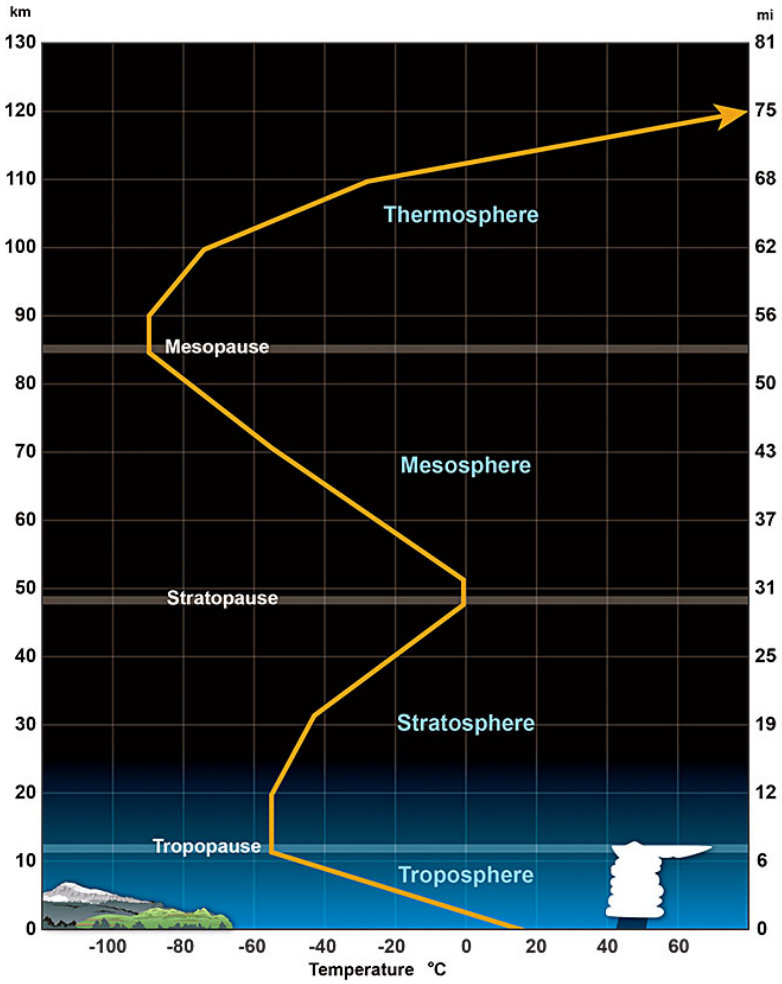

Figure 1.1: The five lower layers of the atmosphere and their average temperature profile (yellow arrow). Taken from NOAA [7].

poles). It is followed by the stratosphere ($\sim 12-50$ km), the mesosphere ($\sim 50-85$ km), the thermosphere ($\sim 85-600$ km) and the exosphere ($\sim 600-10,000$ km). The upper three atmospheric layers, despite being very thin, play a crucial role in absorbing high energy ultraviolet (UV) and x-ray radiation from the sun. The stratosphere and the troposphere are much denser, collectively containing roughly 99% of the atmospheric mass ($\sim 85-90\%$ in the troposphere and $\sim 10\%$ in the stratosphere) [8]. Biogenic and anthropogenic emissions can significantly impact the chemical processes that occur in these lower layers, as evidenced by the effects of chlorofluorocarbons (CFCs) on the stratospheric ozone layer and of air pollution on human health [9, 10].

1.1.1 Stratospheric ozone

In the stratosphere, the production and destruction of O_3 can be described by the Chapman cycle (R 1.1-R 1.5), which leads to the formation of the ozone layer [11].

$$O_2 + h\nu \longrightarrow 2\,O(^3P) \tag{R 1.1}$$

$$O(^3P) + O_2 + M \longrightarrow O_3 + M \tag{R 1.2}$$

$$O_3 + h\nu \longrightarrow O_2 + O(^1D) \tag{R 1.3}$$

$$O(^1D) + M \longrightarrow O(^3P) \tag{R 1.4}$$

$$O(^3P) + O_3 \longrightarrow 2\,O_2 \tag{R 1.5}$$

Early atmospheric chemistry research showed that nitrogen oxides and halogens were able to catalytically destroy O_3 (R 1.6-R 1.7, where X = Cl, Br, NO or OH) [9, 12, 13]. In particular, CFCs, which were commonly used in aerosols and refrigerants, have long atmospheric lifetimes and were thus able to reach the stratosphere, leading to the depletion of the O_3 layer. The UV radiation ($\lambda < 290$ nm) absorbed by O_2 and O_3 in the Chapman cycle is extremely harmful to human health, therefore the Montreal protocol was adopted in 1987 with the aim of phasing out the use of ozone depleting substances [14].

$$X + O_3 \longrightarrow XO + O_2 \tag{R 1.6}$$

$$XO + O \longrightarrow X + O_2 \tag{R 1.7}$$

1.1.2 The troposphere and atmospheric mixing

As the troposphere is the lowest layer of the atmosphere, it is most strongly influenced by the Earth's surface. The troposphere is divided into two sublayers, the planetary boundary layer (PBL), the altitude of which varies with meteorology but is typically below 1000 m, and the free troposphere [15]. As it is in direct contact with the Earth's surface, the PBL experiences large temperature variations and turbulent winds, which lead to strong vertical mixing. The free troposphere is instead more stable, with less diurnal temperature variations and less turbulent winds. Over the oceans, the marine boundary layer (MBL) is more stable than the terrestrial PBL, as water has a higher heat capacity than land and therefore

experiences less diurnal temperature variation.

Atmospheric gases that have lifetimes spanning years are well-mixed through the atmosphere. Notably, CFCs, with lifetimes over a decade, are able to reach the stratosphere and react with O_3 leading to the depletion of the ozone layer (section 1.1.1), and carbon dioxide (CO_2) and methane (CH_4) are both well-mixed in the atmosphere as a result of their long atmospheric lifetimes. Reactive trace gases generally have short atmospheric lifetimes (ranging from hours to weeks) and experience limited vertical mixing as they are removed from the atmosphere through chemical reactions or physical processes before they can reach the stratosphere. Despite this, these reactive trace gases, many of which are emitted directly from anthropogenic and biogenic sources, can undergo reactions leading to the formation of secondary pollutants and experience tropospheric transport prior to their removal, thus profoundly impacting tropospheric chemistry and potentially affecting human health, agriculture and ecosystems [15].

1.2 Tropospheric oxidation chemistry

The hydroxyl radical, OH, is a key tropospheric oxidant able to react with pollutants and GHGs in what is referred to as the atmosphere's self-cleaning cycle. The main source of OH is the photolysis of O_3, followed by the reaction between $O(^1D)$ and water vapour (R 1.8-R 1.9), which is particularly important in unpolluted remote environments. In urban polluted environments, the photolysis of nitrous acid (HONO) and of hydrogen peroxide (H_2O_2) can also be significant sources of OH (R 1.10-R 1.11).

$$O_3 + h\nu \longrightarrow O_2 + O(^1D) \quad \text{(R 1.8)}$$

$$O(^1D) + H_2O \longrightarrow 2\,OH \quad \text{(R 1.9)}$$

$$HONO + h\nu \longrightarrow OH + NO \quad \text{(R 1.10)}$$

$$H_2O_2 + h\nu \longrightarrow 2\,OH \quad \text{(R 1.11)}$$

1.2.1 The NO_x-O_3-VOC cycle

As described in section 1.1.1, the formation of stratospheric O_3 through O_2 photolysis requires UV radiation with wavelengths shorter than 290 nm. These wavelengths are absorbed by the stratospheric ozone layer and therefore only

wavelengths > 290 nm reach the troposphere, consequently preventing the Chapman cycle (R 1.1–R 1.5) from occurring within the troposphere. Some stratospheric O_3 enters the troposphere through stratosphere–troposphere exchange processes, but this represents a small fraction of total tropospheric O_3 [16].

The majority of tropospheric O_3, particularly in the PBL, is produced through the photolysis of NO_2 and the subsequent reaction of $O(^3P)$ with O_2 (R 1.12–R 1.13). The reaction between NO and O_3 regenerates NO_2 (R 1.14). If there were no other route for NO to be converted into NO_2, reactions R 1.12–R 1.14 would be in equilibrium and there would be no net production or destruction of O_3 in the troposphere.

$$NO_2 + h\nu \xrightarrow{j_{NO_2}} NO + O(^3P) \quad \text{(R 1.12)}$$

$$O(^3P) + O_2 + M \longrightarrow O_3 + M \quad \text{(R 1.13)}$$

$$NO + O_3 \longrightarrow NO_2 + O_2 \quad \text{(R 1.14)}$$

As mentioned above, OH oxidises many atmospheric gases, including CO (R 1.15) and CH_4 (R 1.16). These reactions produce the hydroperoxy radical, HO_2 (also referred to as the hydroxy radical) and the methylperoxy radical, CH_3O_2, respectively. OH can also react with volatile organic compounds (VOCs) (R 1.17), including alkanes, alkenes and aromatics, to make an organic peroxy radical, RO_2, where R depends on the VOC that was oxidised.

$$CO + OH \xrightarrow{O_2} CO_2 + HO_2 \quad \text{(R 1.15)}$$

$$CH_4 + OH \xrightarrow{O_2} CH_3O_2 + H_2O \quad \text{(R 1.16)}$$

$$RH + OH \xrightarrow{O_2} RO_2 + H_2O \quad \text{(R 1.17)}$$

HO_2 and RO_2 (including CH_3O_2) can oxidise NO to NO_2 (R 1.18–R 1.20), thus regenerating NO_2 without destroying O_3. As well as regenerating NO_2, these reactions both provide a pathway for the production of more HO_2 or RO_2.

$$NO + HO_2 \longrightarrow NO_2 + OH \quad \text{(R 1.18)}$$

$$NO + CH_3O_2 \longrightarrow NO_2 + CH_3O \quad \text{(R 1.19)}$$

$$NO + RO_2 \longrightarrow NO_2 + RO \quad \text{(R 1.20)}$$

Reaction R 1.18 produces OH, which can then oxidise CO, CH_4 or VOCs

into HO_2 or RO_2 as described above. The alkoxy radical, RO, formed in R 1.20, can undergo various reactive pathways, including isomerisation and reaction with O_2, resulting in the production of either HO_2 or RO_2 and a carbonyl.

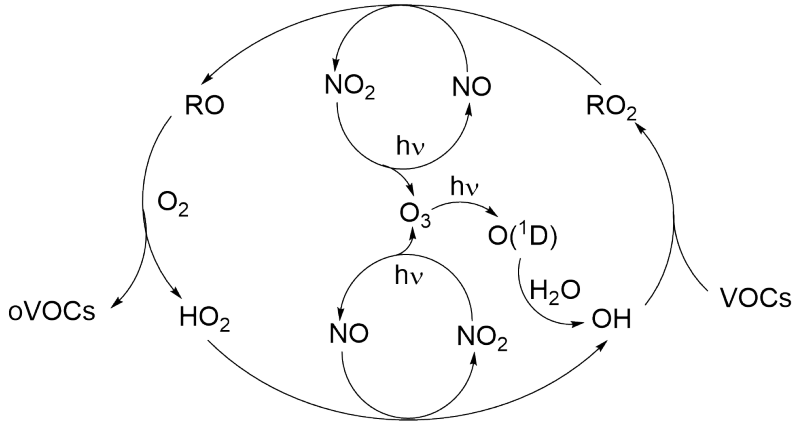

Figure 1.2: Catalytic reaction cycle between NO_x and peroxy/hydroxy radicals leading to the production of O_3 in the troposphere.

These reactions lead to the catalytic production of O_3 (figure 1.2), which is therefore dependent on the amounts of NO_x and VOCs present. The relationship between O_3, NO_x and VOCs is complex, and in polluted environments changes in NO_x and VOC mixing ratios can have different effects on O_3 mixing ratios depending on whether O_3 production is NO_x-limited or VOC-limited (also known as NO_x-saturated) [17]. In a NO_x-limited regime, as NO_x mixing ratios increase, the amount of O_3 increases, as more NO_2 can photolyse producing more O_3 (R 1.12–R 1.13). Once NO_x is in excess (in a VOC-limited regime), further increases in NO_x mixing ratios actually lead to a decrease in O_3 mixing ratios, because as the reaction between O_3 and NO (R 1.14) outcompetes NO_2 photolysis (R 1.12), the reaction between NO_2 and OH (R 1.21) becomes more significant and leads to the production of nitric acid, HNO_3, which through dry deposition acts as a sink for both NO_x and OH.

$$NO_2 + OH + M \longrightarrow HNO_3 + M \qquad \text{(R 1.21)}$$

1.2.2 Ozone cycling in the remote MBL

There are few direct sources of emissions over the oceans, therefore mixing ratios of many reactive trace gases are low due to their short atmospheric lifetimes. In the remote MBL, NO_x mixing ratios are typically tens of ppt [18, 19], compared

to mixing ratios of tens of ppb seen in urban environments [20–22]. As NO_x mixing ratios decrease, there is a switch from net O_3 production to net O_3 destruction, with reactions between HO_2 and RO_2 (R 1.22-R 1.24) taking place over reactions between NO and HO_2/RO_2 (R 1.18-R 1.20) [18, 23].

$$HO_2 + HO_2 + M \longrightarrow H_2O_2 + O_2 + M \quad \text{(R 1.22)}$$

$$RO_2 + RO_2 \longrightarrow ROH + R{=}O + O2 \quad \text{(R 1.23)}$$

$$HO_2 + RO_2 \longrightarrow ROOH + O_2 \quad \text{(R 1.24)}$$

$$OH + O_3 \longrightarrow HO_2 + O_2 \quad \text{(R 1.25)}$$

$$HO_2 + O_3 \longrightarrow OH + 2\,O_2 \quad \text{(R 1.26)}$$

As HO_2 and RO_2 are no longer converting NO to NO_2, the O_3-NO_x cycle (R 1.12-R 1.14) is a null cycle, therefore in this environment net O_3 destruction is seen [24]. O_3 destruction occurs through the photolysis of O_3 to produce OH (R 1.8-R 1.9), reactions between O_3 and OH (R 1.25) and HO_2 (R 1.26) and via catalytic halogen cycles (R 1.27-R 1.31, where X = I or Br) [25].

$$X + O_3 \longrightarrow XO + O_2 \quad \text{(R 1.27)}$$

$$XO + XO \longrightarrow 2\,X + O_2 \quad \text{(R 1.28)}$$

$$XO + HO_2 \longrightarrow HOX + O_2 \quad \text{(R 1.29)}$$

$$HOX + h\nu \longrightarrow OH + X \quad \text{(R 1.30)}$$

$$XO + NO \longrightarrow NO_2 + X \quad \text{(R 1.31)}$$

This halogen-mediated catalytic O_3 loss cycle also affects NO_x and HO_x (OH + HO_2) cycling in the tropical MBL. R 1.31 provides another pathway for the oxidation of NO into NO_2 (along with R 1.14, R 1.18 and R 1.20), though although it generates NO_2 without directly removing O_3, it does not result in net O_3 production as it also yields X which can remove O_3 (R 1.27). The reaction between XO and HO_2 (R 1.29) represents a significant sink for HO_x through the heterogeneous uptake of HOX (X = I or Br) though there is still uncertainty surrounding the magnitude of the uptake coefficient, γ_{HOX} [26, 27].

1.3 Nitrogen oxides

1.3.1 Global sources of nitrogen oxides

As discussed above, nitric oxide (NO) and nitrogen dioxide (NO_2), are commonly referred to as nitrogen oxides (NO_x) and are grouped together due to their rapid cycling (R 1.12-R 1.14). The sources of NO_x are both natural (lightning, wild fires and microbial soil activities) and anthropogenic (emissions during the combustion of fossil fuels and during biomass burning), with the majority of NO_x coming from fossil fuel combustion [28–31]. In its 2007 Physical Science Basis report, the Intergovernmental Panel on Climate Change (IPCC) estimates that in the 1990s NO_x emissions from fossil fuel combustion and industrial processes were 25.6 Tg N yr^{-1} (of this, between 0.5 and 0.8 Tg N yr^{-1} was from aviation), NO_x emissions from biomass burning were 5.9 Tg N yr^{-1}, NO_x emissions from soils were 8.9 Tg N yr^{-1} (1.6 Tg N yr^{-1} from agriculture and 7.3 Tg N yr^{-1} from natural soils) and NO_x emissions from lightning were between 1.1 and 6.4 Tg N yr^{-1} [32].

Work since then suggests than anthropogenic emissions are still the main source of NO_x in the atmosphere. Granier *et al.* compared different emission inventories between 1980 and 2010 and found that there is broad agreement in total anthropogenic NO_x emissions between the inventories (with a maximum difference between inventories of $\sim 20\%$), with all but one inventory showing a slight increase in NO_x emissions between 1990 and 2010 [33]. The 2021 Physical Science Basis IPCC report shows, however, that between 1996 and 2015 tropospheric NO_2 has been decreasing in Europe, North America and Japan. Following a peak in 2011, NO_2 in China is also decreasing, though in South Asia tropospheric NO_2 has doubled between 1996 and 2015 [34]. Despite these regional changes, the total global NO_x emissions in 2005 (47.9 Tg N) and in 2014 (47.5 Tg N) showed very little change [35].

As more countries start implementing stricter air quality legislation and anthropogenic NO_x continues to decrease, the relative importance of NO_x emissions from natural sources will increase. Estimates for NO_x emissions from lightning vary as uncertainty still surrounds the amount of NO_x produced per lightning flash, with recent work suggesting that global lightning NO_x emissions may be higher than previous estimates (~ 9 Tg N yr^{-1} compared to previously reported values between 2-8 Tg N yr^{-1}), due to higher NO_x emission rates per

lightning flash and shorter NO_x lifetimes in the region of outflow of thunderstorms [36–38]. NO_x emissions from soils are also hard to quantify as they are affected by many physical (temperature, pH, humidity) and biochemical factors, with recent estimates ranging from 7.9 Tg N yr^{-1} to 12.9 ± 3.9 Tg N yr^{-1} [35, 39–41].

1.3.2 Transport and atmospheric sinks of nitrogen oxides

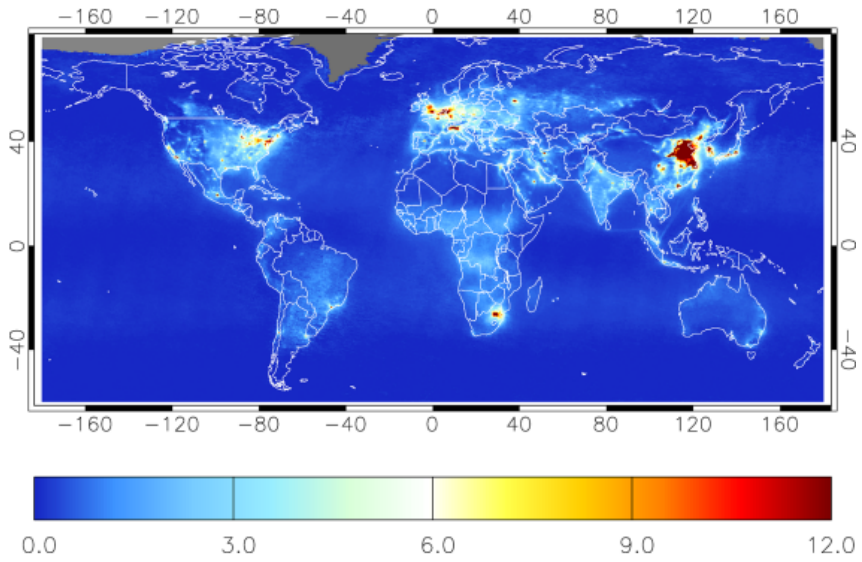

Figure 1.3: Mean tropospheric NO_2 vertical column density in 10^{15} molecules cm^{-2} between April 1996 and September 2017. Taken from Georgoulias *et al.* [42].

Figure 1.3 shows the NO_2 vertical column density across the globe, with clear hotspots in highly populated, industrialised areas, demonstrating that the highest NO_x mixing ratios are seen in urban environments. Direct NO_x sources over the oceans are limited to NO_x emissions by ships, with some studies also suggesting that NO_x can be photochemically produced in the sunlit ocean [43–46]. NO_x transport from polluted regions to the unpolluted, remote oceanic atmosphere is another important source of NO_x over the oceans. As NO_x has a short lifetime (0.5-2 days) in the PBL due to its reactivity, its transport mainly occurs through the conversion of NO_x into peroxyacetyl nitrate (PAN) [47]. PAN is an organic nitrate, formed following the oxidation of acetaldehyde by OH and then the reaction with NO_2 (R 1.32-R 1.34). Reactions between NO_2 and other RO_2 or RO species proceed in a similar manner and lead to the formation of other organic nitrates (respectively peroxyalkyl nitrates, $ROONO_2$, and alkyl nitrates,

$RONO_2$).

$$CH_3CHO + OH \longrightarrow CH_3CO + H_2O \quad \text{(R 1.32)}$$

$$CH_3CO + O_2 \longrightarrow CH_3C(O)OO \quad \text{(R 1.33)}$$

$$CH_3C(O)OO + NO_2 \underset{\Delta}{\rightleftharpoons} CH_3COO_2NO_2 \quad \text{(R 1.34)}$$

The low temperatures present in the upper troposphere lead to long atmospheric lifetimes for PAN, therefore NO_x that has been converted to PAN can be transported to the tropics, where, as temperatures increase with decreasing altitude, PAN thermally decomposes back into NO_2 (R 1.34) [48].

PAN and organic nitrates are reservoir species for NO_x, and as such convert back into NO_x under specific atmospheric conditions (thermal decomposition in the case of PAN and organic nitrates). NO_x reservoir species are often referred to as NO_z and include, as well as PAN and organic nitrates, nitric acid (HNO_3), nitrous acid (HONO), the nitrate radical (NO_3), dinitrogen pentoxide (N_2O_5). HONO is formed through the reaction between NO and OH (R 1.35), which are reformed following HONO photolysis (R 1.36).

$$NO + OH + M \longrightarrow HONO + M \quad \text{(R 1.35)}$$

$$HONO + h\nu \longrightarrow NO + OH \quad \text{(R 1.36)}$$

HNO_3 can be formed through reactions of NO_x with OH or HO_2 (R 1.37-R 1.38, however it is only a minor product from R 1.38, with NO_2 and OH the main products from this reaction), through the heterogeneous hydrolysis of N_2O_5 on sulfate aerosols (R 1.39) and through the reaction between NO_3 and aldehydes or dimethylsulfide, DMS (R 1.40-R 1.41) [49, 50].

$$NO_2 + OH + M \longrightarrow HNO_3 + M \quad \text{(R 1.37)}$$

$$NO + HO_2 + M \longrightarrow HNO_3 + M \quad \text{(R 1.38)}$$

$$N_2O_5 + H_2O \longrightarrow 2\,HNO_3 \quad \text{(R 1.39)}$$

$$NO_3 + RCHO \longrightarrow HNO_3 + RCO \quad \text{(R 1.40)}$$

$$NO_3 + (CH_3)_2S \longrightarrow HNO_3 + CH_3SCH_2 \quad \text{(R 1.41)}$$

N_2O_5 is formed following the reaction of NO_2 with NO_3 (R 1.42). NO_3 is

formed overnight in the absence of photolysis, through the reaction of NO_2 and O_3 (R 1.43). This reaction also occurs during the daytime, but NO_3 is rapidly photolysed and therefore cannot undergo reactions R 1.40–R 1.42. The reaction between NO_3 and VOCs (specifically unsaturated species) provides another pathway for the formation of organic nitrates (R 1.44) [24].

$$NO_2 + NO_3 + M \longrightarrow N_2O_5 + M \quad \text{(R 1.42)}$$

$$NO_2 + O_3 \longrightarrow NO_3 + O_2 \quad \text{(R 1.43)}$$

$$RCH{=}CH_2 + NO_3 \longrightarrow RCHCH_2ONO_2 \text{ or } RCH(ONO_2)CH_2 \quad \text{(R 1.44)}$$

As all these species rapidly react and interconvert in the troposphere, the sum of NO_x and NO_z is known as total reactive nitrogen, and is referred to as NO_y. Permanent loss pathways for NO_x occur through wet and dry deposition, either directly through the dry deposition of NO_2 on soils and vegetation or indirectly through both wet and dry deposition of NO_z species [50].

Whilst HNO_3 is technically a reservoir species for NO_x, as its photolysis yields NO_2 and OH, it has been traditionally considered the main atmospheric sink for NO_x, as it is removed from the troposphere though wet and dry deposition more rapidly than it photolyses back into NO_x [51]. Recent studies have however shown that unlike HNO_3, the photolysis of particulate nitrate, pNO_3^-, occurs on atmospherically relevant timescales and therefore pNO_3^- offers a pathway for NO_x recycling from HNO_3 in remote environments (discussed fully in chapter 5). Wet and dry deposition of organic nitrates can also represent a permanent sink for NO_x, however there is still a large amount of uncertainty surrounding this process, as different groups of organic nitrates have been shown to recycle to NO_x at different rates [52].

1.3.3 NO_x measurement techniques

NO_x measurement techniques can be divided into remote techniques and *in situ* techniques. Fourier-transform infrared (FTIR) spectroscopy, non-dispersive infrared (NDIR) spectroscopy and differential optical absorption spectroscopy (DOAS) are examples of remote measurement techniques for the detection of NO (NDIR and FTIR spectroscopy) and NO_x (DOAS). FTIR and NDIR spectroscopy rely upon a molecule's absorption band to identify it and since the absorption band of water vapour and NO_2 overlap, they cannot be used to measure NO_2.

The DOAS measurement technique was first described by Platt *et al.* and uses the Beer-Lambert law to detect NO and NO_2 based on their absorption spectra [53]. As these remote techniques rely on rely on well-characterised absorption cross sections, mixing ratios can be directly calculated using the Beer-Lambert law, without the need for calibration.

As opposed to remote measurement techniques, which don't require calibration, *in-situ* measurements of NO_x are relative and need to be frequently calibrated in order to convert the measured signal into mixing ratios. Frequent calibrations ensure that the measurements remain accurate across varying measurement conditions. These measurement techniques are most commonly used for the detection of NO_x, with the World Meteorological Organization-Global Atmospheric Watch (WMO-GAW) recommending the use of O_3 induced chemiluminescence detection (O_3-CLD, first described by Fontijn *et al.*) for the measurement of NO and photolytic conversion of NO_2 to NO, followed by O_3 induced chemiluminescence detection (PLC-O_3-CLD) for the measurement of NO_2 [54, 55]. As such, this method is used to measure the NO_x data collected in this study and is fully described in 2.

Other *in-situ* measurement techniques able to measure NO and NO_2 at low limit of detections (LODs) have been reported (summarised in table 1.1), but they are not recommended for use at WMO-GAW sites yet as their long-term monitoring capabilities have not been tested [55, 56].

Cavity ring-down spectroscopy (CRDS) can directly measure NO_2 by measuring the rate at which light intensity decays in an optical cavity containing two highly reflective mirrors [58]. Within the optical cavity, light from a laser with a specific wavelength (532 nm for NO_2) is reflected using the mirrors [57]. By turning off the laser, the decay in light intensity within the optical cavity can be measured and the rate at which this decay occurs can be used to determine how much of the light-absorbing molecule is in the optical cavity. CRDS has also been used to measure NO, however it is not able to reach the low LOD seen with other NO measurement techniques (Kostorev *et al.* report a LOD of 0.7 ppb) [62].

Laser-induced fluorescence (LIF) spectroscopy uses a laser to excite molecules to an excited state and measures the photons emitted by fluorescence as they relax back down to their ground state. This technique has been used to measure both NO and NO_2 by using different excitation laser wavelengths (215 nm for NO, 585 nm for NO_2) and as such is able to selectively detect NO and NO_2 without

Table 1.1: NO_x measurement techniques that have been identified as candidates for use at long-term monitoring sites by the WMO-GAW.

Measurement technique	Species measured	Limit of detection (integration time)	References
Chemiluminescence	NO	22 ppt (1 s)	This work
Photolytic NO_2 conversion followed by chemiluminescence	NO_2	25 ppt (1 s)	This work
Cavity ring-down spectroscopy (CRDS)	NO_2	40 ppt (1 s) [57]	O'Keefe and Deacon [58]
Laser induced fluorescence (LIF)	NO	1 ppt (1 s)	Rollins *et al.* [59]
	NO_2	15 ppt (10 s)	Thornton *et al.* [60]
Quantum cascade laser absorption spectroscopy (QCLAS)	NO	10 ppt (180 s)	Tuzson *et al.* [61]
	NO_2	3 ppt (180 s)	

interferences [59, 60].

Quantum cascade laser absorption spectroscopy (QCLAS) can directly measure NO and NO_2 at the same time by using two tunable narrow-linewidth mid-IR lasers, one emitting at around 1600 cm^{-1} (for NO_2 absorption lines at 1599.9 cm^{-1}) and one at around 1900 cm^{-1} (for NO absorption lines at 1900.1 cm^{-1}) [61]. Each laser beam is split into three, with the main beam being reflected multiple times to increase its effective path length before it is focused on an IR detector. The other two beams are used to identify the absorption lines, by passing through a reference cell containing a 1:1 mixture of NO and NO_2, and for accurate frequency tuning rate determination. Through the Beer-Lambert law, the absorption can be used to calculate the concentration of the absorbing species.

When measuring NO_x in the remote MBL, where mixing ratios are in the tens of ppt, challenges can arise both from an instrument's selectivity and its sensitivity. The use of lasers with specific wavelengths in CRDS, LIF and QCLAS enhances the instrument's selectivity to NO or NO_2, thus vastly reducing signal from interfering species. The chemiluminescence technique (fully described in chapter 2) is not as selective as these techniques, particularly for NO_2, because it

relies on the photolytic conversion of NO_2 to NO, typically using light in the 385-395 nm range. Other species, such as HONO, PANs and organic nitrates, are known to photolyse at the wavelengths used for NO_2 photolysis and can thus lead to positive measurement offsets (discussed further in section 2.2.5).

1.4 Summary

The hydroxyl radical, OH, is essential for the atmosphere's self-cleaning cycle, as it oxidises many trace gases, including air pollutants and GHGs. The main production pathway for OH, of particular importance in the unpolluted atmosphere, is the photolysis of O_3 and subsequent reaction with water vapour. The abundance of O_3 is controlled by the NO_x-O_3-VOC cycle, which can lead to the catalytic formation of O_3. In remote, unpolluted environments, NO_x mixing ratios are low enough for O_3 depleting reactions to dominate over O_3 producing reactions, resulting in net O_3 loss. An increase in NO_x mixing ratios can shift the regime from net O_3 destroying to net O_3 producing, therefore it is important to understand the sources, sinks and chemical processes that govern NO_x mixing ratios over the oceans. Figure 1.4 summarises the main NO_x sources and sinks and the key chemical reactions that take place in the remote MBL.

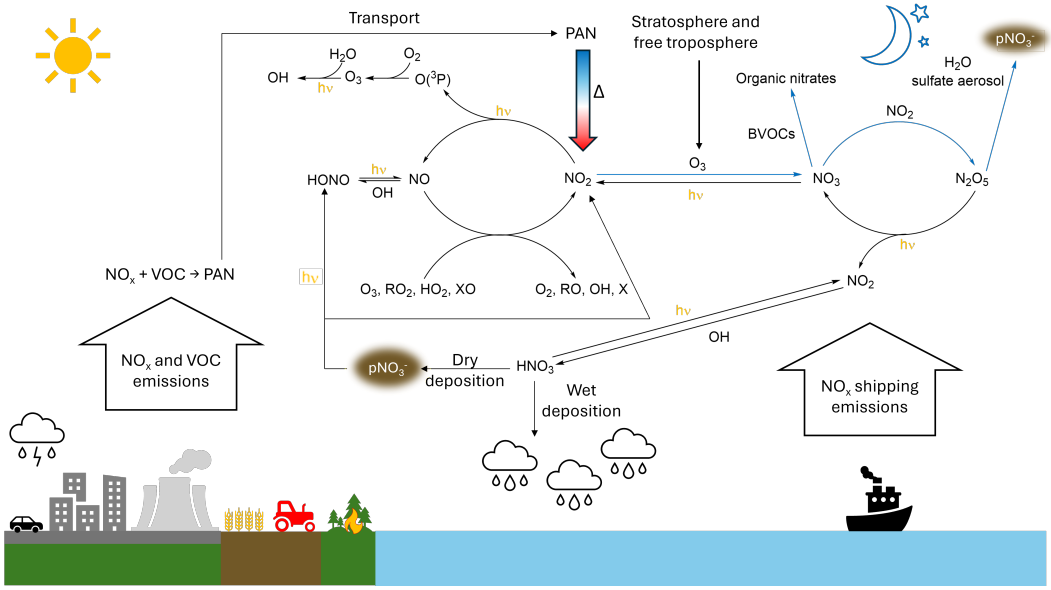

Figure 1.4: The main sources, sinks and reactions that characterise NO_x in the clean, remote MBL. Blue arrows represent processes that dominate at night.

1.5 Thesis outline

Chapter 2 describes the measurement of NO_x at the Cabo Verde Atmospheric Observatory (CVAO). The instrument, calibration routine and offset correction are presented, followed by an in-depth overview of the code used to process the NO_x data from raw counts (in Hz) to hourly averaged mixing ratios in ppt (parts per trillion). Limitations and future plans for NO_x measurements at the CVAO are discussed.

Chapter 3 compares the NO_x measurements made at the CVAO with those made at another WMO-GAW site, the Kennaook/Cape Grim Baseline Air Pollution Station (KCG BAPS) in Tasmania. The instruments and the data processing routines used at both sites are compared, and methods for measurement offset determination are discussed.

Chapter 4 examines trends in NO_x mixing ratios at the CVAO between 2012 and 2024, and looks at the differences in NO_x across different air masses that reach the CVAO. An NO_2 photostationary state (PSS) analysis is carried out, using measurements of NO_x, O_3 and photolysis rates, historical values of BrO and IO and box modelled values for HO_2 and RO_2. The effect of measuring NO extremely close to the instrument's LOD is discussed.

Chapter 5 presents two new measurements of HONO collected at the CVAO, in February 2023 and September 2024, which are compared to previous HONO measurements collected at the site. A PSS analysis is carried out, demonstrating that if the photolysis of pNO_3^- is not included as a source of HONO, mixing ratios are vastly underestimated. HONO production pathways through heterogenous NO_2 uptake and dust surface photocatalytic conversion are also considered, but were not found to be significant in this environment.

Chapter 6 summarises the key findings from the previous chapters and concludes by reiterating the importance of collecting long-term datasets of trace gases over the oceans, so that our understanding of the oxidation processes occurring in the MBL continues to improve.

Chapter 2

Measuring NO_x in the remote marine boundary layer: an overview of instruments and data processing

2.1 Introduction

Understanding the sources and sinks of NO_x in the remote marine boundary layer (MBL) is important, as discussed in chapter 1, as it leads to a better understanding of the factors affecting the atmosphere's oxidising capacity over the oceans. The low NO_x mixing ratios (tens of ppts) seen in the clean, unpolluted oceanic environment however are difficult to measure, and require specialised instrumentation with high sensitivity.

The Cabo Verde Atmospheric Observatory (CVAO) on the island of São Vicente in Cabo Verde is a World Meteorological Organization-Global Atmospheric Watch (WMO-GAW) station, unique as a site where long-term measurements of the unpolluted remote oceanic atmosphere over the tropical North Atlantic have been collected since 2006 [63]. At the CVAO, NO_x is measured using a chemiluminescence instrument with an hourly limit of detection (LOD) of around 1 ppt for NO and 2 ppt for NO_2, able therefore to collect a well-resolved dataset of NO_x over the oceans. Data collected at the CVAO is routinely submitted to the World Data Centre for Reactive Gases (WDCRG) and to the World Data Centre for Greenhouse Gases (WDCGG) and various publications present the

NO_x data collected at the site [18, 64–68].

This chapter focuses on the instrument and data processing used to measure NO_x at the CVAO, with the former described in section 2.2 and with section 2.3 giving the first detailed description of the NO_x processing steps used at the CVAO.

2.2 NO_x measurements at the Cabo Verde Atmospheric Observatory (CVAO)

2.2.1 Site Description

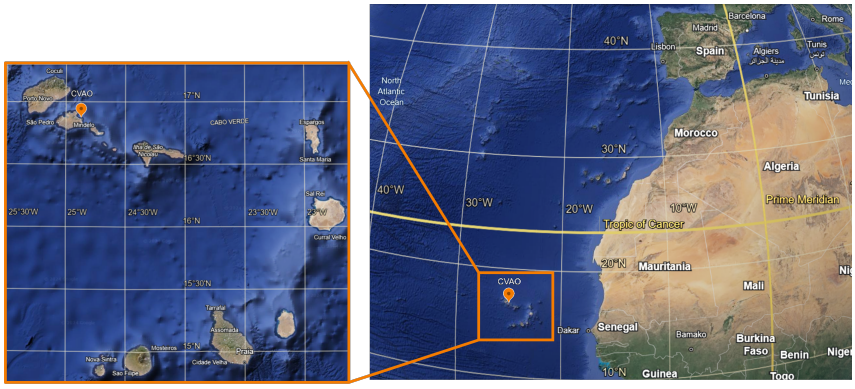

Figure 2.1: The Western Atlantic Ocean, with the location of Cabo Verde highlighted by the orange square. A zoomed in map of Cabo Verde shows the CVAO on the island of São Vicente.

The Cabo Verde Atmospheric Observatory (CVAO, 16° 51' 49" N, 24° 52' 02" W) is located on the island of São Vicente in Cabo Verde (figure 2.1), first described in Carpenter *et al.* [63]. The site is 10 m above sea level and is surrounded by volcanic rock, overlooking the Atlantic Ocean. The remote location of the CVAO ensures that there are no sources of pollution nearby, with the site sampling air from the ocean the majority of the time. When the wind direction is between 100° and 340°, the air travels over the island before reaching the CVAO and is therefore flagged as being impacted by local pollution. Instances where the wind speed is below 2 m s^{-1} are also flagged as being affected by local contamination (figure 2.2). Between October 2006 and December 2024, the site was sampling clean, marine air 95% of the time.

Backtrajectories of air masses sampled at the site show that the majority of

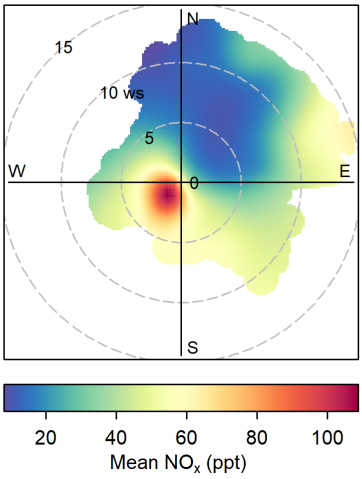

Figure 2.2: A polar plot coloured by NO_x mixing ratios measured at the CVAO between 2017 and 2024, highlighting that the lowest NO_x mixing ratios are seen when the wind is north-easterly as the air does not pass over the island of São Vicente.

the time the air sampled at the station has travelled over the North Atlantic Ocean and that the composition of the air masses reaching the site varies over the seasons (figure 2.3). In the autumn and winter months air masses have a stronger European and African influence, which results in Saharan dust reaching the CVAO and in higher mixing ratios of many species measured at the site. In the spring and the summer, the air masses are cleaner, with less continental influences and lower mixing ratios measured at the CVAO.

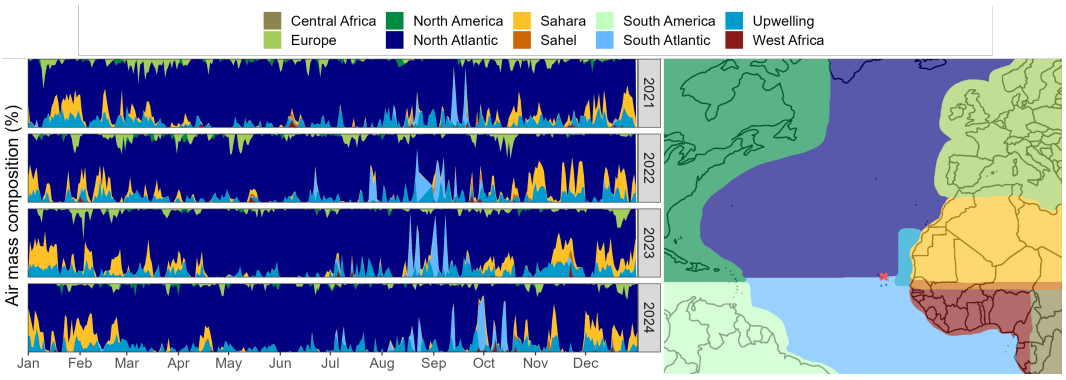

Figure 2.3: Daily average air mass compositions at the CVAO between 2021 and 2024. The map on the right defines the regions, with the red cross indicating the location of the CVAO.

The seasonality in the air masses reaching the CVAO is caused by seasonal changes in the subtropical anticyclone over the North Atlantic (known as the

Azores anticyclone) [63]. In the summer, the Azores anticyclone is concentrated over the North Atlantic, leading to north-easterly winds with limited African and European influence at the site, whereas in the winter the anticyclonic high pressure system extends from eastern North America to northwestern Africa resulting in air masses reaching the CVAO from Africa and Europe [69].

Table 2.1: Summary of the species measured at the CVAO, along with the instruments used, their 2σ hourly uncertainty and reference (see section 2.3.6 for information on NO_x uncertainty analysis).

Instrument	Measurement	2σ hourly uncertainty	Reference
Custom-built dual-channel AQD NO_x analyser	NO (ppt) NO_2 (ppt)	1.5 ppt 4.2 ppt	Andersen *et al.* [67]
Thermo Scientific 49i ozone monitor	O_3 (ppb)	0.07 ppb	Read *et al.* [25]
Picarro	CO (ppb) CO_2 (ppm) CH_4 (ppb)	1.0 ppb 45 ppb 0.3 ppb	Zellweger *et al.* [70, 71]
Dual channel gas chromatograph with flame ionisation detector	Ethane (ppt) Ethene (ppt) Acetylene (ppt) Propane (ppt) Propene (ppt) Iso-butane (ppt) n-butane (ppt) Iso-pentane (ppt) n-pentane (ppt) Benzene (ppt) Toluene (ppt) Methanol (ppt) Acetone (ppt)	5.2% 5.0% 10.7% 5.6% 6.9% 6.4% 5.0% 4.6% 6.4% 4.8% 6.3% 20.7% 12.2%	Steinbrecher [72]
Ocean Optics spectral radiometer QE650000	$j_{O(^1D)}$ (s^{-1}) j_{NO_2} (s^{-1}) j_{HONO} (s^{-1})	15% 15% 15%	Andersen *et al.* [68]
Campbell scientific automatic weather station	Temperature (°C) Pressure (hPa) Relative humidity (RH) (%) Solar radiation (W m^{-2})	0.4°C at 5-40°C 1.0 hPa at 0-40°C 2% at 10%-90% 5%	Carpenter *et al.* [63]

Table 2.1 gives an overview of the trace gas and meteorological measurements

collected at the CVAO by the University of York, supported by the National Centre for Atmospheric Science (NCAS), all of which are collected from the top of a 7.5 m tower. Aerosol and greenhouse gas (GHG) measurements are collected at the CVAO by the Leibniz Institute for Tropospheric Research (TROPOS) and by the Max Planck Institute, Jena (MPI), respectively, with the Instituto Nacional de Meteorologia e Geofisica (INMG) providing technical support.

2.2.2 Chemiluminescence

At the CVAO, NO_x is measured using a custom-built dual channel Air Quality Design (AQD) NO_x analyser. This instrument detects NO through chemiluminescence, first described as a measurement technique in Fontijn *et al.* [54]. The NO in the sampled air reacts with excess O_3 to produce excited state NO_2 (R 2.1), which can relax down to the ground state through two pathways, shown in R 2.2 and in R 2.3. Photons emitted by excited state NO_2 (R 2.2) can then be detected by a photomultiplier tube (PMT), with the signal being linearly proportional to the amount of NO in the sampled air. In order to maximise sensitivity and minimise quenching through molecular collision (R 2.3), which doesn't emit a photon, the pressure in the reaction chamber is kept low. Water vapour in particular is very efficient at quenching this reaction, leading to humidity controls being applied to chemiluminescence instruments to ensure that sampling and calibrations are carried out under the same conditions (either through drying the sampled air or through humidifying the calibration gas).

$$NO + O_3 \longrightarrow NO_2{}^* + O2 \tag{R 2.1}$$

$$NO_2{}^* \longrightarrow NO_2 + h\nu \tag{R 2.2}$$

$$NO_2{}^* + M \longrightarrow NO_2 + M \tag{R 2.3}$$

In order to detect NO_2, photolytic converters are used, which illuminate the sampled air with UV light, leading to photolysis of NO_2 to yield NO (R 2.4).

$$NO_2 + h\nu \longrightarrow NO + O \tag{R 2.4}$$

The NO in the sampled air and the NO produced from the photolysis of NO_2 are both detected by reaction with O_3 (R 2.1) followed by the emission of a photon as $NO_2{}^*$ relaxes down to the ground state (R 2.2), therefore the

amount of NO_2 in the sampled air is calculated by subtracting the amount of NO measured when the NO_2 converter is off.

2.2.3 Instrument set-up

The custom-built dual channel AQD NO_x analyser used at the CVAO is described in detail in Andersen *et al.* [67] and is summarised here. The diagram in figure 2.4 gives an overview of the instrument and its components.

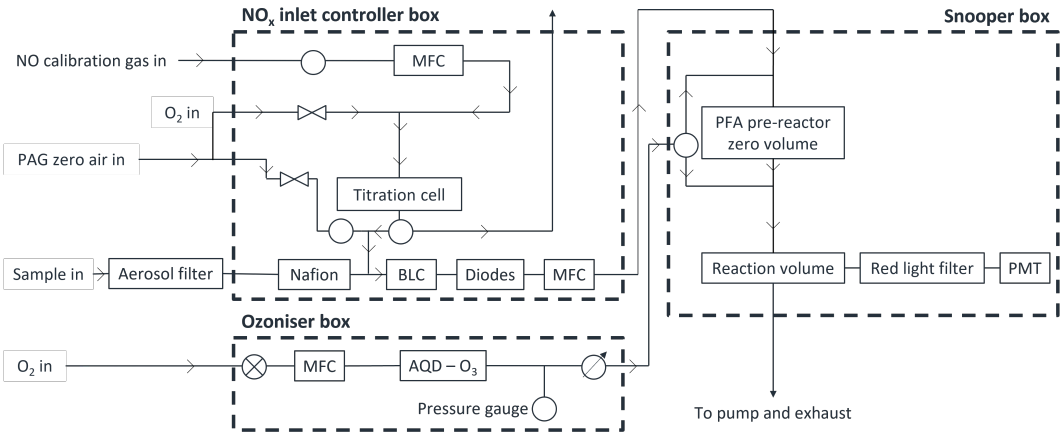

Figure 2.4: Schematic of the AQD NO_x analyser used at the CVAO to measure NO_x.

The inlet is located at the top of a 7.5 m tower and air is sampled through a glass manifold, used by all the instruments run by the University of York at the CVAO, with a pump flow rate of roughly 750 L min^{-1}. Dead-end traps are in place both inside and outside the lab to avoid dust, sea salt and condensation from reaching the instruments. Before the sampled air reaches the NO_x instrument, it passes through an aerosol filter (47 mm PTFE filter with a pore size of 1.3 μm) and is dried using a Nafion dryer (PD-50T-12-MKR, Permapure), which uses a flow of zero air from a pure air generator (PAG 003, Eco Physics AG) filtered through a Sofnofil (Molecular Products) and activated charcoal (Sigma Aldrich) trap (dew point -15° C). The Nafion is used to dry the sampled air to avoid large differences in humidity between the sampled air, the calibration gas and the zero air.

Once the sampled air reaches the instrument, its flow rate is set to 1000 mL min^{-1} by a mass flow controller (MKS, M100B) and it passes through two NO_2 converters, which are placed in series. The first of these is a commercially available blue light converter (BLC, λ= 385 nm, 3 W, LED Engin, Inc.) which

has been shown to have a significant measurement offset due to surface reactions on the porous, Teflon-like walls of its the photolysis cell [73]. The second NO_2 converter is a custom-built system (referred to as diodes) first described by Pollack *et al.* [74], which uses a quartz tube as the photolysis cell, illuminated on either end by two UV-LEDs (λ= 395 nm, Hamamatsu Lightningcure L11921-500). Measurement offsets due to surface reactions are avoided by using the quartz tube as the photolysis cell, therefore this NO_2 measurement is used as the official measurement, with the BLC NO_2 measurement simply used as a reference point.

After the NO_2 converters, the sampled air flows through the PFA pre-reactor zero volume (180 mL, PFA, Savillex, LLC) and then through the reaction volume (241 mL, aluminium with gold coating). A valve controls whether the sampled air will react with the O_3 generated by the ozoniser box (which generates excess O_3, with concentrations of 3%-4%) in the pre-reactor zero volume or in the reaction volume [75, 76]. By allowing NO and O_3 to react in the zero volume, a background measurement can be measured, as all the NO_2^* generated (R 2.1) will have relaxed down to ground state before reaching the PMT. The background measurement takes into account the signal seen from the PMT dark current, which is reduced by keeping the PMT cooled to -26° C (see section 2.2.6 for more information on the PMT temperature set-point), as well as the signal due to interferences from surface O_3 reactions. Both during background and ambient measurements, the sample passes through a red light filter (Schott RG-610) before reaching the PMT to avoid photons with λ> 600 nm being detected as these are not emitted by NO_2^*, but by alkenes reacting with O_3.

Whilst the instrument has two channels, currently only one is in use and measures NO_x in a 5-minute cycle, made up of 1 minute of background measurement, using the pre-reactor zero volume, 2 minutes of NO measurement, 1 minute of NO_x measurement using the BLC and 1 minute of NO_x measurement using the didoes.

2.2.4 Calibrations

Calibrations are carried out every 61 hours to ensure that, over a month, an equal number of calibrations occur during daytime and nighttime. In general, calibrating at the inlet is preferable, as it accounts for any line effects, however this not possible at the CVAO. The NO_x inlet control box (figure 2.4) contains the titration cell, which is used during conversion efficiency (CE) calibrations, and

would therefore have to be placed at the inlet in order for calibrations to occur at the inlet. Due to the high temperatures and direct sunlight experienced in Cabo Verde, the NO_2 converters, also housed in the NO_x inlet control box, would experience very high temperatures under these conditions, leading to an increase in thermal offsets (see section 2.2.5). Therefore calibrations are performed at the back of the instrument, rather than at the inlet.

Single-point calibrations are performed through standard addition to the sampled air, to minimise differences in temperature and humidity between the calibration gas and the ambient air. The NO calibration gas used (5 ppm, 8 mL min^{-1}) is added to the sampled air flow (1000 mL min^{-1}) resulting in a mixing ratio of NO during calibrations of roughly 40 ppb. This is much higher than the NO_x mixing ratios seen at the CVAO, however chemiluminescence is expected to behave linearly across these mixing ratios and working with cylinders with lower NO mixing ratios results in stability issues. As the ozone is well in excess (mixing ratios of between 3% and 4%), even during calibrations with significantly higher NO than is seen during sampling (40 ppb compared to a few ppt), there will not be significant consumption of O_3 in the reactor volumes.

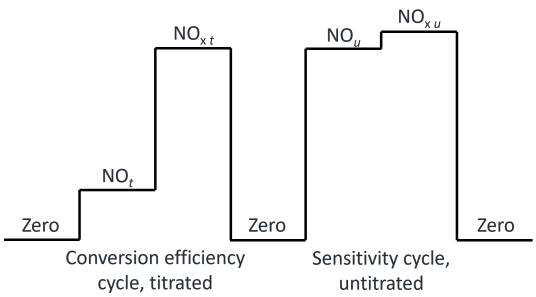

Figure 2.5: Diagram of the CE and sensitivity calibration cycles used to calibrate the CVAO NO_x instrument. NO_t and $NO_{x\ t}$ are measured during the titrated calibration cycle, NO_u and $NO_{x\ u}$ are measured during the untitrated calibration cycle.

Figure 2.5 shows a diagram of a titrated CE cycle followed by an untitrated sensitivity cycle. During titrated CE calibration cycles, O_2 and the NO calibration gas are exposed to UV lights in the titration cell (figure 2.4), which converts O_2 to O_3 and leads to a known amount of NO being converted into NO_2 (between 70% to 80% NO is titrated to NO_2 at the CVAO). The efficiency of the two NO_2 converters in use at the CVAO can then be measured by determining how much of the known NO_2 generated during the gas phase titration (GPT) is converted to NO, taking into account the small amount of NO_2 present in the NO cal gas

cylinder, as shown in equation 2.1.

$$\begin{aligned} \text{CE} &= \frac{\text{NO}_2 \text{ detected during cal} - \text{NO}_2 \text{ in cal gas}}{\text{NO}_2 \text{ created during GPT}} \\ &= \frac{(NO_{xt} - NO_t) - (NO_{xu} - NO_u)}{NO_u - NO_t} \end{aligned} \tag{2.1}$$

During untitrated sensitivity calibration cycles, a known amount of NO calibration gas is measured. The difference in signal between the untitrated calibration NO measurement and the NO measurement during the ambient cycle prior to the calibration is calculated and represents the increase in signal due to the addition of a known amount of NO. Dividing this difference by the NO calibration mixing ratio, as shown in equation 2.2, produces the instrument's sensitivity in counts per second (cps) ppt^{-1}.

$$\text{Sensitivity} = \frac{\text{NO cps during cal} - \text{NO cps before cal}}{\text{NO mixing ratio during cal}} \tag{2.2}$$

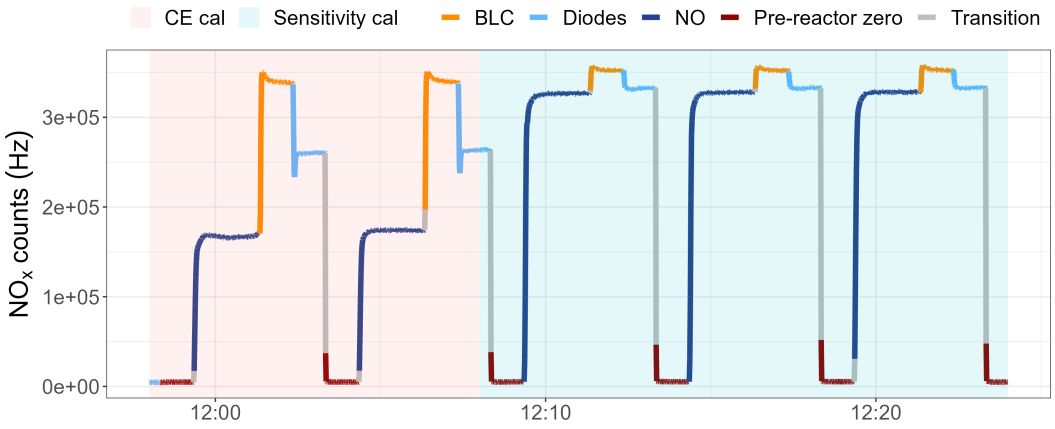

Figure 2.6: Plot of raw NO_x data from the CVAO AQD instrument during a calibration measured on the 3rd June 2024. The background has been shaded to indicate whether CE cycles (titrated) or sensitivity cycles (untitrated) are being measured. The colour of the line indicates what measurement is being collected.

A calibration cycle from the CVAO is shown in figure 2.6 and is made up of 2 titrated conversion efficiency cycles, followed by 3 untitrated sensitivity cycles. The NO calibration gas begins flowing 2 hours before a calibration starts, to condition the lines.

Conditions are generally stable and there is not much variation between calibrations, as shown in figure 2.7. The only issues encountered during this period are in the first half of 2023, when the diode CE was decreasing due to the

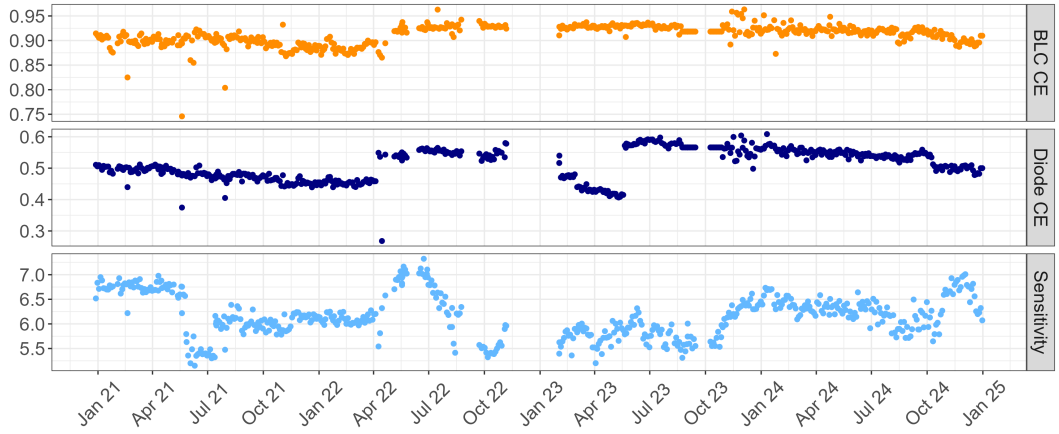

Figure 2.7: Timeseries of NO sensitivity (in cps ppt^{-1}) and of the CE for the BLC and the diodes from 2021 to 2024.

diodes being misaligned, and in mid-2023 (August to October) when, during the CE calibration, the GPT was converting all NO to NO_2, which was solved by increasing the flow of NO cal gas to 8 mL min^{-1}. During this period, the CE of the last normal calibration was used, as there is not a large amount of variability in the CE values.

2.2.5 Measurement offsets

Measurement offsets are accounted for in the NO_x AQD analyser both by measuring a pre-reactor zero for 1 minute at the start of each 5-minute cycle (as described in section 2.2.3) and by measuring the offset from 0 ppt when sampling NO_x-free air. Table 2.2 shows all the sources of offsets in NO_x measurements and describes how the offsets affect the measurements and how they are corrected.

In unpolluted environments, where there are no direct emissions of NO_x, NO values are roughly 0 ppt at night. Nighttime (between 21:00 and 04:00 local time) NO measurements are therefore used to quantify offsets due to O_3 reactions with alkenes at the same rate as NO, as well as the offsets caused by pressure differences between the pre-reactor and the reaction volumes. Nighttime NO values are chosen over NO values during PAG zero air measurements because they are carried out more frequently (every night as opposed to every 61 hours) and in the same air matrix as ambient measurements, so there are no discrepancies due to changes in humidity.

NO_2 mixing ratios are calculated by subtracting NO counts from NO_x counts, therefore NO offsets are removed from the NO_2 measurements. Table 2.2

Table 2.2: NO_x offsets seen at the CVAO using the NO_x AQD analyser, the effect these offsets have on the measurement and how their value can be determined.

Offset cause	Offset effect	Detection
O_3 reacting with alkenes at a different rate than NO	Positive NO offset	Pre-reactor zero
O_3 surface reactions	Positive NO offset	Pre-reactor zero
O_3 reacting with alkenes at the same rate as NO	Positive NO offset	NO_x-free air
Pressure difference between pre-reactor and reaction volumes	Positive or negative NO offset	NO_x-free air
Surface reactions in NO_2 converter	Positive NO_2 offset	NO_x-free air
NO_y thermal conversion in NO_2 converters	Positive NO_2 offset	NO_x-free air
NO_y photolytic conversion in NO_2 converters	Positive NO_2 offset	NO_x-free air

highlights three potential causes of NO_2 offsets. The offsets due to surface reactions occurring on the walls of the NO_2 converters only affect the BLC, as described in section 2.2.3.

Other potential offsets in the NO_2 measurements are due to NO_y compounds being thermally or photolytically converted to NO in the NO_2 converters. Previous work carried out by Reed *et al.* and by Andersen *et al.* has shown that due to the similarity between the ambient temperature at the CVAO and the temperature of the sampled air, as well as the fact that the NO_2 converters are only on for one minute in the five minute cycle, thermal interferences are expected to be minimal [68, 73].

In terms of photolytic interferences, HONO is the only species that both has an ACS that overlaps with the UV LEDs in use at the CVAO (λ= 385 nm for the BLC, λ= 395 nm for the diodes, figure 2.8) and is present in significant amounts (maximum measured midday values of HONO at the CVAO during the February 2023 campaign are roughly 25 ppt, see chapter 5) [68].

Using the ACS of HONO at 385 nm and assuming a conversion efficiency of 50% for the diodes, the photolytic offset due to HONO was calculated to be between 0.23 and 3.01 ppt, using the minimum and maximum midday (between 11:00 and 15:00 UTC) HONO mixing ratios measured during the February

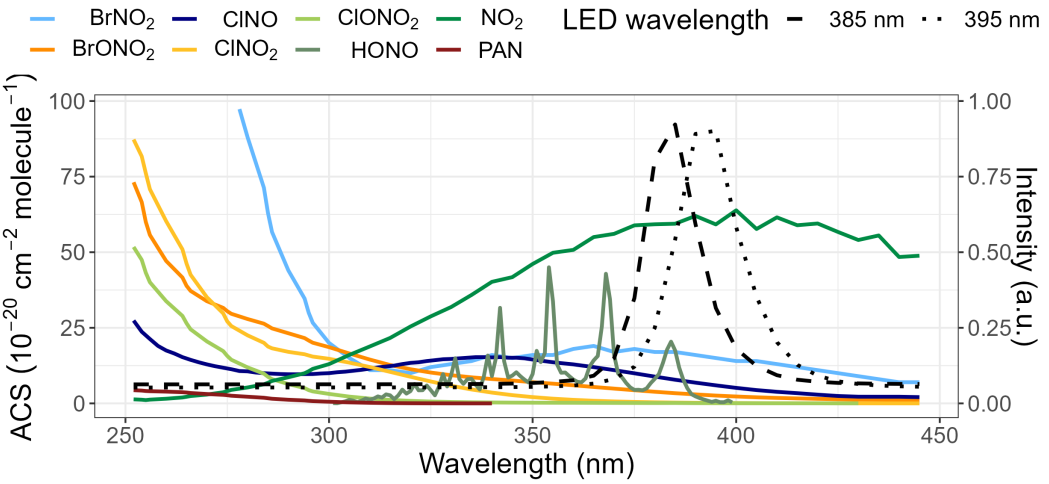

Figure 2.8: Plot of the absorption cross section (ACS) of NO_2 and potential photolytic interfering species (solid coloured lines), along with the spectral output of UV LEDs used at the CVAO (black dotted and dashed lines).

2023 campaign (fully discussed in chapter 5). These values do not account for the possibility of HONO being lost or produced through heterogeneous processes occurring in the sample lines and therefore only represent an estimate of the offset due to HONO, however at the low mixing ratios measured at the CVAO, the HONO offset could form a significant percentage of the measured NO_2.

Photolytic and thermal offsets cannot be determined using PAG zero air measurements, since it is impossible to remove NO_x and not also remove NO_y species. As a result, a new method was developed to account for these offsets, based on the assumption that over 30 days, there will be periods where the NO_2 mixing ratios at the CVAO are practically 0 ppt. This assumption replaces the previous assumption that measurements conducted using the diode system were completely free from interferences. As discussed above, while thermal and photolytic interferences are likely to be small, assuming that they are small enough to be negligible risks NO_2 mixing ratios being overestimated. While the assumption that periods where extremely low NO_2 mixing ratios are measured represent a measurement of interfering species could lead to the underestimation of NO_2 mixing ratios, utilising a rolling NO_2 minimum (median hourly data, window width = 30 days) to offset-correct NO_2 measurements does not lead to any difference in final NO_2 mixing ratios until the end of 2023, when instrumental issues led to a rise in the NO_2 baseline (figure 2.9). If the NO_2 minima method were not applied to offset-correct this data, it would show an erroneous increase

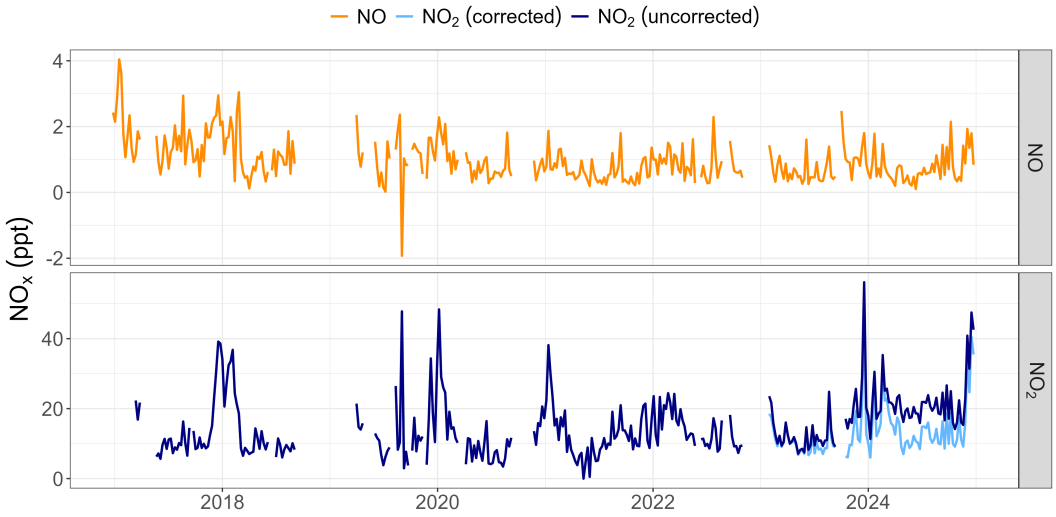

Figure 2.9: Weekly timeseries of NO and NO_2 from the CVAO. NO_2 data in dark blue has not been offset corrected, NO_2 data in light blue has been corrected using the 30-day rolling minima. Note that until the end of 2023, the corrected and uncorrected NO_2 mixing ratios are the same, and the light and dark blue lines overlap.

in NO_2 in the MBL. This would then affect the trends in NO_x (discussed in 4), making it appear that in the past two years there has been a dramatic shift in NO_x mixing ratios at the CVAO.

A comparison between the NO_2 minima and the PAG (measured every 61

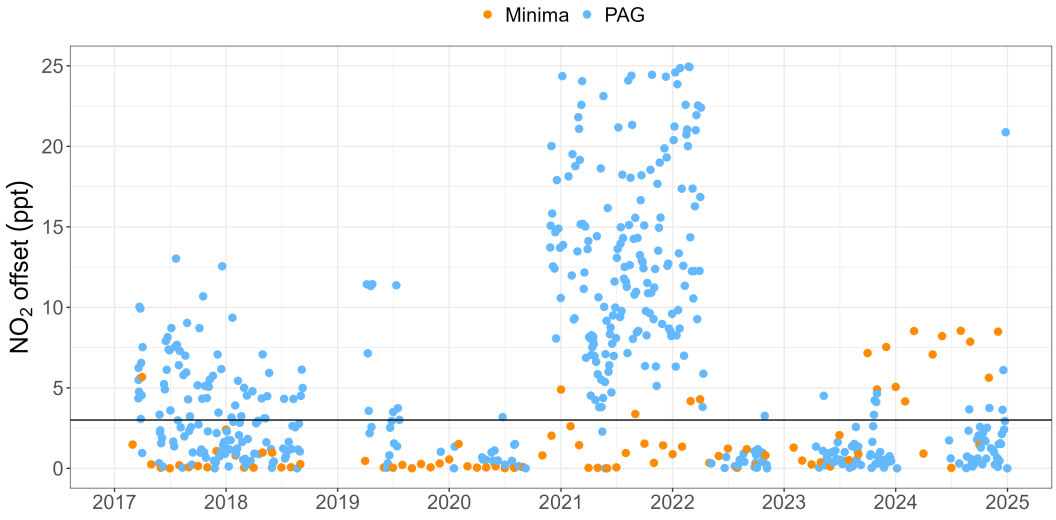

Figure 2.10: NO_2 offsets calculated using pure air generator (PAG) measurements (blue) and 30 day rolling minima (orange). The black line indicates the potential maximum HONO photolytic offset (3 ppt). Between 2021 and 2022, PAG values reached over 90 ppt, but are not shown in this plot.

hours) values is show in figure 2.10. As illustrated by this plot, the PAG can undergo instrumental issues, as in 2021, which would then affect the calculation of measurement offsets. The PAG values are also generally larger than the monthly NO_2 minima, thought to be because PAG air is not entirely free from NO_x. In comparison, prior to autumn 2023, NO_2 monthly minima are generally well below the calculated maximum value of photolytic interference (black line in figure 2.10). The jump in NO_2 monthly minima seen at the end of 2023 occurred after the instrument was turned off to replace the pump tip seals (discussed further in section 2.2.6) and is not seen in NO data. The baseline shift is corrected by applying this offset to the data (figure 2.9), showing that this is a valid method for quantifying offsets in the NO_2 diode measurements, whether they are caused by thermal or photolytic interferences or by instrumental issues.

2.2.6 Instrumental issues between 2021 and 2024

NO_x has been measured at the CVAO using the same AQD instrument since 2006. The instrument is generally stable, encountering only three major instrumental issues between 2021 and 2024, described below.

Loss of signal (November 2022-January 2023)

In November 2022, the instrument lost signal in both channels and had to be turned off until the end of January 2023. The PMT socket in one channel showed signs of water damage, which can occur if the instrument is turned off suddenly without giving the PMT time to return to room temperature (for example if a power cut occurs). Since the PMT is kept at around -30° C, the ice that forms melts if the change in temperature is too rapid and in this case had caused damage to the PMT socket, leading to a loss of signal. The instrument's second channel, which isn't currently used for measurements, had a working PMT socket, but a broken PMT, therefore the working PMT from the first channel was moved into the second channel, with the working PMT socket.

PMT temperature

In summer 2023, the lab temperature at the CVAO fluctuated a lot. As mentioned above, the PMT is cooled to around -30°C with a Peltier cooler, to minimise the interferences from PMT dark counts. The Peltier coolers in the instrument

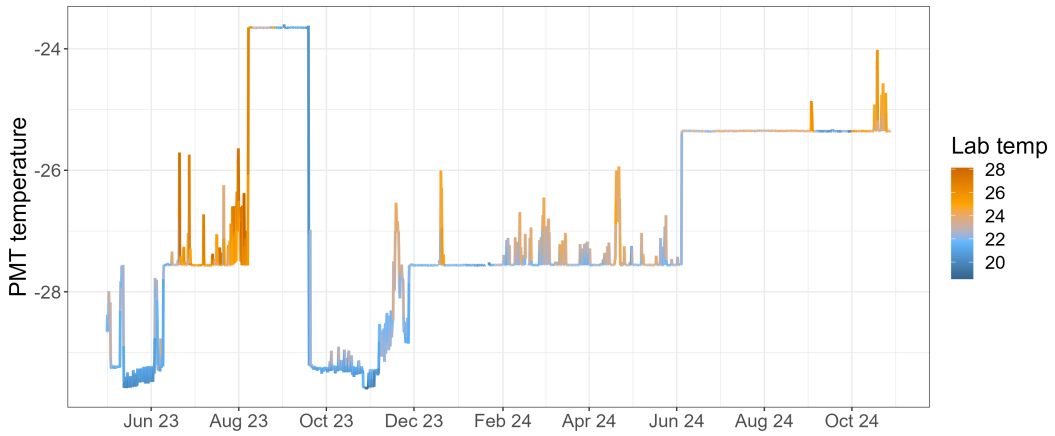

Figure 2.11: Plot of the variation of the PMT temperature from summer 2023 to autumn 2024, colour coded by the temperature in the lab.

have never been changed, running continuously for almost 18 years. Figure 2.11 shows a plot of the PMT temperature, highlighting that in June 2023, due to increases in the lab temperature, large diurnal variations were seen in the PMT temperature, which were mitigated by increasing the temperature set-point from -30°C to -28°C and then to -24°C. At the end of the summer months, the lab temperature was stable, therefore the PMT set-point was lowered back down to -30°C, however due to the age of the Peltier coolers, difficulties were encountered in maintaining a stable temperature. The set-point was once again increased to -28°C at the end of November 2023 and to -26°C in June 2024. PMT temperatures have remained stable across summer 2024, however with higher lab temperatures in October 2024, changes of over 1°C were seen on a

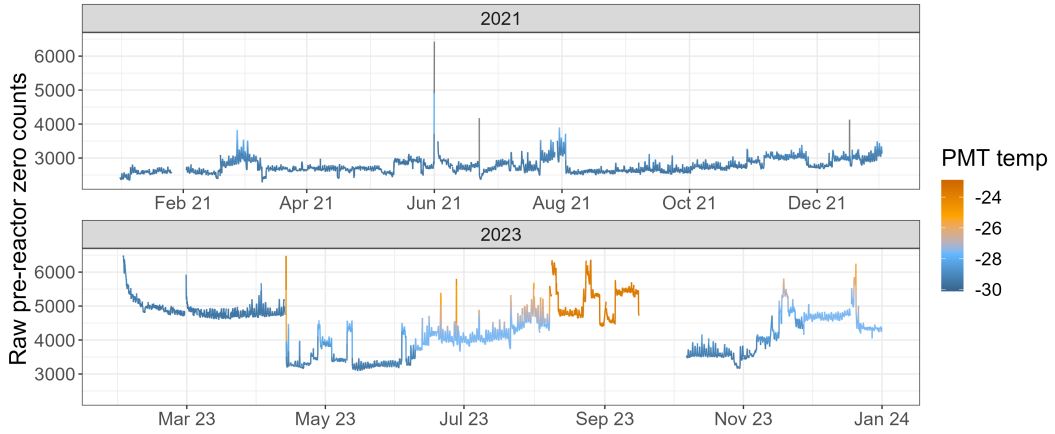

Figure 2.12: Hourly raw pre-reactor zero counts in 2021 and 2023, coloured by the PMT temperature.

few days.

If further increases in the PMT temperature set-point are required to maintain a stable temperature, the Peltier coolers will be replaced as higher PMT temperatures lead to increases in background dark counts, as shown in figure 2.12, resulting in a decrease in the instrument's sensitivity.

NO_2 baseline shift

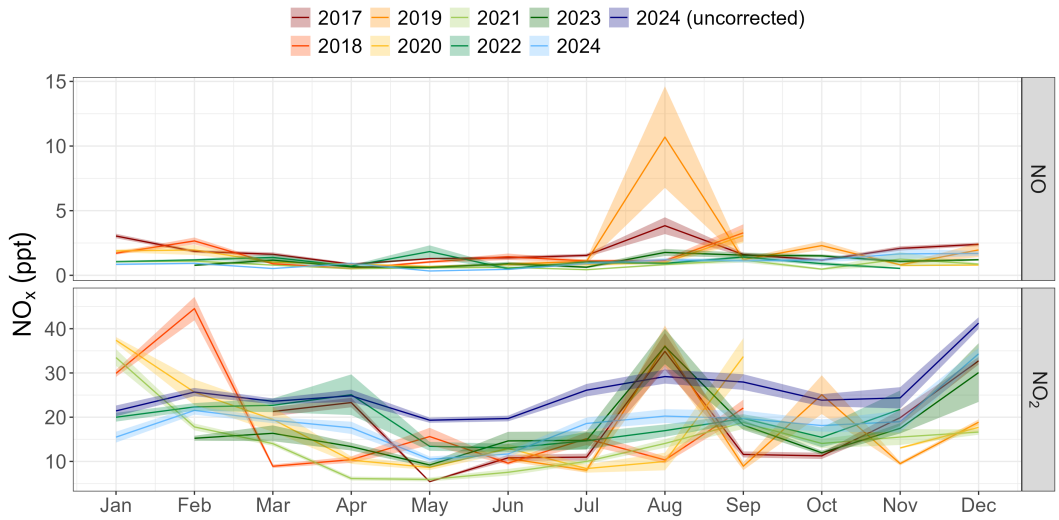

Figure 2.13: Monthly mean for NO and NO_2. For 2024, monthly NO_2 means are shown for the uncorrected data (dark blue) and for the data corrected as described in section 2.2.5 (light blue). Shaded area represents SE.

Following an increase in the reaction cell pressure, pump tip seals were replaced in September 2023. When the pump was turned back on, it overheated due to its fan not being properly connected. Once the pump was fixed, the NO_2 baseline was shifted higher, however NO measurements were unaffected, as shown in figure 2.13. The most likely cause is the introduction of a leak, which will be investigated during the next visit to the site. As discussed in section 2.2.5, the new NO_2 offset method is able to correct the shift in the NO_2 baseline.

2.3 CVAO NO_x processing code

2.3.1 Processing code overview

The aim of the NO_x processing code is to convert the raw 10 Hz data in cps to processed 5-minute data in ppt, accounting for the measurement offsets described in section 2.2.5, and removing data measured when the instrument was not

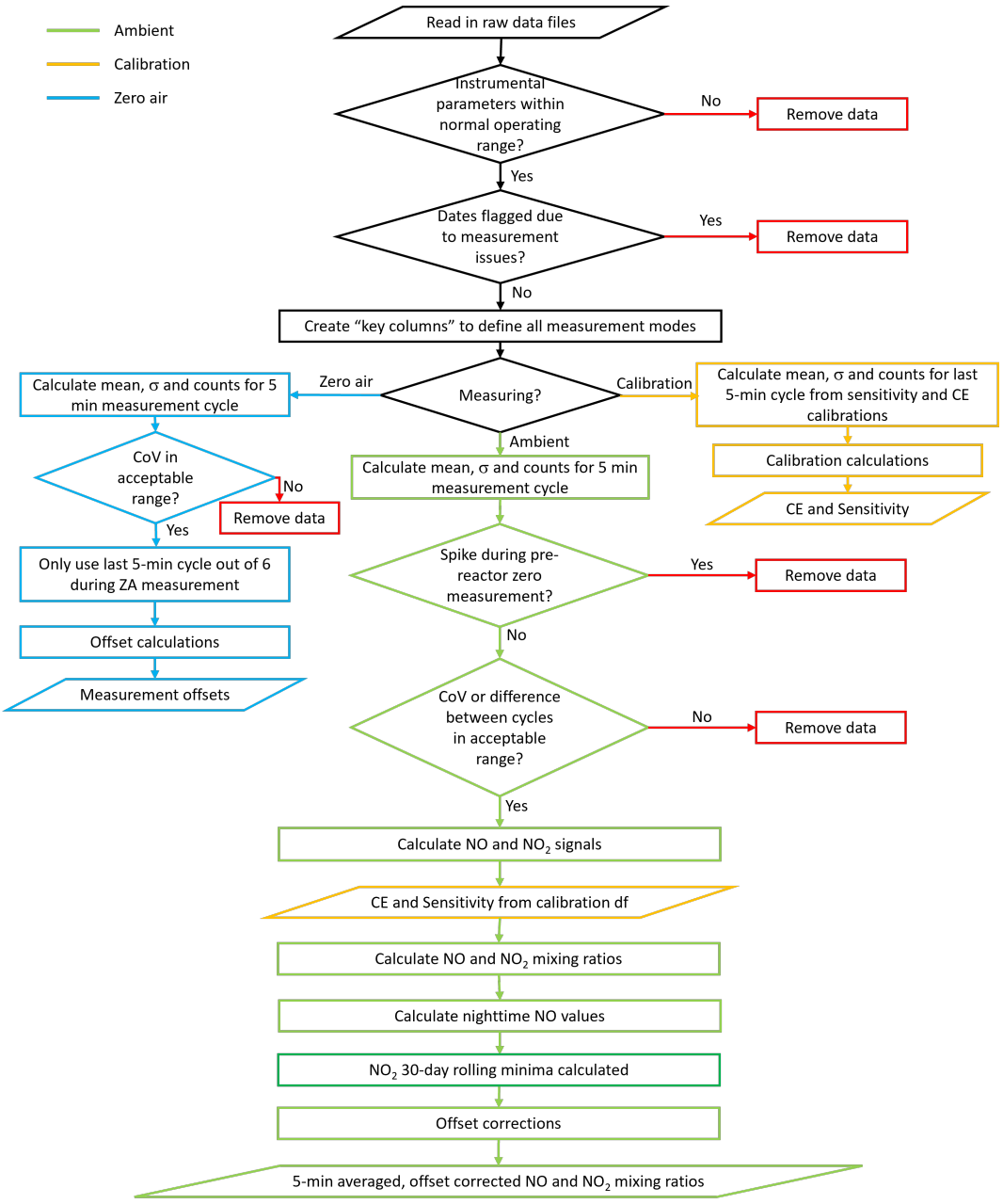

Figure 2.14: NO_x Python processing code flowchart.

running smoothly or when there were issues at the site. The code flowchart shown in figure 2.14 gives a step-by-step overview of how this is accomplished and what order the operations are performed within the processing code.

Daily raw data files are produced by the AQD NO_x instruments, which contain NO_x raw data in cps, instrumental parameters (flows, temperatures and pressures) and valve settings, which are used to identify what measurement mode the instrument is operating in (pre-reactor zero, NO or NO_x ambient, calibration or zero air measurement). Data processing is carried out in Python (the flowchart for the code is shown in figure 2.14), with further details regarding data filtering, calculations and offsets given in the following sections. The code runs automatically on JASMIN, a data intensive supercomputer operated by the Science and Technology Facilities Council (STFC) on behalf of the Centre for Environmental Data Analysis (CEDA) [77]. Raw data files are uploaded to JASMIN, where the processing code is stored and set to run overnight each night. Processed data files containing offset-corrected 5-minute averaged mixing ratios can then be downloaded from JASMIN and further processing steps, such as ozone corrections, hourly averaging and uncertainty analysis, are carried out, described in sections 2.3.5 and 2.3.6.

2.3.2 Data flagging and filtering

As shown in the code flowchart (figure 2.14, in red) data are filtered at various points during the processing. The first checks on the data are performed using instrumental parameters: if the PMT temperature is higher than a defined threshold (which has changed over the years as the PMT temperature set-point has changed, as discussed in section 2.2.6) or if the raw counts are below 0, the data point is removed. Dates when work was done on the instrument or there were issues at the site were also manually added to a digital notebook, which was then used to remove these periods.

For ambient measurements, the pre-reactor zero in each 5-minute cycle is checked to determine if there is a spike, in which case the whole cycle is flagged and removed from further analysis. Spikes are identified using a median filter (signal.medfilt from the SciPy package in Python, with a window width of 25). The median filter smooths the pre-reactor zero measurements, with only sharp spikes remaining, which are most likely due to outliers. The difference between the smoothed and non-smoothed values is calculated and if its absolute value is

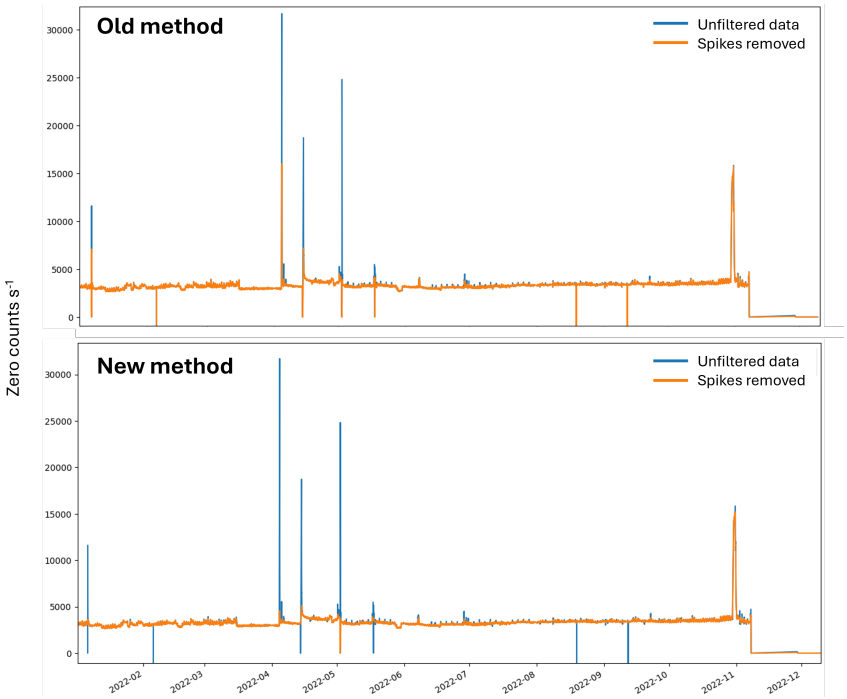

Figure 2.15: Pre-reactor zero counts from 2022 processed using the old and new methods of filtering data to identify spikes.

≥ 100, the cycle is removed due to a spike in the pre-reactor zero. In the past, this step was done without using the signal.medfilt function, and fewer outliers were flagged, as can be seen in figure 2.15.

Table 2.3: Coefficient of variation (CoV) and difference between subsequent cycles (mean $\pm 2\sigma$) between 2014 and 2019 for NO and zero, between 2017 and 2019 for NO_2.

Measurement	CoV (mean $\pm 2\sigma$)	Difference between subsequent cycles (mean $\pm 2\sigma$)
Pre-reactor zero	2.4 ± 1.7 cps	N/A
NO	2.5 ± 10.6 cps	0 ± 515 cps
NO_2 BLC	2.5 ± 7.5 cps	0 ± 1432 cps
NO_2 diodes	2.1 ± 2.5 cps	0 ± 738 cps

In order to remove outliers that have not already been identified using the methods above, both the coefficient of variation (CoV $= \frac{\sigma}{\mu}$) and the difference between subsequent measurement cycles are used. If either of these parameters for any of the measurements made within a 5-minute cycle (pre-reactor zero, NO or NO_2) falls outside the mean $\pm 2\sigma$ (summarised in table 2.3) calculated for data between 2014 and 2019 (2017 and 2019 for NO_2 measurements), the cycle is dropped. The CoV is also used to identify and remove outliers during PAG

zero air measurements, however the difference between subsequent cycles is not, since only the last cycle of three zero air cycles is used in analysis, in order to ensure that all NO calibration gas has been removed.

Figure 2.16: A comparison of how outliers affect the 5-minute averaged NO_x mixing ratios when processed with the code on JASMIN and an older iteration of the processing code.

The changes made to the data filtering led to better treatment of outliers compared to the previous iterations of the code, that were ran locally rather than on JASMIN (figure 2.15), which in turn results in better processed data, as shown in figure 2.16.

2.3.3 Calibration and mixing ratio calculations

In order to convert the data from cps to ppt, the sensitivity and conversion efficiency calculated during the calibration (using equations 2.2 and 2.1) are required. Firstly, the signal due solely to NO and the signal due solely to NO_2 are calculated. For NO, this is done by subtracting the pre-reactor zero measurement from the NO measurement (NO signal = NO cps − Pre-reactor zero cps), for NO_2, this is done by subtracting the NO measurement from the NO_x measurement (NO_2 signal = NO_x cps − NO cps). The mixing ratios of NO and NO_2 are then calculated as shown below in equations 2.3 and 2.4.

$$\text{NO mixing ratio (ppt)} = \frac{\text{NO}_{\text{signal}}}{\text{Sensitivity}_{\text{cps ppt}^{-1}}} \tag{2.3}$$

$$\text{NO}_2 \text{ mixing ratio (ppt)} = \frac{\text{NO}_{2\text{ signal}}}{\text{Sensitivity}_{\text{cps ppt}^{-1}} \times \text{CE}} \tag{2.4}$$

The last step in processing the data is subtracting the value of the offsets from the mixing ratios. A detailed description of how the offsets are measured both for NO and NO_2 is given in section 2.2.5. In summary, nighttime NO measurements are used to determine the NO offsets and are subtracted from the mixing ratio to give the offset-corrected NO mixing ratio. In order to avoid using nighttime NO measurements taken during nights when sampling local pollution, and therefore nights when the NO mixing ratio is not representative of the background, if the difference between subsequent nights is above the mean $\pm 2\sigma$ difference (0 ± 6.58 ppt) calculated between 2014 and 2019, the nighttime value is not used to calculate the NO offset. NO_2 measurements using the diode converter are offset corrected using the monthly minima values, as these are considered to be measurements made when NO_2 is 0 ppt and therefore represent the thermal and photolytic interferences in the system.

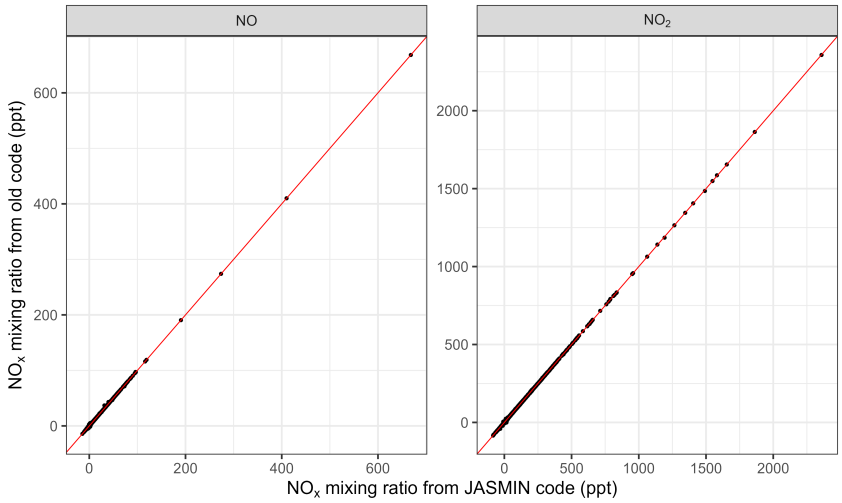

Figure 2.17: A comparison of NO_x mixing ratios calculated using the new and old processing codes, with all periods when an outlier was detected in either code removed. When the instrument is operating well, the codes yield very similar outputs.

The final output from the JASMIN NO_x processing code are the 5-minute average offset-corrected NO and NO_2 mixing ratios. The updated processing code on JASMIN, as shown in section 2.3.2, improves the way outliers are identified and treated, but it is important to note that the NO_x instrument is quite stable and when periods with outliers are removed, the output from the updated

code is very similar to that from the previous iteration, as expected (figure 2.17).

2.3.4 Spikes in processed data

During data processing, outliers are identified and removed from the NO_x data, as described in section 2.3.2, however the processed 5-minute data still contain some spikes in NO_x. These periods of higher NO_x are considered genuine, rather than caused by instrumental issues, and comparisons with met data measured at the CVAO show that often periods with higher NO_x occur when wind speeds are low (less than 2 m s^{-1}) or the wind direction is between 100° and 340°, resulting in local pollution from the island being sampled at the site.

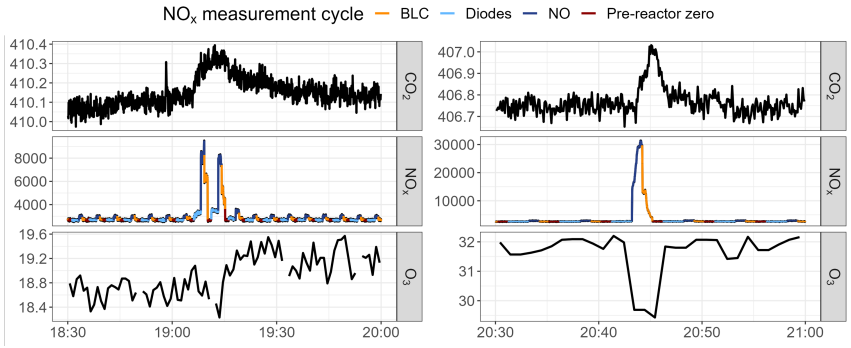

Figure 2.18: Raw CO_2 (ppm, minute data), O_3 (ppb, minute data) and NO_x (cps, 10 Hz) data from the 8th (LHS) and the 14th (RHS) August 2021, showing instances where a spike in NO_x corresponds to an increase in CO_2 and a decrease in O_3.

Comparing raw NO_x data (10 Hz) with raw O_3 data (1 minute) and raw CO_2 data (1 minute), as done in figure 2.18, shows that spikes in NO_x often occur at the same time as spikes in CO_2, and nighttime NO_x spikes are almost always accompanied by drops in O_3, due to NO_x titration of O_3. When these spikes occur whilst the site is sampling clean, marine air they are thought to be caused by emissions from small, local fishing vessels fitted with diesel engines (figure 2.19), the main pollutants from which are CO_2 and NO_x.

Daytime spikes in the processed NO_x data are not accompanied by a drop in O_3, since photolysis happens during the day, and sometimes do not correspond with a spike in CO_2 or periods of local pollution. In these cases, the increase in NO_x is still considered genuine, as no instrumental parameters have flagged the measurement, and could perhaps be due to emissions from larger ships, as some international shipping lanes from Europe to sub-Saharan Africa and South

Figure 2.19: Local fishing vessels on São Vicente, the emissions from which may be sampled at the site.

America pass near Cabo Verde, however investigating these spikes is outside the scope of this PhD project.

Table 2.4: The hourly mean ± 4σ and the difference between the hourly mean and median ± 4σ for NO and NO_2 measured using the diodes. These ranges are used to identify extreme values, which are flagged as such in the processed data.

Measurement	Difference between hourly mean and median (mean ± 4σ)	Hourly mean ± 4σ
NO	0.2 ± 4.1 ppt	1.7 ± 47.9 ppt
NO_2	1.7 ± 33.0 ppt	17.3 ± 176.8 ppt

Despite these spikes being considered genuine, they are not considered representative of the clean, marine background and therefore data are flagged when the hourly average is calculated. Flags are applied when the data coverage is less than 50% and when the measurements are considered to be extreme, such as when the difference between the hourly mean and median is above the mean ± 4σ of this difference calculated between 2014 and 2019 for NO and 2017 and 2019 for NO_2 and when the hourly mean is above hourly mean ± 4σ mixing ratio calculated between 2014 and 2019 for NO and 2017 and 2019 for NO_2 (table 2.4). Periods when met data indicate that local pollution is being sampled are also identified and flagged using wind speed and direction, as described above.

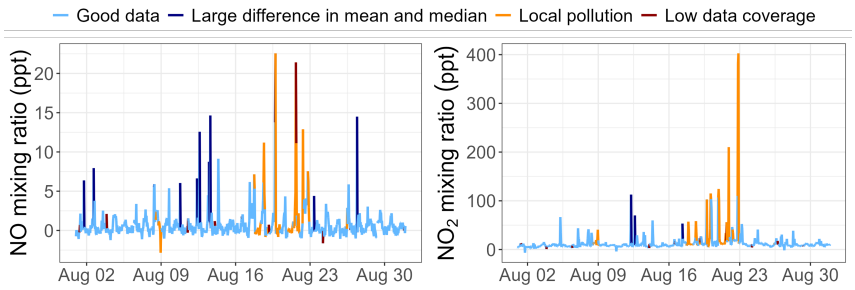

Figure 2.20: Hourly averaged NO_x data from August 2021, coloured by data flags.

Figure 2.20 shows the hourly averaged NO_x data from August 2021, which has been coloured by the flag applied to the data.

2.3.5 Ozone correction and data submission

The 5-minute averaged offset-corrected NO and NO_2 mixing ratios calculated using the processing code on JASMIN have not been O_3 corrected. The sample takes 4.3 s to travel from the inlet to the detector, with NO and O_3 still reacting in the lines producing NO_2, but, due to the absence of sunlight, NO_2 is not able to photolyse back to NO. When the NO_2 converters are turned on (residence time of 1 s in each converter), NO_2 is photolysed to NO, which can still react with O_3 to once again produce NO_2. These reactions need to be accounted for and corrected, so that the processed NO_x data reflect the mixing ratios at the inlet, rather than those measured at the detector.

The method used to perform the O_3 correction is described by Andersen *et al.* and, up until the 2023 data, the code for this step was ran locally before the yearly NO_x dataset from the CVAO is submitted to the WDCRG via ACTRIS (Aerosol, Clouds and Trace Gases Research Infrastructure), who are in charge of QA/QC [67].

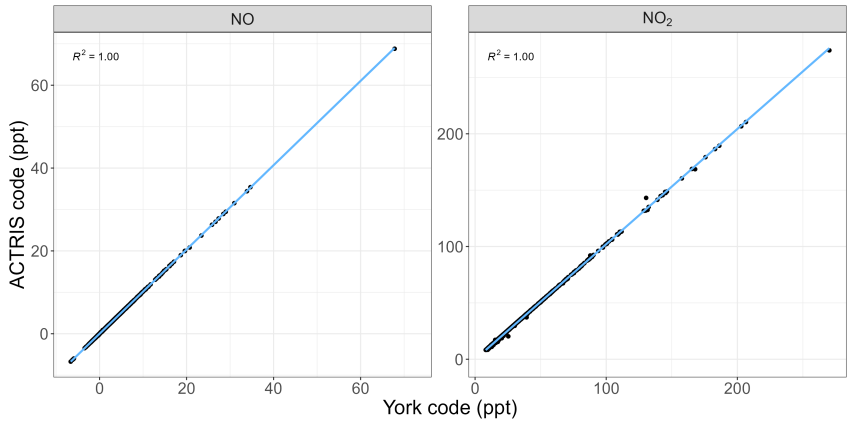

Figure 2.21: Comparison between the York and the ACTRIS O_3 corrected NO_x data from 2023.

Starting with 2023 data, ACTRIS has requested that the NO_x data submitted not be O_3 corrected, in order to ensure that the O_3 correction is being calculated in the same way by all the sites that submit data to the WDCRG. When the final O_3-corrected 2023 NO_x data were available on EBAS, it was compared to 2023

NO_x data that had been corrected using the local code to confirm that the ozone correction methods yield the same result (figure 2.21).

2.3.6 Uncertainty analysis

The uncertainty analysis for NO_x at the CVAO is fully described in the SI of Andersen *et al.* [67]. Briefly, the overall uncertainty associated with these measurements takes into account the precision of the instrument (used as the instrument's LOD, as it represents the noise around zero), the uncertainties associated with the calibrations, offset corrections and ozone corrections (eq. 2.5).

$$\text{Uncertainty} = \sqrt{\text{Precision}^2 + \text{Cal uncertainty}^2 + \text{Offset uncertainty}^2 + \text{O}_3\text{ corr uncertainty}^2} \tag{2.5}$$

The instrument's precision is calculated by determining the zero count variability over an hour: the mean pre-reactor background measurement for each hour is calculated, and then is subtracted from each pre-reactor background measurement in that hour. This results in an hourly frequency distribution of the PMT's photon-counting, which is Gaussian at high photon-counting rates [78]. In order to calculate the 1 second precision (2σ), the standard deviation is multiplied by two and divided by the sensitivity (and by the CE for NO_2). The hourly precision is calculated by dividing the 1 second precision by the square root of the number of data points available in the hour.

The uncertainties associated with the calibration, offset determination and O_3 correction are determined by combining all the sources of uncertainty associated with each of these calculations using error propagation. The final uncertainty associated with the NO and NO_2 measurements is then calculated using eq. 2.5.

Table 2.5 summarises the hourly LOD and the uncertainties for NO and NO_2 between 2021 and 2024. The increase in hourly LOD and uncertainty in 2023 and 2024 compared to 2021 and 2022 is likely due to the instrumental issues that were encountered at the end of 2022 and in the summer of 2023, which are described fully in section 2.2.6. Briefly, the PMT was moved to a different channel in January 2023 due to signal loss and over the summer of 2023 and the first half of 2024, the PMT temperature set-point was increased due to

difficulties in maintaining a stable temperature. PMT dark counts increase at higher temperatures, therefore the zero count variability was higher in 2023 and 2024 (shown in figure 2.12), which is used to calculate the LOD and in turn to calculate the uncertainty.

Table 2.5: Averages of hourly LODs and overall uncertainties for NO and NO_2 between 2021 and 2024.

Year	NO hourly LOD	NO_2 hourly LOD	NO uncertainty	NO_2 uncertainty
2021	0.82 ppt	1.67 ppt	1.06 ppt	3.57 ppt
2022	0.85 ppt	1.70 ppt	1.17 ppt	3.70 ppt
2023	1.03 ppt	2.19 ppt	1.37 ppt	3.74 ppt
2024	1.16 ppt	2.21 ppt	1.39 ppt	4.48 ppt

2.4 Summary, implications and future plans

The need for high sensitivity measurements of NO_x over the oceans has been discussed in chapter 1, and this chapter has presented the NO_x chemiluminescence instrument used at one of the only WMO-GAW stations measuring the remote MBL. The measurement technique, instrument set-up, calibrations and offset corrections were described in detail, highlighting the steps taken to minimise measurement interferences. Low hourly LODs (around 1 ppt for NO and 2 ppt for NO_2) have been achieved, though between 2017 and 2024 $\sim 46\%$ daytime (between 08:00 and 20:00 UTC) NO measurements were below the hourly LOD.

A new method to correct measurement offsets associated with the NO_2 diode measurement was presented, which relies on the assumption that near-zero ppt measurements of NO_2 at the CVAO represent the NO_2 measurement offset. These offsets are identified by using a 30-day rolling minima, and once applied showed that an increase in the NO_2 baseline measured in late 2023 and in 2024 was caused by an increase in measurement offsets and was not therefore a genuine increase in NO_2 over the oceans. The continual improvement of measurement and data processing techniques is essential when collecting datasets in remote environments with such low levels of NO_x, as a change of a few ppt in the measurement offsets can represent a large shift in mixing ratios, thus leading to the misinterpretation of trends in the data if not properly identified.

The detection and removal of outliers during data processing was updated and automated through the use of the SciPy signal.medfilt function to better identify outliers in the data caused by spikes that occurred during background measurements. A comparison between data from 2022 processed using the old and updated code confirmed that the addition of the signal.medfilt function allowed for more outliers (both positive and negative) to be removed. This step occurs early in the processing code, and is followed by further data filtering steps, which utilise the coefficient of variation, differences between subsequent cycles and extreme values thresholds (mixing ratio > 4σ mean calculated between 2014 and 2019) to flag and remove outliers. The previous iteration of the code therefore, while not able to capture the same number of outliers by flagging measurement cycles where there was a spike during background measurements as the updated version, was still able to detect outliers in the data using these thresholds. By detecting the outliers at an earlier stage of the processing, the updated version of the code is able to explain the reason for a larger proportion of outliers compared to previous iterations and is less reliant on data thresholds, which may change and need to be updated as NO_x mixing ratios in the remote MBL changes. Having fewer unexplained outliers will also help with future plans to study the outliers and their causes more extensively, with the aim of identifying the role small, local fishing vessels and air masses reaching the site having travelled over shipping lanes have on NO_x at the CVAO.

Future plans also include updating the NO_x instrument by setting up the second channel, which is currently not being used, to measure NO and an hourly pre-reactor zero, in order to increase the amount of NO data coverage over an hour and to better understand what causes spikes in the measured values. A NO measurement inter-comparison between the NO_x chemiluminescence instrument and an NO laser-induced fluorescence (LIF) instrument will also be carried out, as the LIF NO measurement technique is free from interferences and has extremely low LODs (0.3 ppt for 10 s integration time reported by Rollins *et al.*, described in section 4.3.1) [59].

Chapter 3

NO_x measurements at the Kennaook/Cape Grim Baseline Air Pollution Station (KCG BAPS)

3.1 Introduction

Like the Cabo Verde Atmospheric Observatory (CVAO), the Kennaook/Cape Grim Baseline Air Pollution Station (KCG BAPS) in Tasmania is a World Meteorological Organization-Global Atmospheric Watch (WMO-GAW) station that has been collecting long-term measurements of greenhouse gases (GHGs), trace gases, aerosols and meteorological data over the oceans for decades [79–81]. NO_x mixing ratios at KCG BAPS have been measured using an Air Quality Design (AQD) chemiluminescence instrument, similar to the one used at the CVAO (described in chapter 2), for over 15 years [82].

This chapter describes the KCG BAPS in section 3.2.1, before focusing on the NO_x instrument set-up at the site and the processing code used to analyse the data. Both the instrumental set-up and the data processing at KCG BAPS are discussed in relation to the instrument and processing used for the CVAO NO_x measurements, with section 3.2 comparing the instruments and section 3.3 comparing the processing codes. Lastly, section 3.4 discusses ongoing issues with measurement offsets at the KCG BAPS, specifically with NO measurement offsets, highlighting the difficulties encountered when measuring such low mixing ratios of NO_x.

3.2 KCG NO_x instrument

3.2.1 KCG BAPS site description

The Kennaook/Cape Grim Baseline Air Pollution Station (KCG BAPS) is located on the northwestern tip of Tasmania (figure 3.1, 40° 41' 00" S, 144° 41' 22" E), on top of a 94 m cliff looking out over the Southern Ocean. The site has been running continuously since 1978 and is funded and managed by the Australian Bureau of Meteorology, with the scientific programme jointly supervised by the Australian Nuclear Science and Technology Organisation (ANSTO), the Commonwealth Science and Industrial Research Organisation (CSIRO) and the University of Wollongong.

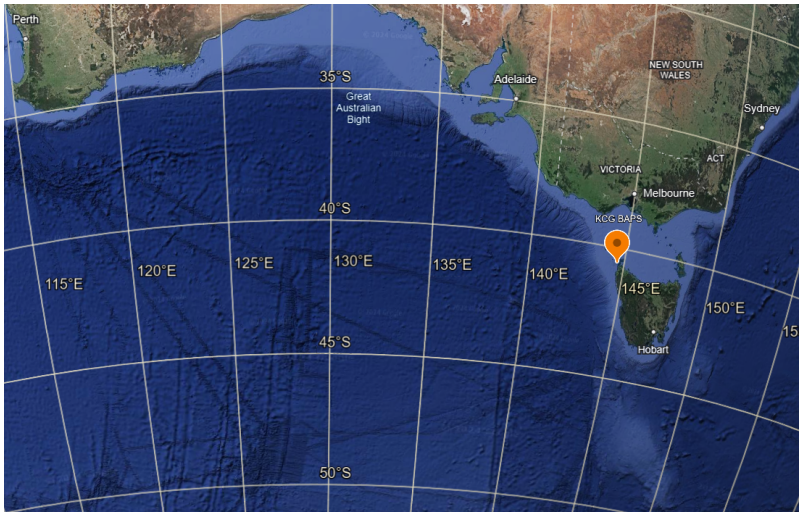

Figure 3.1: Map of the south of Australia, Tasmania and the Southern Ocean, with the location of the KCG BAPS in the north-west of Tasmania indicated by the orange marker.

The site measures both the clean, background air from the Southern Ocean (baseline) and polluted air masses (non-baseline) that have travelled to the site from the Australian mainland or over Tasmania. Periods when baseline air is being sampled are identified primarily using Radon-222 measurements taken at the site (described in detail in Williams *et al.* [83]). Radon, a noble gas that is relatively insoluble in water, is emitted from land $\sim$ 100 times more rapidly than it is emitted from water and has a half-life of 3.8 days, making it a good indicator of how recently air masses have been in contact with land and therefore exposed to land-based pollution [84]. A detailed overview of baseline filtering at KCG BAPS can be found in Molloy and Galbally [85], but, in short, data collected

when radon was $\leq$ 100 mBq m^{-3} is considered baseline. In 2022, baseline air identified using radon measurements was sampled 33% of the time.

3.2.2 CVAO and KCG BAPS NO_x instrument comparison

NO_x measurements at both the CVAO and at the KCG BAPS have been conducted using an AQD chemiluminescence instrument for over 15 years. Section 2.2 describes the NO_x AQD instrument used at CVAO, as well as the calibration and zeroing procedures. Full details of the measurement of NO_x at KCG BAPS can be found in the technical manual written by Dr Ian Galbally [82]. Rather than give a full description of the instrumental set-up at KCG BAPS, this section will highlight the key differences in how the NO_x measurements are carried out at the two sites, summarised in table 3.1.

Table 3.1: Key instrumental set-up differences between the NO_x AQD instrument used at the CVAO and at the KCG BAPS.

Difference	CVAO	KCG BAPS
NO_x converters	BLC (385 nm) and custom-built diodes (395 nm)	BLC (385 nm)
NO_x inlet box position	Inside the lab	At the inlet (figure 3.2)
Humidity correction	Nafion to dry ambient air	Humidifier to humidify zero air
Calibration frequency	Every 61 hours	Daily
Zero air measurement	30 minutes	1 hour
Measurement cycle	5 minutes	20 minutes

Set-up differences

The two main set-up differences between the sites are how differences in humidity between the ambient and zero air are minimised and the placement of the inlet box. At the the KCG BAPS, a humidifier is used to humidify the zero air rather than using a Nafion to dry the ambient air (as is done at the CVAO, described in section 2.2.3), and the inlet box is placed right at the inlet, as shown in figure 3.2. Placing the inlet box at the inlet means that the NO_2 converter (only one is used at KCG BAPS, a BLC) is at the inlet and that both calibrations and zero air measurements occur at the inlet, with NO calibration gas and zero air being

Figure 3.2: The NO_x inlet (highlighted in orange) on the side of the 10 m tower and the NO_x inlet box (highlighted in red) on the roof of the KCG BAPS.

pumped up to the inlet, where they are sampled and then pumped back down into the main lab, where the ozoniser and the detector are. The NO_x inlet box at the CVAO has also, in the past, been placed at the inlet, at the top of the 7.5 m tower, however a large amount of interferences were seen due to the BLC overheating in the sun, outside of the temperature controlled lab.

Operational differences

The differences in how the instrument operate are due to differences in the measurement cycle and in the frequency and length of calibrations and zero air measurements. The measurement cycle at the CVAO is 5 minutes long and is made up of 1 minute of pre-reactor zero, 2 minutes of NO, 1 minute of NO_x with the BLC and 1 minute of NO_x with the diodes (figure 3.3). At KCG BAPS, measurement cycles are 20 minutes long and are made up of 4 minutes of pre-reactor zero, 4 minutes of NO, 4 minutes of NO_x, 4 minutes of NO and lastly 4 minutes of pre-reactor zero with the BLC turned on (figure 3.3).

Calibrations at the CVAO take place every 61 hours (section 2.2.4), whereas calibrations at KCG BAPS are carried out daily and are made up of six cycles (three NO sensitivity cycles and three NO_x conversion efficiency cycles), an extra NO sensitivity cycle compared to CVAO calibrations. The zero air measurements at the KCG BAPS are an hour long and are carried out both before and after the calibration, as opposed to being 30 minutes long and taking place only after the

Figure 3.3: An hour of raw ambient NO_x measurements from CVAO and KCG BAPS taken between midday and 13:00 (UTC at CVAO, UTC+10 at KCG BAPS) on 1st January 2022, with the different types of measurements during the measurement cycles highlighted.

calibration, as occurs at the CVAO.

3.3 CVAO and KCG processing comparison

The processing code used to analyse NO_x data from CVAO is described in detail in section 2.3, the code used for KCG BAPS data is described briefly in section 3.3.1. The comparison between these two processing codes was performed by using both these codes to analyse raw NO_x data from KCG BAPS from 2022. The CVAO processing code had to be slightly modified in order to be used for the NO_x data from KCG BAPS due to differences in the way the two AQD NO_x analysers are operated (described in 3.2.2). The aim of this section is to note the differences between the two processing codes and assess whether data processed by the two codes are comparable.

3.3.1 KCG processing code overview

As NO_x at KCG BAPS is measured using an AQD NO_x analyser, the raw data files contain the same information as those at CVAO (raw counts, instrumental parameters and valve settings). The first step in the data processing is a pre-processing step carried out in Python, the subsequent steps are carried out in R. The pre-processing step in Python is used to create a monthly data file and to check that there are no gaps in the data. The monthly data files are then read into R, where data are removed based both on manually inputted periods when there were instrumental issues or work being carried out at the site, as well as

removing data automatically based on whether instrument parameters fall within acceptable ranges, shown in table 3.2.

Table 3.2: Instrumental parameters used to assess the KCG BAPS NO_x AQD's operational state and the range of acceptable values.

Instrumental parameter	Acceptable range
Raw counts	100 to 100,000 cps
PMT high voltage	1610 to 1650 V
O_2 flow	90 to 95 mL min^{-1}
Reaction chamber pressure	4 to 7.5 Torr
Inlet sample flow	1000 to 1050 mL min^{-1}
PMT temperature	-40 to -20 °C

The daily calibrations are then processed in order to calculate the sensitivity (in ppt cps^{-1} rather than in cps ppt^{-1}, as is done at CVAO) and the conversion efficiency (CE). The hourly mixing ratios for NO and NO_2 are then calculated using the sensitivity and CE, and finally the ozone and offset corrections are applied. As will be fully discussed in section 3.4, the method for determining measurement offsets at the KCG BAPS has not yet been finalised due problems with the zero air (ZA) measurements and difficulties in identifying a period when values can be assumed to be zero. Therefore, the methods used for offset and ozone corrections have been excluded from the comparison of the two processing codes in this analysis.

3.3.2 Data processing step 1: reading in raw data files and calculating initial statistics

As described in sections 2.2.3 and 3.2.2, both sites use a modified AQD NO_x instrument, leading to similar raw data files, with some differences in the variable names. The variable names that are used to determine what state the instrument is measuring in (zero, NO, NO_x ambient, calibration or zero air) are called key columns and the names used for these key columns at both sites, as well as a description of what they indicate, are shown in table 3.3 below.

The CVAO NO_x ambient measurement cycle (5 minutes) is shown in table 3.4. All key columns referring to calibrations and zero air measurements are off during ambient measurements. The delay column refers to the amount of time that is dropped when switching to a new measurement mode.

Table 3.3: Key column names in both codes, as well as a description of what these key columns indicate. For all key columns, 1 means that the variable is on, 0 means that it is off.

KCG	CV (raw data)	CV (processing code)	Description
Inlet_BLC	NO2_converter	NO2_converter	BLC converter
zero_valve_1	zero_valve_1	NOx_zero_k	Pre-reactor zero
Inlet_NOx	NOx_cal	NOx_cal_k	Calibration
NO_valve	NO_valve	calMFC_k	NO cal gas flowing
NOx_cal	Titration_lamp	GPTLamp_k	Gas phase titration
Inlet_ZA	zero_air_valve	NOx_za_k	Zero air
N/A	diodes	NO2_converter_diode	Diode converter

The KGC NO_x ambient measurement cycle (20 minutes) is shown in table 3.7. The KCG BAPS processing code uses an 18 second transition delay when any key variable changes. All key columns relating to calibration and zero air measurements are off during ambient measurements.

The key difference in the cycles is the presence of an extra NO and pre-reactor zero measurement within the KCG BAPS measurement cycle. The final pre-reactor zero (measured with the NO_2 converter on) is not used in the processing code. The second NO measurement is used in the processing code.

At the CVAO calibrations are preformed every 61 hours (for a full description of the calibration cycle at CVAO, see section 2.2.4). The calibrations are made up of five cycles, two NO_x CE calibration cycles (titrated - t), followed by three NO

Table 3.4: Summary of the 5-minute measurement cycle at the CVAO and how the different measurement modes are identified in the processing code based on the values in the key columns.

Time (s)	Delay (s)	Species	NOx_zero_k	NO2_converter	NO2_converter_diode
0-60	10	Zero	On	Off	Off
60-180	10	NO	Off	Off	Off
180-240	30	BLC NO_x	Off	On	Off
240-300	30	Diode NO_x	Off	Off	On

Table 3.5: Calibration variables and their associated key columns used in the CVAO processing code.

Species	Column name	NO2_converter	NOx_zero_k	NO2_converter_diode	NOx_cal_k	calMFC_k	GPTLamp_k
Calibration zero	Cal_zero	Off	On	Off	On	On	/
Untitrated NO	NO_u	Off	Off	Off	On	On	Off
Titrated NO	NO_t	Off	Off	Off	On	On	On
Untitrated NO_2 (BLC)	NO2_u	On	Off	Off	On	On	Off
Titrated NO_2 (BLC)	NO2_t	On	Off	Off	On	On	On
Untitrated NO_2 (Diodes)	NO2_u_diode	Off	Off	On	On	On	Off
Titrated NO_2 (Diodes)	NO2_t_diode	Off	Off	On	On	On	On

Table 3.6: Calibration variables and their associated key columns used in the KCG BAPS processing code.

Species	Column name	Inlet_BLC	Zero_valve_1	Inlet_NOx	NO_valve	NOx_cal
Calibration zero (untitrated)	ZerocalNO	Off	On	On	On	Off
Calibration zero (titrated)	zeroNOcalNOtitrNOx	Off	On	On	On	On
Unitrated NO	NOcalNO	Off	Off	On	On	Off
Titrated NO	NOcalNOtitrNOx	Off	Off	On	On	On
Untitrated NO_2	NOxcalNO	On	Off	On	On	Off
Titrated NO_2	NOxcalNOtitrNOx	On	Off	On	On	On

Table 3.7: Summary of the 20-minute measurement cycle at the KCG BAPS and how the different measurement modes are identified in the processing code based on the values in the key columns.

Time (s)	Species	Inlet_BLC	zero_valve_1
0-240	Zero	Off	On
240-480	NO	Off	Off
480-720	NO_x	On	Off
720-960	NO	Off	Off
960-1200	Zero	On	On

sensitivity cycles (untitrated - u). Table 3.5 shows how the different measurement types are identified in the CVAO processing code for calibrations (zero air is always off during calibrations).

At KCG BAPS calibrations occur daily and are made up of six cycles (section 3.2.2), three NO sensitivity cycles (untitrated, calNO) followed by three NO_2 conversion efficiency cycles (titrated, calNOtitrNOx). Table 3.6 shows how the KCG BAPS calibration variables are defined.

Once all the measurement modes have been defined using the key columns, initial statistics are calculated. The CVAO code calculates the average pre-reactor zero, NO and NO_x counts for each measurement cycles, whereas the KCG BAPS code calculates the median zero, NO and NO_x counts over an hour, without calculating median values for the individual cycles within the hour. The CVAO data are also hourly averaged, but this is done after the 5-minute averaged NO and NO_2 mixing ratios have been calculated.

For calibration calculations, the initial averaging is done differently compared to ambient data. The CVAO code only uses the last untitrated (sensitivity) and the last titrated (CE) cycles to find the mean of the calibration species (defined in table 3.5). The KCG BAPS code uses all the calibration cycles to find the calibration species defined in table 3.6, and calculates the median rather than the mean of the species.

3.3.3 Data processing step 2: calibration and mixing ratio calculations

Both processing codes calculate the CE and sensitivity once the initial statistics have been calculated. Both the sensitivity and the CE are calculated slightly differently at the two sites, and the differences are due to the air sampled at

the site. As described in section 2.2.1, at the CVAO air reaching the site is almost always clean, marine air, whereas at the KCG BAPS (described in section 3.2.1) baseline conditions occur only $\sim 30\%$ of the time. When calculating the sensitivity at the CVAO, the increase in counts due to the addition of NO cal gas is calculated by subtracting the NO counts from the cycle before the cal (equation 2.2), since the ambient NO mixing ratios are low and fairly constant. At the KCG BAPS, this is not the case therefore the sensitivity is calculated by using the pre-reactor zero measured during the sensitivity calibration as a way to determine the increase in counts due to the addition of NO cal gas, as shown in equation 3.1. The sensitivity at KCG BAPS is calculated in ppt cps^{-1}, rather than in cps ppt^{-1} as is done at CVAO and for the purposes of this comparison, sensitivity calculated using the CVAO code was also calculated in ppt cps^{-1}.

$$\text{Sensitivity} = \frac{\text{NO mixing ratio during cal}}{\text{NO counts during cal} - \text{Pre-reactor zero counts during cal}} \tag{3.1}$$

The CE at the KCG BAPS is calculated using zero corrected NO values, as shown in equation 3.2, again to account for the fact that the background NO_x values are often not baseline levels.

$$\text{CE} = \frac{(NO_{xt} - NO_t) - (NO_{xu} - NO_u)}{(NO_u - zero_u) - (NO_t - zero_t)} \tag{3.2}$$

Once the sensitivity and CE have been calculated, the mixing ratios for NO and NO_2 can be calculated. First, the signal due to NO and the signal due to NO_2 are calculated by subtracting the pre-reactor zero from NO and the NO counts from NO_2, then the mixing ratios are calculated using the equations 3.3 and 3.4 (multiplying by the sensitivity rather than dividing by the sensitivity due to the fact that the sensitivity at KCG BAPS is calculated is ppt cps^{-1}).

$$\text{NO mixing ratio (ppt)} = \text{NO}_{\text{signal}} \times \text{Sensitivity}_{\text{ppt cps}^{-1}} \tag{3.3}$$

$$\text{NO}_2 \text{ mixing ratio (ppt)} = \text{NO}_{2\,\text{signal}} \times \text{Sensitivity}_{\text{ppt cps}^{-1}} \times \text{CE} \tag{3.4}$$

3.3.4 Comparison outcome

The key differences in the processing codes used at the two sites are summarised in table 3.8. The CVAO processing code was modified to accommodate these differences, to verify whether, once the known differences between the two processing codes are accounted for, the output when both codes are processing the same data are very similar.

Table 3.8: A summary of the differences between the NO_x processing codes used at the CVAO and at the KCG BAPS.

Difference	CVAO code	KCG BAPS code
Initial statistics	Average over each cycle	Median over an hour of measurements
Transition times	Delays in table 3.4	Delays in table 3.7
Calibration data selection	Last calibration cycle	All calibration cycles
Sensitivity calculation	Previous NO cycle used (eq. 2.2)	Pre-reactor zero during cal used (eq. 3.1)
CE calculation	No zero correction (eq. 2.1)	Zero correction (eq. 3.2)

A paired t-test was performed for the four different outputs (Sensitivity, CE, NO mixing ratios and NO_2 mixing ratios), and indicated that the differences between the NO and NO_2 mixing ratios determined with the two different codes were not statistically significant (p = 0.06 and p = 0.6, respectively). The differences between sensitivity and CE instead were statistically significant (p = 0.03 and p = $9.7 \times 10^{-}5$, respectively), however the small mean difference between the two datasets (0.00014 for the sensitivity and 0.0008 for the CE), despite being statistically significant, is likely not practically meaningful given the scale of the data (mean sensitivity ~ 0.82, mean CE ~ 0.95). This may indicate a minor but consistent bias between the two processing codes, rather than a substantive difference in output.

The plots in figure 3.4 show the output of the CVAO and KCG BAPS codes plotted against each other for NO sensitivity, NO_2 CE, ambient NO and NO_2. Periods where there were instrumental issues or disruptive activity at the KCG BAPS have been removed. As the sensitivity and the CE are used to calculate NO and NO_2 mixing ratios, differences in sensitivity and CE are propagated into differences in the mixing ratios.

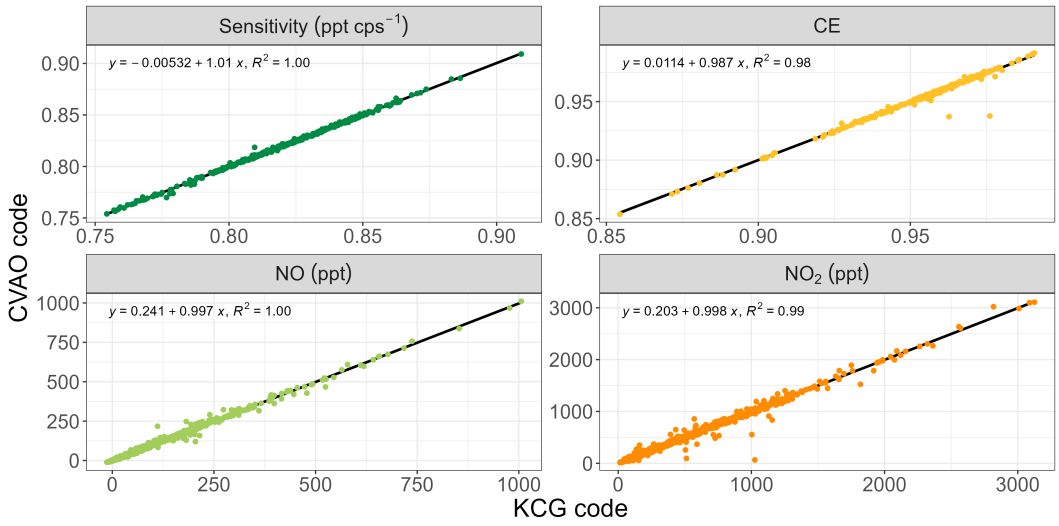

Figure 3.4: Plots of sensitivity, CE, NO and NO_2 mixing ratios for KCG BAPS NO_x data from 2022, calculated using the CVAO code and the KCG BAPS code. Equations and R^2 values are displayed in each panel.

The last steps in processing the raw NO_x data are applying the offset and ozone corrections, however a method for NO_x offset determination at the KCG BAPS has not yet been finalised. The following section describes potential ways of calculating the offsets at the KCG BAPS and the issues surrounding them.

3.4 KCG NO_x offset determination

An in-depth discussion of the causes of offsets and how they are determined can be found in section 2.2.5. In summary, offsets can be determined either by using the pre-reactor zero (O_3 surface reactions and O_3 reactions with alkenes at different rates to O_3 + NO) or by using NO_x-free air (O_3 reactions with alkenes at the same rate as O_3 + NO, NO_2 surface reactions and NO_z thermal and photolytic interferences). NO_x-free air can either be ambient air that has been scrubbed of NO_x using a pure air generator (a PAG 003, Eco Physics AG is used at both the CVAO and the KCG BAPS) or ambient air that is measured in periods when the mixing ratio of NO or NO_2 is likely to be close to 0 ppt. The following sections describe different methods for determining offsets by using NO_x-free air and any associated issues.

3.4.1 Zero air measurements

At both sites, ZA measurements are carried out after a calibration (every 61 hours at the CVAO and daily at the KCG BAPS, see section 3.2.2), however these values cannot provide an accurate measurement offset for NO or NO_2 in baseline conditions. When the pure air generator (PAG) scrubs NO_x from the ambient air, it also removes NO_y compounds and volatile organic compounds (VOCs), which can be sources of interference in NO_x measurements, therefore ZA from the PAG is not able to quantify all possible measurement offsets. ZA is also dried and a difference in humidity between ZA and ambient air could lead to offsets being overestimated or underestimated. At the CVAO, ambient air is dried with a Nafion (section 2.2.3) and at the KCG BAPS ZA is humidified (section 3.2.2) to attempt to keep the humidity of ZA and sampled ambient air the same, however problems with these methods have been encountered at both sites, potentially leading to spurious ZA signals.

When measuring tens and hundreds of ppts of NO_x, these inaccuracies in the determination of offsets only have a small effect on the final mixing ratios, however in baseline conditions, when mixing ratios are a few ppts, well quantified and understood measurement offsets are necessary to report the measured mixing ratios with confidence and carry out further analysis with the data.

3.4.2 Offset determination using ambient values

NO_2 monthly minima offsets

NO_2 offsets at both sites can be calculated from the NO_2 monthly minima, as this is considered representative of the NO_2 offset, based on the assumption that within a month, NO_2 mixing ratios at the site will be 0 ppt at some point, therefore the lowest monthly value is caused by the NO_2 offset (see section 2.2.5).

Nighttime NO offsets

In clean, unpolluted environments, nighttime values of NO tend to 0 ppt, as at night NO and O_3 react (R 2.1) but NO is not regenerated by NO_2 photolysis (R 2.4), leading to virtually all the NO being converted into NO_2 and its mixing ratio tending to 0 ppt. The use of nighttime (between 21:00 and 04:00 UTC, LT -1) measurements to offset-correct NO works well at the CVAO, since clean baseline air is sampled $\sim 95\%$ of the time, meaning that almost every nighttime

NO measurement can be used, leading to daily NO_x-free measurements carried out in ambient air.

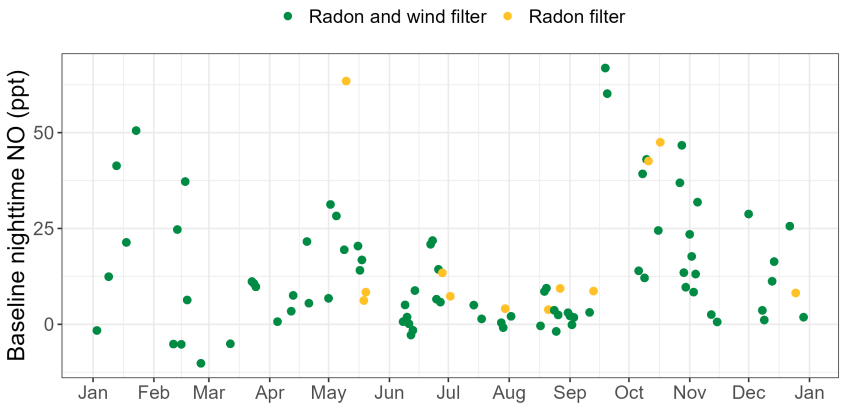

Figure 3.5: Baseline nighttime NO (between 22:00 and 04:00 LT, UTC + 10) measured in 2022, coloured by whether the radon filter (radon $\leq$ 100 mBq m^{-3}) is used alone (in yellow) or with the wind filters (WS $\geq$ 20 km h^{-1} and 190° $\geq$ WD $\leq$ 280°, in green).

At the KCG BAPS, only $\sim$ 30% measurements are made under baseline conditions (radon $\leq$ 100 mBq m^{-3}), therefore most nights NO would not be expected to tend to 0 ppt, leading to significant gaps between baseline nighttime NO measurements. Furthermore, figure 3.5 shows that in 2022 even on nights (between 22:00 and 04:00 LT, UTC + 10) when sampling baseline air, NO mixing ratios range from -10 to 66 ppt, showing a large amount of variability, which could be due to NO_x emissions from the soil surrounding the KCG BAPS [82]. As the CVAO is surrounded by volcanic rock, NO_x soil emissions are not a concern at this site. Wind speed ($\geq$ 20 km h^{-1}) and wind direction (between 190° and 280°) can also be used to filter data for baseline conditions, however even with this extra layer of filtering applied (data in green in figure 3.5), the nighttime NO values are still high and variable.

3.5 Summary and future plans

The processing comparison between the CVAO and the KCG BAPS has shown that the methods used to treat the data at both sites yield very similar results, once operational and set-up differences have been accounted for. This comparison again highlights the difficulties measuring NO_x at such low mixing ratios, with further challenges at the KCG BAPS due to the large range of mixing ratios that are routinely measured at the site, with air masses from the clean baseline sector

and from the polluted Australian mainland being sampled. As a result of these challenges, problems with measurement offsets still remain in the KCG BAPS NO data, with more work needed to verify whether a suitable measurement offset can be determined for historic baseline NO measurements. At the time of writing, ongoing work is being carried out to update the NO_x KCG BAPS processing script and to quantify NO_x soil emissions measured at the KCG BAPS.

Plans are in place for the collaboration between the University of York and CSIRO to continue, with future aims of submitting KCG BAPS NO_x data to the World Data Centre for Reactive Gases (WDCRG) and comparing NO_x mixing ratios from the remote marine boundary layer (MBL) in the Northern and Southern hemispheres.

Chapter 4

Changes in NO_x at the CVAO between 2012 and 2024: effects of changing air masses and implications on atmospheric oxidation processes

4.1 Introduction

As discussed in chapter 1, over the oceans the hydroxyl radical, OH, oxidises pollutants and greenhouse gases (GHGs), in what is referred to as the atmosphere's self-cleaning cycle. In the marine boundary layer (MBL), the photolysis of ozone, O_3, is the main source of OH and its mixing ratios are controlled by the amount of nitrogen oxides (NO and NO_2, referred to as NO_x) and volatile organic compounds (VOCs) present. Lee *et al.* found that at the Cabo Verde Atmospheric Observatory (CVAO) the O_3 compensation point (at which there is a switch from an O_3 destroying to an O_3 producing regime) was between 17 and 34 ppt of NO, therefore currently a net destruction of O_3 occurs [18]. Even small changes in the compositions of air masses that reach the site, due to changing meteorology or air quality, could have a profound impact on the chemistry that occurs over the oceans. It is therefore important to understand the processes that take place in this environment, to better predict what effect these changes will have on the atmosphere's self-cleaning cycle.

In order to test our understanding of the chemistry occurring over the oceans, a photostationary state (PSS) analysis can be performed. Under PSS conditions, NO and NO_2 are in equilibrium (R 4.1-R 4.3) and if O_3 were the only species converting NO into NO_2, the Leighton relationship $\varphi = \frac{j_{NO_2}[NO_2]}{k_{O_3}[O_3][NO]}$ would be 1 [86].

$$NO + O_3 \longrightarrow NO_2 + O_2 \quad \text{(R 4.1)}$$

$$NO_2 + h\nu \xrightarrow{j_{NO_2}} NO + O(^3P) \quad \text{(R 4.2)}$$

$$O(^3P) + O_2 + M \longrightarrow O_3 + M \quad \text{(R 4.3)}$$

Deviations from 1 indicate that other oxidants are present and convert NO to NO_2, specifically hydroxy and peroxy radicals (HO_2 and RO_2) and halogen oxides (IO and BrO) are known to oxidise NO into NO_2, shown in R 4.4-R 4.7.

$$NO + RO_2 \longrightarrow NO_2 + RO \quad \text{(R 4.4)}$$

$$NO + HO_2 \longrightarrow NO_2 + OH \quad \text{(R 4.5)}$$

$$NO + IO \longrightarrow NO_2 + I \quad \text{(R 4.6)}$$

$$NO + BrO \longrightarrow NO_2 + Br \quad \text{(R 4.7)}$$

Adding these reactions and rearranging the Leighton relationship gives the equation to calculate PSS NO_2 (eq. 4.1), which can then be compared to measured values of NO_2 to test our understanding of the NO_x cycling in the troposphere.

$$NO_{2\ PSS} = \frac{(k_{O_3}[O_3] + k_{RO_2}[RO_2] + k_{HO_2}[HO_2] + k_{IO}[IO] + k_{BrO}[BrO])[NO]}{j_{NO_2}} \quad (4.1)$$

Under low-NO_x conditions previous studies have found that the PSS analysis underestimates the amount of NO_2 measured [19, 68, 87–89]. The underestimation of PSS NO_2 compared to measured values could be due to errors in the measured values, specifically measurement offsets in NO_2 mixing ratios or large uncertainties in measurements of RO_2 [73], or to a missing oxidant, which is able to convert NO to NO_2 and has not been accounted for.

Studies performed under low-NO_x conditions have also revealed discrepancies

between measured and modelled OH, HO_2 and RO_2 [27, 90–94]. These discrepancies point to the fact that the current understanding of atmospheric radical chemistry is incomplete. In environments where NO_x mixing ratios are low and VOCs mixing ratios are high, particularly in forested regions, RO_2 isomerisation has been proposed as an unclassical method leading to the regeneration of OH, specifically through the autoxidation of RO_2 [95]. The reactive aldehyde mechanism (RAM) describes the series of H-shifts that occur in a RO_2 radical leading to the formation of a hydroperoxyl-carbonyl (HPC, or a similar species depending on the substituents present on RO_2), which photolyses to produce OH [96]. In Beijing, Whalley *et al.* hypothesised that model underprediction of measured RO_2 could be due to the preferential isomerisation of the alkoxy radical RO, formed following R 4.4 (particularly when RO_2 is derived from monoterpenes or long-chain alkanes), leading to the regeneration of a peroxy radical rather than the formation of a hydroxy radical and a carbonyl [90]. As a result, RO_2 could undergo multiple reactions with NO, oxidising it into NO_2, prior to being converted into HO_2.

The role of Cl atoms in reacting with VOCs to produce RO_2 has also been noted. In a coastal urban site in southeastern China, Chen *et al.* measured large mixing ratios of HOCl (mean midday peak of 181 ppt) and found that OH and Cl radicals formed by HOCl photolysis reacted with VOCs leading to an increased production of HO_2 and RO_2 [97]. Lawler *et al.* reported HOCl mixing ratios between <5 and 173 ppt and Cl_2 mixing ratios between <1 and 35 ppt at the CVAO, noting that the mixing ratios in both species were notably higher in air containing aged pollution compared to clean North Atlantic air, but could not fully explain the measured values [98]. The mineral dust-sea spray aerosol (MDSA) mechanism described by van Herpen *et al.* proposes that Cl is produced through the catalytic photoreaction of Fe(III) chlorides formed in sea salt and Saharan dust aerosols [99]. This mechanism could therefore provide a pathway for the production of Cl over the North Atlantic, which could oxidise VOCs and produce more HO_2 and RO_2.

NO_2 PSS analysis carried out by Andersen *et al.* using NO_x data from the CVAO revealed that NO_2 was underpredicted by the box model, most notably in air masses with aged pollution, indicating that a missing oxidant able to convert NO into NO_2 may be present in these more polluted air masses [68]. In African air masses affected by Saharan dust, the MDSA mechanism could be producing more Cl leading to increased production of HO_2 and RO_2. Whalley *et al.* found

good agreement between measured and box modelled daytime OH and HO_2 at the CVAO, highlighting the importance of including halogen chemistry in the model to improve HO_2 predictions, but noted that the impact of IO and BrO on NO_x mixing ratios had not been considered [27].

This chapter examines the NO_x timeseries from the CVAO (2012 to 2024 for NO, 2017 to 2024 for NO_2), focusing on trends in NO_x and how these change with different air masses in sections 4.3.1 and 4.3.2. In section 4.3.4 a PSS analysis is carried out on this timeseries and the possible causes for an increase in discrepancy between the measured and PSS NO_2 values as the years progress are discussed.

4.2 Experimental

4.2.1 Measurements at the CVAO

The NO_x instrument used at the CVAO is described in chapter 2, which also gives a full description of the CVAO (see section 2.2.1). As summarised in table 2.1, O_3, CO, CO_2, CH_4, VOCs and met data (RH, air temperature, pressure, wind speed and direction) are also measured at the site. More in-depth descriptions of measurement of photolysis rates and of halogen oxides made at the CVAO are given below, as these have not yet been described in this thesis.

Photolysis rates

At the CVAO a spectral radiometer, consisting of a 2-pi sr quartz diffuser coupled to an Ocean Optics spectrometer via a 10 m fibre optic cable, is used to measure solar UV flux. It operates between 200 and 1000 nm, calibrated between 250-750 nm at 1 nm resolution, with an integration time of 1 minute. It utilises a Hamamatsu back-thinned FFT-CCD detector with >90% quantum efficiency at 700 nm. From the spec rad measurements, 47 photolysis rates are calculated using Python code developed by Dr Lisa Whalley at the University of Leeds, based on accurate absorption cross sections and quantum yields from the literature [100].

The spec rad was calibrated in 2016, 2019 and 2025 against a 1000 W (FEL) quartz-halogen tungsten coil filament lamp (Gooch and Housego, NIST traceable FEL 1000-W lamp standard of spectral irradiance, OL FEL-A, bearing the designation F-1128) at the University of Leeds. Providing the fibre optic cable

isn't changed, the calibration is relatively constant over a number of years [101]. The calibration uncertainty is $\sim 5-6\%$ at 300 nm and 4% at 650 nm. This uncertainty is mainly due to the certified accuracy of the irradiance standard.

For periods when the spec rad wasn't measuring, the monthly correlations of photolysis rates with solar radiation for each hour between 09:00 and 17:00 are used to calculate the photolysis rates. The error associated with the calculated photolysis rates is considered to be the slope of this correlation. Further details can be found in appendix A.

Halogen oxides

Halogen oxide radicals, BrO and IO, were measured at the CVAO between November 2006 and June 2007 using differential optical absorption spectroscopy (DOAS) [25, 102]. Yearly midday means of IO (1.4 ± 0.8 ppt, 1σ) and BrO (2.5 ± 1.1 ppt, 1σ) are used in this analysis. Although Mahajan *et al.* reported only limited seasonal variability between November 2006 and June 2007, the use of a constant value for IO and BrO is not able to capture any changes these species may undergo with changing air masses or changing atmospheric processes [102]. All the calculations that these values are used in are looking at daytime (between 11:00 and 15:00 UTC) chemical processes, therefore considering the diurnal variation in IO and BrO is not necessary for this study.

4.2.2 Hydroxy and peroxy radicals

Measured (February 2023)

Measurements of RO_2, HO_2, OH and OH reactivity were made at the CVAO during the PEROXY campaign in February 2023. These measurements were made using the University of Leeds's fluorescence assay by gas expansion (FAGE) laser-induced fluorescence (LIF) instrument, operated by Dr Lisa Whalley, Dr Graham Bousted, Dr Sam Seldon and Dr Rachel Lade. The instrument set-up, calibrations and offset determinations are described fully in Dr Sam Seldon's thesis [103].

Briefly, HO_2 and RO_2 are converted into OH, which is then detected using laser induced fluorescence at 308 nm [104]. In order to convert HO_2 and RO_2 into OH, firstly RO_2 is converted into HO_2 through reaction with NO, after which CO is then added to convert any OH back into HO_2 (figure 4.1). In

the FAGE cell, all the HO_2 (from RO_2 conversion and from OH conversion) is then reacted with NO to convert it to OH, which is then detected through laser induced fluorescence [105]. As measurements of OH, HOx (OH and HO_2) and ROx (OH, HO_2 and RO_2) can be made depending on whether NO and CO are added, these species can be subtracted from each other to determine values of OH, HO_2 and RO_2.

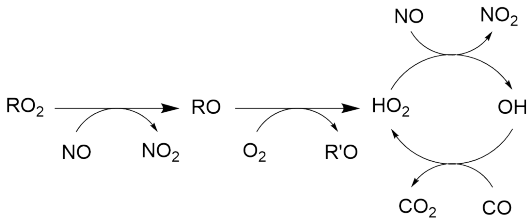

Figure 4.1: Reactions that take place within the FAGE LIF instrument to convert HO_2 and RO_2 into OH. Adapted from Fuchs *et al.* [105].

During the PEROXY campaign, calibrations were performed weekly using a portable flow tube which converts humidified air into OH and HO_2. Calibrations taken earlier in the campaign were excluded due to instrumental issues. The data were corrected for O_3 interference (on average this interference was 5.9×10^5 molecules cm^{-3}) and for water vapour effect. Nighttime values were used to zero both HO_2 and RO_2, due to an unknown artefact potentially in the NO cylinder or in tubing from this cylinder to the instrument. Applying nighttime zeroes corrects the effects of this artefact and brings nighttime values down to around 0. During this campaign, measurement uncertainties for OH, HO_2 and RO_2 were found to be $\sim 21\%$.

Box modelled

Monthly diurnal mixing ratios of HO_2 and RO_2 were determined between July 2017 and June 2020 using a zero-dimensional chemical box model [106], which incorporated a subset of the Master Chemical Mechanism (MCM v3.31) into the AtChem2 modelling toolkit [107], fully described in Andersen *et al.* [67]. A list of reactions added to the MCM can be found in appendix B. For months when box modelled HO_2 and RO_2 mixing ratios were not available (August 2020 to December 2024), an average mixing ratio for that month was used instead.

4.2.3 Air mass backtrajectories

Air mass composition at the CVAO is determined by running 10 day backtrajectories using FLEXPART (version 10.4) in backwards mode, driven by pressure data from the Global Forecast System (GFS) reanalyses at $0.5° \times 0.5°$ resolution. Backtrajectories are run every 6 hours and the amount of time (in %) spent over each region (North Atlantic, South Atlantic, North America, South America, Europe, Sahara, Sahel, West Africa, Central Africa and Upwelling, defined in figure 2.3) at an altitude below 1000 m is calculated.

4.3 Results

4.3.1 NO_x mixing ratios at the CVAO

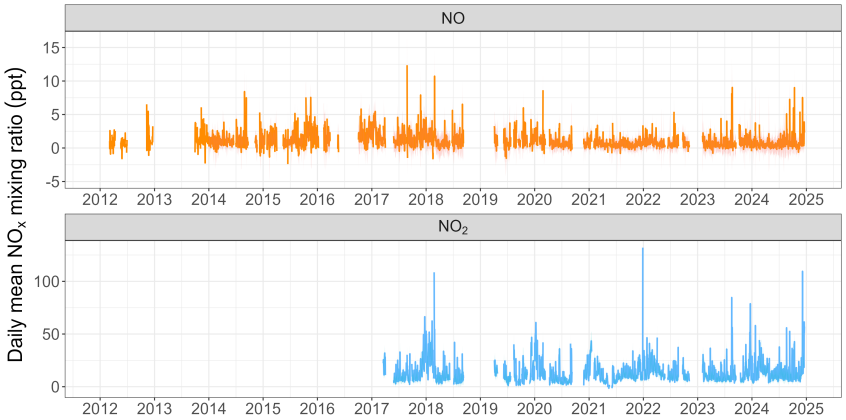

Figure 4.2: Daily averaged NO_x timeseries measured at the CVAO under baseline conditions. Shading represents measurement uncertainties (calculated as described in section 2.3.6.

The daily-averaged NO (2012 to 2024) and NO_2 (2017 to 2024) timeseries from the CVAO are shown in figure 4.2. The measurement offsets associated with NO_2 data measured before 2017 (when the diodes were installed) cannot be properly quantified, therefore these data are not considered reliable. The data in figure 4.2 have been processed as described in section 2.3, and filtered to remove extreme values (as described in section 2.3.4) or measurements collected when sampling air that has passed over the island (wind speed < 2 m s^{-1} or wind direction between 100° and 340°) to ensure that only NO_x mixing ratios from the clean MBL are shown. Data measured below the instrument's limit of detection

(LOD) are considered valid therefore are included in figure 4.2 and have been used in this analysis. Hourly timeseries of NO_x data from the CVAO are available on EBAS and have been quality controlled by ACTRIS. NO_x data from 2024 have been submitted to ACTRIS, however have not yet gone through QA/QC at the time of writing, so may be subject to changes.

NO_x diurnal cycles

Clean background (as defined above) NO and NO_2 diurnal cycles between 2017 and 2024 are shown in figure 4.3, coloured by season. The NO diurnal peaks around midday, with mixing ratios returning to zero overnight. Over the oceans, without any fresh emissions, the key source of NO is the photolysis of NO_2, therefore the highest NO mixing ratios are seen when the photolysis rates are largest, at noon. At night NO continues to react with O_3, however NO_2 no longer photolyses to yield NO, therefore in the absence of emissions NO mixing ratios return to zero. The effect of these reactions can also be seen in the NO_2 diurnal cycle, which shows growing NO_2 mixing ratios overnight, with a peak just before dawn. NO_2 mixing ratios then decrease during the day, with measurements made in autumn and winter showing a bump in the afternoon (potential due to production of NO_2 from pNO_3^- photolysis producing more NO_2 than is being photolysed to NO, discussed in chapter 5). For both species, mixing ratios are by far highest in the winter. NO mixing ratios are lowest in the spring, whereas NO_2 mixing ratios are lowest in the summer. This difference between NO and NO_2 could be due to the higher photolysis rates in the summer,

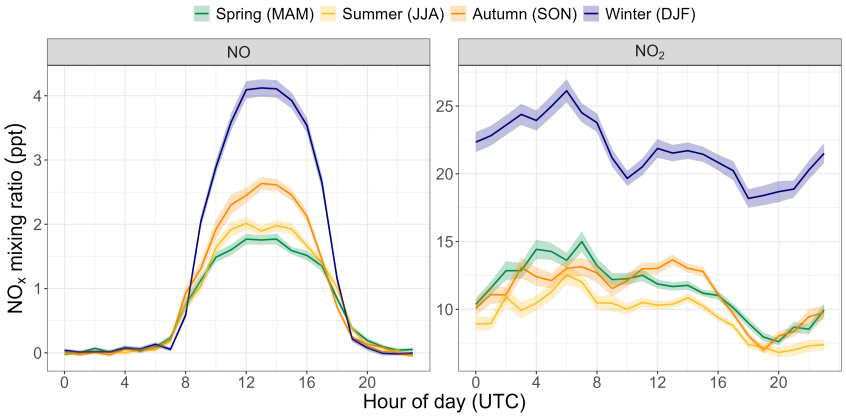

Figure 4.3: NO and NO_2 diurnals (in UTC, LT-1) coloured by season, between 2017 and 2024. Shaded areas represent the standard error.

which leads to slightly more NO and slightly less NO_2.

NO_x mixing ratios in different air masses

As well as being driven by the changes in photolysis rates throughout the year, the seasonality of NO_x mixing ratios at the CVAO is also due to the seasonality of the air masses reaching the CVAO, described in section 2.2.1. Seasonal changes in the Azores anticyclone, located north of Cabo Verde, result in changes to the air masses reaching the site with more African and European air in the autumn/winter and more North Atlantic air in the summer. As described in section 4.2.3, 10 day back-trajectories are run every 6 hours and the percent of time each back-trajectory spent over each region (defined in figure 2.3) is calculated. In order to determine changes in NO_x mixing ratios in different air masses, the percentages calculated from back-trajectories have been used to define five different air mass categories, using the daily average air mass composition at the CVAO:

- **African (Afr):** days when the air reaching the site spent at least 1% of time over Africa (Sahara, Sahel, West and Central Africa), and more than half the polluted air (African, European or North American air) was African.
- **European/North Atlantic (Eu/NAt):** days when the air reaching the site spent at least 1% of time over Europe, and more than half the polluted air (African, European or North American air) was European.
- **North America/Atlantic (Am/NAt):** days when the air reaching the site spent at least 1% of time over North America, and more than half the polluted air (African, European or North American air) was North American.
- **North Atlantic (NAt):** days when the air reaching the site spent at least 98% of time over the ocean (Upwelling, North or South Atlantic), with less than 1% of the oceanic air coming from the Southern hemisphere.
- **Southern Hemisphere (SH):** days when the contribution from the Southern Hemisphere was over 1% (with more time spent over the Southern Hemisphere than over polluted Northern Hemisphere regions).

This classification focuses on identifying the days in which the air reaching the site has been clearly influenced by one particular region. For this reason, days

during which multiple air masses are present in high amounts have been excluded from further analysis. In particular, in order for any day to be classified as African, European/North Atlantic or North American/Atlantic (the three "polluted" air masses), the air reaching the site needs to have spent more than 50% of the total time spent over the "polluted regions" over one of these three regions.

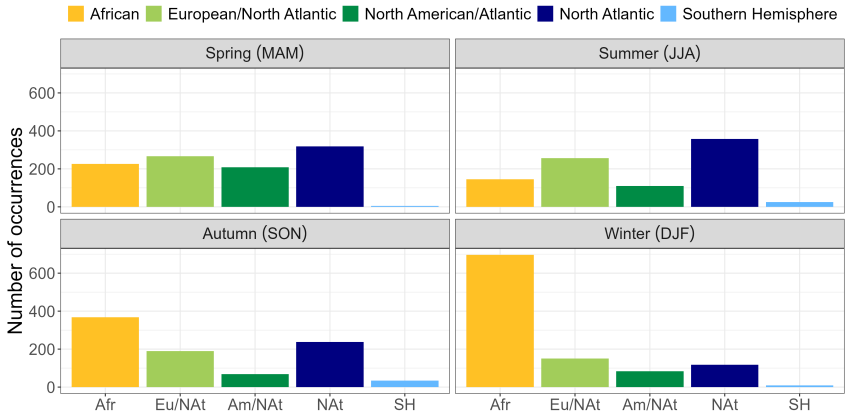

Figure 4.4: Number of occurrences of each air mass (between 2012 and 2024) in the different seasons at the CVAO.

Figure 4.4 shows how the air masses at the CVAO change over the seasons, as well as how prevalent each air mass type is at the site. Between 2012 and 2024, the predominant air mass at the CVAO was African for 30% of the days, North Atlantic 22% of the days, European 18% of the days, North American 10% of the days and from the Southern Hemisphere 2% of days. As the Southern Hemisphere air mass is only sampled on 2% of days it is not included in further analysis. The remaining 18% of days were not classified, either because they were affected by local pollution (defined as periods with wind speed below 2 m s^{-1} or wind direction between 100° and 340°) or because they did not clearly fit into the five categories described above (air masses that had similar amounts of influence from more than one region).

As shown in table 4.1, the highest mixing ratios for NO and NO_2 are measured in the African air mass, followed by air masses with European influence and air masses with North American influence. The lowest mixing ratios are seen in the North Atlantic air mass. The difference between all air masses apart from the North Atlantic and North Atlantic/American air mass are statistically significant (calculated using ANOVA (analysis of variance) and Turkey's range test). The lifetime of NO_x over the oceans ranges from a few hours to a few days and depends on the abundance of OH and therefore on photochemical activity. Aged

Table 4.1: Mean ($\pm 2\sigma$) daytime (11:00–15:00 UTC) NO and NO_2 mixing ratios between 2017 and 2024 in the four different air masses at the CVAO, as described above.

Air mass	Daytime NO (mean $\pm 2\sigma$)	Daytime NO_2 (mean $\pm 2\sigma$)
African	3.0 ± 6.4 ppt	16.3 ± 28.1 ppt
European/North Atlantic	2.5 ± 5.6 ppt	13.4 ± 22.8 ppt
North American/Atlantic	1.9 ± 5.1 ppt	11.8 ± 16.9 ppt
North Atlantic	1.7 ± 4.4 ppt	10.8 ± 14.2 ppt

pollution from North America generally takes longer to reach Cabo Verde than aged pollution from Europe or Africa and therefore NO_x mixing ratios in these air masses are likely lower due to reactions with OH that remove NO_x from the atmosphere. Photochemical activity is also lower in winter months, which are when the majority of African air masses reach the site (figure 4.4), therefore NO_x lifetimes are likely slightly longer and result in more NO_x pollution reaching the site in the season when the most African air is being sampled.

4.3.2 Trends in NO_x at the CVAO

Mixing ratios over the oceans are low, on the order of a few ppt for NO and tens of ppt for NO_2, but it is possible to see fluctuations in the amount of NO_x measured at the CVAO over the years. As shown in figure 4.3, NO_x mixing ratios are higher in the winter, therefore the data were deseasonalised using seasonal and trend decomposition using Loess (STL) before plotting the monthly means. The STL method does not work if there is any missing data, so a Kalman filter was used to fill missing data before they were deseasonalised.

The deseasonalised monthly averaged NO mixing ratios (shown in figure 4.5, filtered as described in section 4.3.1 to only include measurements of the clean MBL) increase fairly steadily between 2012 and 2017, followed by a decrease between 2017 and 2021. Between 2021 and 2024, NO monthly averaged mixing ratios remained fairly stable, with a gradual increase. As mentioned above, NO_2 mixing ratios are not available prior to 2017, but between 2017 and 2024 NO_2 monthly mean mixing ratios follow a similar, though less dramatic, trend as NO. NO_2 mixing ratios decrease between 2017 and 2019, are stable between 2019 and 2022, and show a gradual increase in 2023 and 2024, but don't show a bump between 2019 and 2020 which is seen in NO.

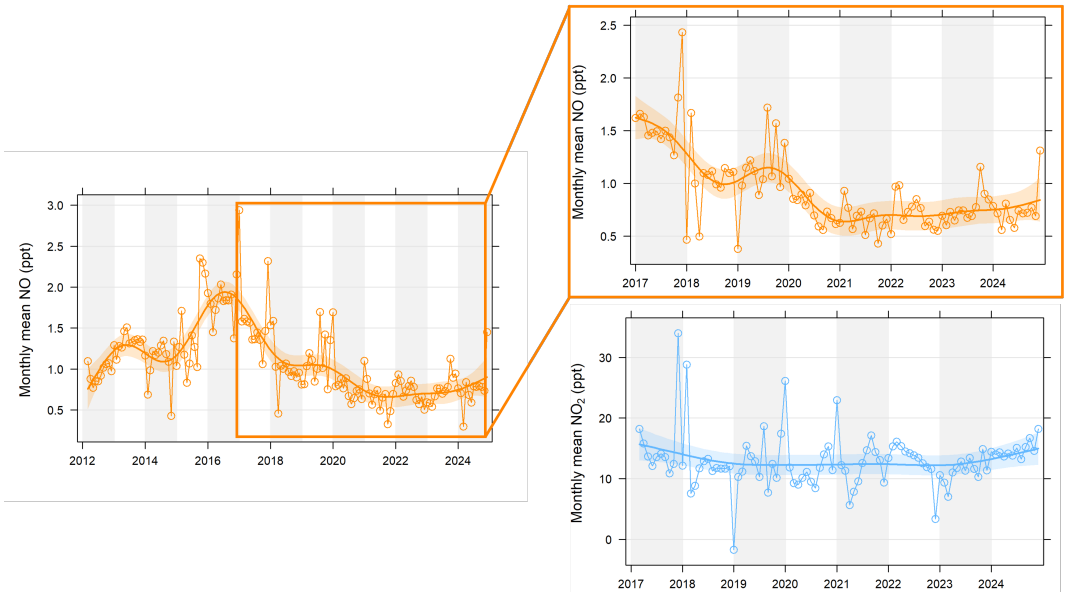

Figure 4.5: Deseasonalised monthly mean NO_x mixing ratios from the CVAO. Months with less than 30% data coverage are excluded from analysis. Data are deseasonalised using STL. The shaded areas represent the 95% confidence intervals of the smooth line fit.

Air mass trends at the CVAO

The trends seen in NO_x mixing ratios at the CVAO could be in part explained by changes in the air masses reaching the site. The different air masses reaching the site are calculated as described in section 4.2.3. Figure 4.6 shows the monthly mean North Atlantic, African (Sahara, Sahel, Western and Central Africa) and European air mass contributions at the CVAO between 2012 and 2024. As described in section 2.2.1, the air masses exhibit seasonality, therefore these data have also been deseasonalised using STL and as backtrajectories are run every 6 hours a Kalman filter was also used here to fill missing data.

Figure 4.6 shows that there have been changes to the air mass composition at the CVAO, most notably a peak in North Atlantic air (and a dip in African and European air) in 2013, followed by a dip in North Atlantic air (and a peak in African and European air) in 2015/2016. From this dip in 2016, the North Atlantic contribution has been steadily increasing, matched by a steady decrease in European air. African air has remained fairly stable between 2018 and 2024, with two local maxima, in 2019/2020 and in 2023, and dips in 2018, 2021 and 2024. These small fluctuations are the counterpart to similar fluctuations seen in North Atlantic air, which is generally increasing in this period, but has local

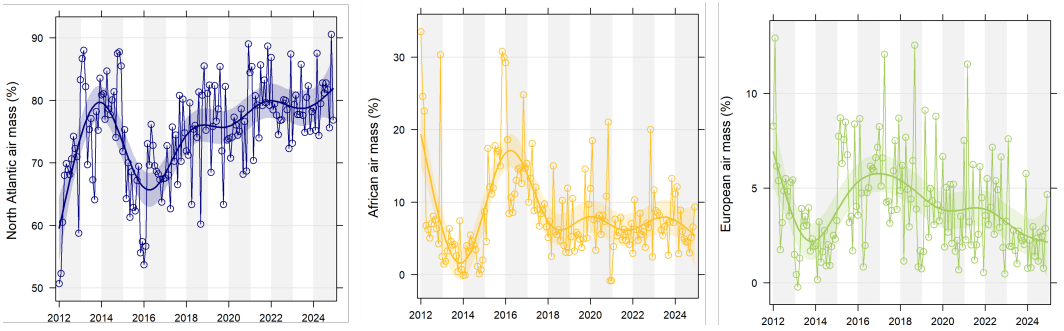

Figure 4.6: Deseasonalised monthly mean North Atlantic (left, in blue), African (centre, in yellow, includes Saharan, Sahelian, western and central African air masses) and European (right, in green) air mass contributions to the CVAO. A map of air mass regions can be found in figure 2.3.

peaks in 2018, 2021 and 2024.

The changes in air mass composition at the CVAO broadly line up with the trends in NO shown in figure 4.5. NO mixing ratios increase between 2012 and 2016, with a dip in 2014 which corresponds to a dip in African and European air masses and a peak in clean North Atlantic air masses. The highest NO monthly mixing ratios are seen in 2016, which corresponds to the largest contributions of African and European air at the CVAO. From 2017 to 2024, both African and European air has been decreasing at the site and North Atlantic air has been increasing, which is reflected by a decrease in NO_2 between 2017 and 2019 and in NO between 2017 and 2021, interrupted by a slight increase in 2019/2020 in NO, when there is an increase in African air. NO_2 and NO have remained fairly stable from 2019 onwards and from 2021 onwards, respectively, with both showing a slight increase in mixing ratios in 2023 and 2024. This increase is not reflected in the air mass behaviour, as the amount of North Atlantic air at the station has continued to increase and African and European air has decreased.

NO_x mixing ratios in different air masses over the years

Whilst the trends in air masses generally help explain the trends seen in NO and NO_2 at the CVAO, they don't show how NO_x is changing within a specific air mass over the years. Figure 4.7 shows how the NO and NO_2 mixing ratios changed between 2012 (2017 for NO_2) and 2024 in African, European/North Atlantic and North Atlantic air, with the air masses classified as described in section 4.2.1 above.

It is worth noting that the air mass categories described in section 4.2.1 are very

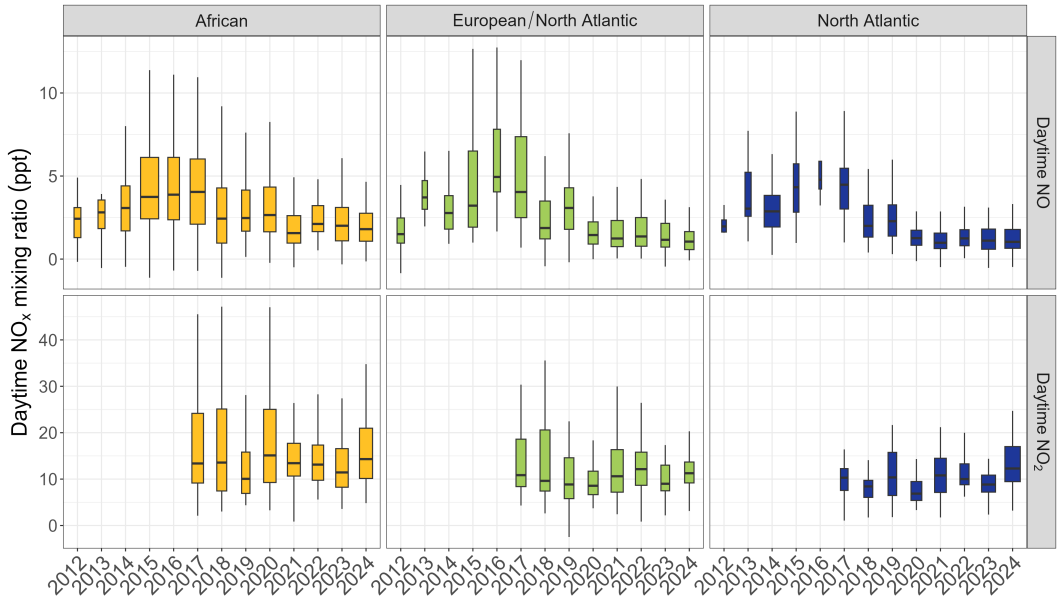

Figure 4.7: A box plot (with outliers removed) of daily averaged daytime (11:00–15:00 UTC) NO and NO_2 mixing ratios in African, European and North Atlantic air masses measured at the CVAO between 2012 and 2024 (NO_2 data only available from 2017). The width of each box represents the number of data points available for that year, species and air mass.

broad and air reaching the site from Africa and Europe always has contributions from the North Atlantic. Air masses classified as African will be predominantly influenced by African air, but could also have a significant European contribution, and vice versa. The number of data points available each year for each species and air mass could also lead to the data being skewed. NO mixing ratios are highest in all three air masses between 2015 and 2017, however the number of data points available, especially in the European and North Atlantic air masses are low compared to previous years. In 2016 in particular data were only available in autumn/winter months (as can be seen in the timeseries in figure 4.2), which is when NO_x is generally highest and most measurements are made in African air (see figure 4.4), leading to a spread of data that is not representative of the whole year. In 2017, when the NO_2 diodes were installed at the CVAO, the Nafion dryer was also added to the system to dry the ambient air, which reduced quenching and thus improved the instrument sensitivity. From 2018 onwards the spread of NO data decreases likely thanks to this change. Data availability in both species from 2017 is also better compared to that between 2012 and 2017, leading to a more reliable and representative set of measurements. The causes and effects of the higher data spread seen between 2015 and 2017 are discussed

further in section 4.3.4.

The changes in NO and NO_2 mixing ratios within the different air masses could be caused by changes in emissions and meteorology over the oceans, over Africa and over Europe. Both NO and NO_2 mixing ratios show a decrease between 2019 and 2020 in European and North Atlantic air masses, which is not seen in the African air mass, potentially indicating that COVID-19 lockdowns had less of an effect on NO_2 emissions in Africa. Whilst there is a large amount of literature on the decrease of many pollutants in Europe, including NO_2, as a result of the COVID-19 pandemic [108–111], the impact on emissions in Africa has not been researched as extensively. Fawole *et al.* show that there is a decrease in NO_2 mixing ratios in Western Africa, however Doumbia *et al.* show that the decreases in NO_2 in Africa are smaller compared to those seen in other regions, including Europe [112, 113]. Han *et al.* used chemical reanalysis to determine quarterly dual anomalies and quarterly anomalies for spring (MAM) and summer (JJA) 2020, seeing a reduction in NO_2 in Western, Central, Southern and Eastern Africa, but an increase in Northern Africa when using the quarterly anomalies method and hypothesised that this was due to NO_2 mixing ratios being higher than previous years in 2020, but with a smaller rate of increase compared to previous years [114]. Kganyago and Shikwambana report an increase of biomass burning emissions in Sub-Saharan Africa in 2020 compared to 2019, pointing to favourable meteorological and vegetation conditions in 2020 for fires, as well as the fact that due to lockdowns, less fire suppression activities were being carried out [115].

Following 2020, NO mixing ratios have remained fairly stable in all three air masses, whereas NO_2 mixing ratios have been quite variable. NO_2 trends reported by NASA show that between 2005 and 2021 there was an increase in NO_2 in most Western African cities for which data were available (15% increase in Nouakchott, Mauritania, 73% increase in Dakar, Senegal, 11% increase in Banjul, The Gambia, 29% increase in Bamako, Mali, 10% increase in Conakry, Guinea) with a decrease only seen in Bissau, Guinea Bissau, which is broadly seen in the NO_2 mixing ratios measured in African air at the CVAO [116]. Inter-annual variability in NO_2 in African air could be due to different meteorological conditions, with studies showing that NO_x emissions from wet soil in West Africa are enhanced compared to emissions from dry soils [117, 118], as well as differences in which regions specifically within the African continent are being sampled.

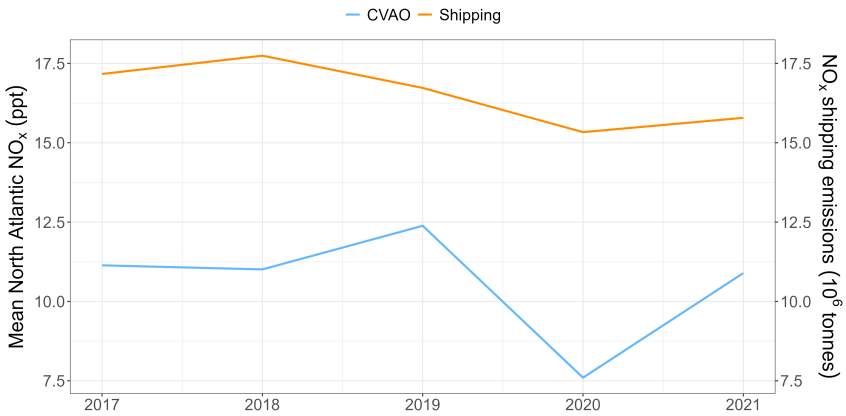

Figure 4.8: Mean yearly NO_x mixing ratios measured in the North Atlantic air mass at the CVAO between 2017 and 2021 (light blue, left axis) and annual NO_x shipping emissions (dark orange, right axis) [119].

Changes in NO_x mixing ratios in North Atlantic air masses are likely related to changes in shipping emissions, with a decrease in both NO and NO_2 in 2020. Yi *et al.* used the Shipping Emission Inventory Model (SEIMv2.2) to generate a ship emission inventory between 2016 and 2021, with the global NO_x data from this inventory compared to mean yearly NO_x mixing ratios measured in North Atlantic air at the CVAO between 2017 and 2021 in figure 4.8 [43, 119]. Broadly, global NO_x shipping emissions and NO_x measurements in the North Atlantic air mass at the CVAO follow similar trends in these years, with a dip in 2020 followed by an increase in 2021. Peak NO_x measurements at the CVAO were in 2019, despite global NO_x shipping emissions decreasing in 2019 from a peak in 2018. Lack of regional shipping emissions data for the North Atlantic makes it difficult to determine if the changes in NO_x in North Atlantic air are entirely due to shipping emissions, and no emissions data are available from 2021 to 2024, however the most recent Review of Maritime Transport, published by the UN trade and development (UNCTAD), reports that global maritime trade grew by 2.4% in 2023 and that between 2018 and 2023 port calls by container ships rose by 20% across Africa, indicating that there is an increase in shipping traffic both globally and regionally [120].

The photochemical production of NO in the ocean surface has not yet been tested in sea-water samples collected in the tropical North Atlantic Ocean, but has been reported by Tian *et al.* in artificial sea-water samples and in samples collected in the western tropical North Pacific Ocean and could therefore also represent a source of NO_x from the ocean at the CVAO [46].

4.3.3 Effects of NO_x on ΔO_3

As discussed in chapter 1, in the remote MBL O_3 depleting reactions dominate over O_3 producing processes. O_3 exhibits a strong seasonal cycle (figure 4.9, left) with the highest mixing ratios measured in the winter months and the lowest mixing ratios seen between July and October. In order not to be affected by this seasonality, changes in the amount of O_3 depletion are studied by looking at ΔO_3, the daily change in O_3 mixing ratios between the peak at 09:00 and the trough at 17:00 (figure 4.9, right).

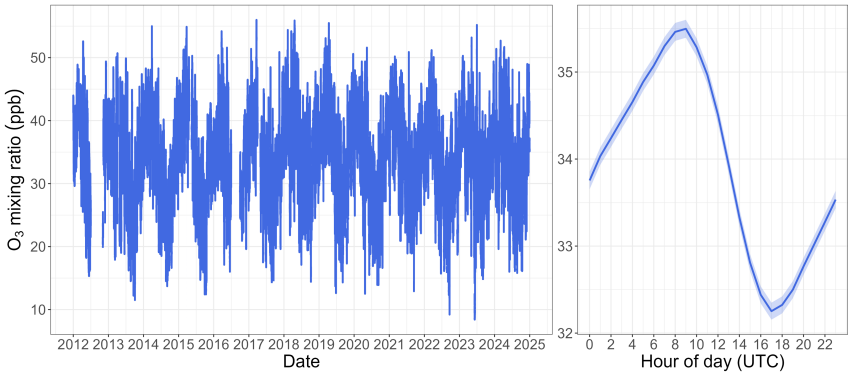

Figure 4.9: Hourly averaged O_3 timeseries (left) and diurnal cycle (right) from the CVAO between 2012 and 2024. The shaded area on the diurnal represents the standard error.

O_3 mixing ratios are affected both by chemical reactions and by physical processes, specifically entrainment from the free troposphere and dry deposition. Since all the chemical changes are photochemical, overnight changes in O_3 mixing ratios are due to entrainment and deposition. The boundary layer height changes throughout the day and is lower overnight, likely leading to less mixing, however over the oceans the diurnal change in boundary layer height is low. In this work, the entrainment and deposition are assumed to be constant throughout the day and can be calculated by taking the difference between O_3 mixing ratios at 22:00 and 03:00 (UTC, LT+1). This assumption may lead to an overestimation of daytime deposition, however because the boundary layer height is not expected to experience many changes over the oceans, this assumption is considered valid for this study. Between 2012 and 2024, the entrainment and deposition contribution to ΔO_3 ranged from a maximum of 0.54 ppb h^{-1} in April 2017 to a minimum of -0.38 ppb h^{-1} in August 2013, with the highest monthly average in May (0.32 ppb h^{-1}) and the lowest in September (0.11 ppb h^{-1}). These values are similar to

those reported by Read *et al.* (0.18–0.48 ppb h^{-1} between November 2006 and June 2007) and by Andersen *et al.* (0.18–0.35 ppb h^{-1} between July 2017 and June 2020) [25, 68].

ΔO_3 due solely to photochemical reactions ($\Delta O_{3\ chem}$) can be estimated by subtracting the entrainment and deposition term, calculated as the difference between O_3 mixing ratios at 03:00 and 22:00 (UTC, LT+1), from ΔO_3. Monthly values of $\Delta O_{3\ chem}$ are shown in figure 4.10 along with daytime NO mixing ratios. The main chemical pathways that lead to O_3 production involve the oxidation of NO by species other than O_3 (RO_2, HO_2, BrO and IO), leading to the formation of NO_2 which rapidly photolyses into NO and $O(^3P)$, with the latter reacting with O_2 to produce O_3. Changes in daytime NO mixing ratios and $\Delta O_{3\ chem}$ follow a similar monthly pattern, with the lowest NO mixing ratios and the largest amount of O_3 destruction occurring in May and the highest NO mixing ratios and smallest amount of O_3 destruction occurring in January.

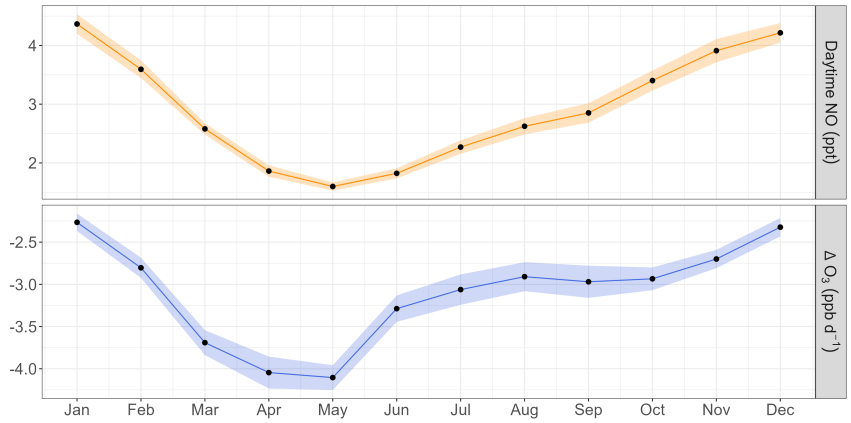

Figure 4.10: Monthly averaged daytime (11:00–15:00 UTC) NO mixing ratios and $\Delta O_{3\ chem}$ values measured at the CVAO between 2012 and 2024. Shading represents ± standard error.

The main loss pathway for O_3 in the remote MBL is its photolysis, followed by the reaction between water vapour and $O(^1D)$. Reactions between O_3 and OH, HO_2 and halogens (Br and I) are also loss mechanisms for O_3. The available O_3 production and loss terms are shown in figure 4.11. These terms were calculated using measured (NO, O_3, photolysis rates, met data) and box modelled (RO_2 and HO_2) values. OH, BrO and IO are assumed to be constant, with mixing ratios of 2×10^6 molecules cm^{-3}, 2.5 ppt and 1.4 ppt respectively, based on previous campaigns at the CVAO. The entrainment/deposition term was calculated as described above, from the difference between O_3 mixing ratios at 03:00 and 22:00

(UTC, LT-1). The O_3 loss due to reactions with halogens cannot be estimated for this period as a box model would be required to estimate this value, and this is outside the scope of this work. Although halogen reactions have been shown to represent a significant O_3 loss over the oceans, they are not expected to impact the seasonality of ΔO_3 as their concentrations are assumed to be constant at the CVAO [25].

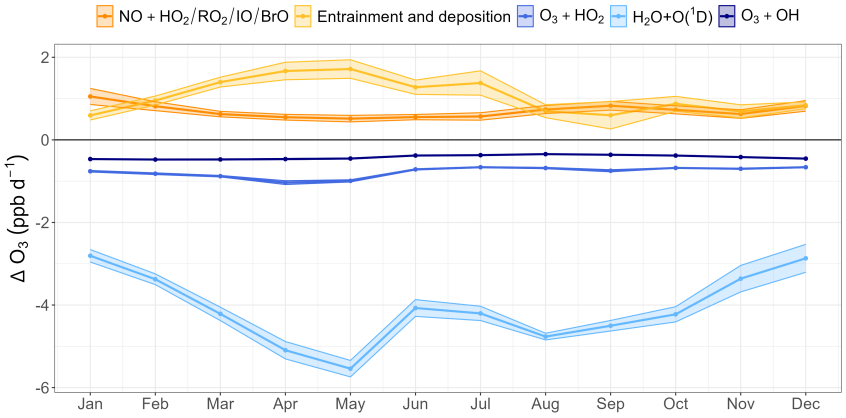

Figure 4.11: Monthly averaged O_3 production and loss rates between 2012 and 2024. The effects of halogens are assumed to be constant and are not included in this plot.

Higher values of the entrainment/deposition term are seen in the spring and summer months (March to July), with values for the rest of the year comparable to O_3 production from NO_x. The most O_3 production from this pathway is seen in January, which is also when O_3 destruction is at its lowest (figure 4.10), however reduced O_3 destruction from its photolysis followed by the reaction between $O(^1D)$ with water vapour is also seen in the winter months. O_3 loss from photolysis and O_3 production from NO follow a similar yearly pattern and as the term for photolysis loss is much larger than the term for NO_x production, this is the key driver for ΔO_3 over the oceans. Increases in NO_x will lead to more O_3 production, though the values currently seen at the site are well below the compensation point, where the regime switches to O_3 production. Continuing to carry out long-term measurements to understand how the atmospheric composition is changing over the oceans is however important, as a shift to an O_3 producing regime would have significant changes on the chemistry of the MBL.

4.3.4 NO_2 photostationary state

As well as allowing us to examine how NO_x mixing ratios are changing at the CVAO over the years and what factors are driving these changes, this long-term timeseries of NO_x measurements in the MBL provides a useful way of focusing on the gaps in our understanding of the atmospheric chemistry processes occurring in this environment, using photostationary state (PSS) analysis.

At the CVAO around midday (between 11:00 and 15:00 UTC, LT+1), NO_2 is under PSS as the average photochemical lifetime of NO_2 ($1/j_{NO_2}$, calculated between 2017 and 2024) was 2 minutes. Measurements collected when the NO_2 lifetime was over 10 minutes have been excluded from this analysis (0.1% data removed) as not being under PSS conditions. NO_2 mixing ratios can be calculated by balancing the NO_2 production from NO oxidation by O_3, RO_2, HO_2, BrO and IO (R 4.1, R 4.4–R 4.7) and NO_2 destruction through its photolysis (R 4.2), shown in equation 4.1.

$$NO_{2\ PSS} = \frac{(k_{O_3}[O_3] + k_{RO_2}[RO_2] + k_{HO_2}[HO_2] + k_{IO}[IO] + k_{BrO}[BrO])[NO]}{j_{NO_2}} \quad (4.1)$$

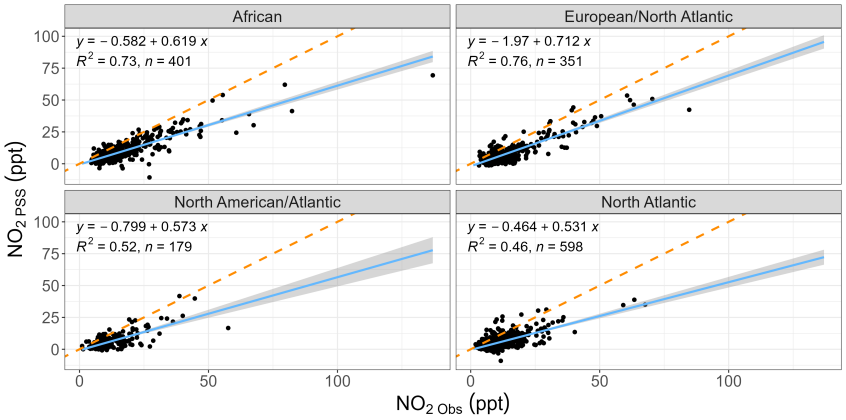

Figure 4.12: A plot of daily averaged midday (11:00–15:00 UTC) measured and PSS NO_2 mixing ratios from the CVAO between 2017 and 2024 in different air masses. The the 1:1 fit is the dashed orange line, the solid blue line is the line of best fit (equation, R^2 and number of available data points, n, displayed on each plot).

In eq. 4.1, j_{NO_2} is the photolysis rate of NO_2. The rate constants for R 4.1, R 4.4–R 4.7 are referred to as k_{O_3}, k_{RO_2}, k_{HO_2}, k_{IO} and k_{BrO}, respectively, with

the reaction rate for methyl peroxy (CH_3O_2) used for all RO_2 as modelling performed by Dr Lisa Whalley indicates that $\sim 90\%$ simple RO_2 at the CVAO is CH_3O_2 [103, 121]. NO, O_3 and j_{NO_2} are measured at the CVAO, as described in sections 2 and 4.2.1. RO_2 and HO_2 mixing ratios were determined using a zero-dimensional box model (section 4.2.2) between July 2017 and June 2020, with monthly diurnal averages calculated from July 2020 onwards. IO and BrO mixing ratios are estimated from measurements of these species taken at the CVAO between November 2006 and June 2007 (section 4.2.1).

The relationship between the measured and PSS NO_2 in different air masses at the CVAO is shown in figure 4.12. In all air masses, the PSS underestimates the measured NO_2 values, with better fits seen in the more polluted air masses (African and European), likely because in these air masses NO_x mixing ratios are higher resulting in a larger spread of data and less values close to the LOD. A Student's t-test was performed and confirmed that for all air masses, the difference between measured and PSS NO_2 was statistically significant.

PSS with measured HO_2 and RO_2 from February 2023

As discussed in section 4.1, the underestimation of measured NO_2 mixing ratio by PSS analysis has previously been attributed to a missing oxidant, which has been hypothesised to be RO_2 regenerated through unclassical isomerisation mechanisms. HO_2 and RO_2 were measured at the CVAO during the PEROXY campaign in February 2023 by the University of Leeds FAGE instrument (section 4.2.2, data available between 5th to 25th February 2023) and have been compared to the box modelled values for February 2018 and February 2020 in figure 4.13.

Both the box modelled years available (February 2018 and February 2020) overestimate measured HO_2 and RO_2 from February 2023. Modelled RO_2 in 2018 is likely lower than in 2020 because NO and NO_2 mixing ratios in 2018 are higher, leading an increase in conversion of RO_2 into HO_2 by NO (R 4.4). The box model used to generate HO_2 and RO_2 did not include terms for halogen chemistry or heterogenous losses to aerosols, likely resulting in the overestimation of measured values. Uncertainties still surround the value of the uptake coefficient γ_{HO_2} and the reaction rates and products between CH_3O_2 with halogen oxides (IO and BrO) [26, 122–124]. Running a more up to date box model which included halogen chemistry and a term for heterogenous losses would likely result in a more accurate estimate of HO_2 and RO_2 values at the CVAO, however

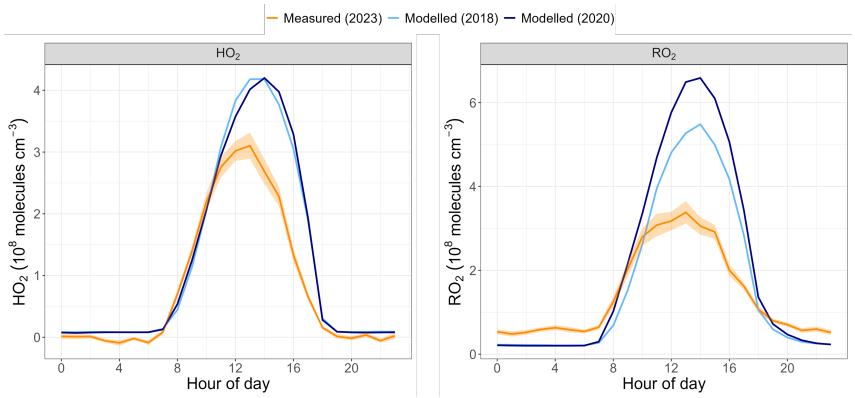

Figure 4.13: Measured (orange) and box modelled (blue) HO_2 (left panel) and RO_2 (right panel) diurnals. Measurements were collected during the PEROXY campaign (5th to 25th February 2023). Box modelled values are from February 2018 (light blue) and February 2020 (dark blue). Shaded area on the measured values represents ± SE.

the effect of halogen oxides on NO_x and O_3 would also need to be considered and as such was not within the scope of this thesis.

In order to carry out NO_2 PSS analysis, the average monthly diurnal HO_2 and RO_2 values were calculated for months when box modelled data weren't available (July 2020 onwards). Table 4.2 compares the measured values from February 2023 with the monthly averages from the box model that have been used to perform the PSS analysis. As seen in the diurnals in figure 4.13, both HO_2 and RO_2 are overestimated by the box model, with a normalised mean bias (NMB) for HO_2 of 37% and for RO_2 of 74%. In both cases, the modelled values fall outside the measurement uncertainty of 21% (1σ).

Table 4.2: Midday (between 11:00 and 15:00 UTC) mean measured and modelled HO_2 and RO_2 mixing ratios. Measured values collected during the PEROXY campaign in February 2023, box modelled values from an average of February 2018 and 2020 data. Uncertainties on measured HO_2 and RO_2 were estimated to be 21% (1σ).

Species	Measured midday mean	Modelled midday mean	NMB
HO_2	2.76×10^8 molecules cm^{-3}	3.78×10^8 molecules cm^{-3}	37%
RO_2	3.11×10^8 molecules cm^{-3}	5.41×10^8 molecules cm^{-3}	74%

The ratio between the measured and PSS NO_2 ($NO_{2\ Obs}/NO_{2\ PSS}$) can be used to visualise whether the PSS analysis is underestimating or overestimating measurements. A ratio of 1 indicates that the PSS is able to correctly reproduce measured NO_2 values, whereas deviations indicate that the PSS is overestimating (ratio < 1) or underestimating (ratio > 1) the measured values.

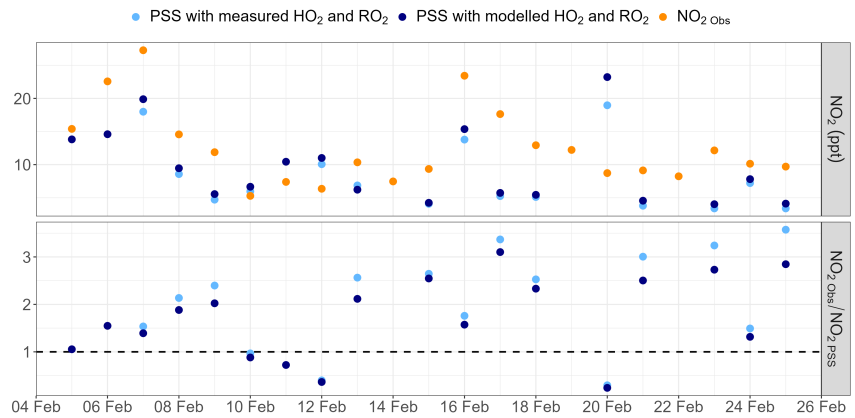

Figure 4.14: Daily averaged midday (11:00–15:00 UTC) measured (orange) and PSS NO_2 mixing ratios calculated using measured (light blue) and box modelled (dark blue) HO_2 and RO_2 values. The bottom panel shows the $NO_{2\ Obs}/NO_{2\ PSS}$ ratio when using measured (light blue) and box modelled (dark blue) HO_2 and RO_2 values. The dashed line indicates a 1:1 ratio.

As shown in figure 4.14 using the measured HO_2 and RO_2 values to calculate $NO_{2\ PSS}$ leads to a larger $NO_{2\ Obs}/NO_{2\ PSS}$ ratio than when using box modelled HO_2 and RO_2 values. This is simply because the box modelled values are larger than the measured values (table 4.2) and the PSS underestimates the observed NO_2 values. As discussed previously, this underestimation was thought to be missing RO_2, however the measurements from this campaign indicate that at the CVAO this is likely not the case, unless an unknown measurement offset has not been accounted for or the missing RO_2 is not measured by the FAGE. O_3 and water vapour corrections have been applied to the HO_2 and RO_2 measured values and nighttime values, which are known to be roughly 0, were used to correct for an unknown offset in the data, thought to be caused by an interferences in the NO cylinder (see section 4.2.2).

Factors affecting the $NO_{2\ Obs}/NO_{2\ PSS}$ ratio

Andersen *et al.* showed that at the CVAO between July 2017 and June 2020 a ratio of $\sim$ 1 was seen in air masses with low CO (< 80 ppb), ethane (< 0.75 ppb) and acetylene (< 50 ppt) mixing ratios, but deviations from 1 were seen with higher mixing ratios (CO > 100 ppb, ethane > 1.0 ppb, acetylene > 50 ppt), indicating that there could be a missing oxidant in more polluted air masses [68]. Expanding this analysis to include data from the CVAO from 2020 to 2024 (figure 4.15), however, shows that as the years progress, the deviations from 1 increased

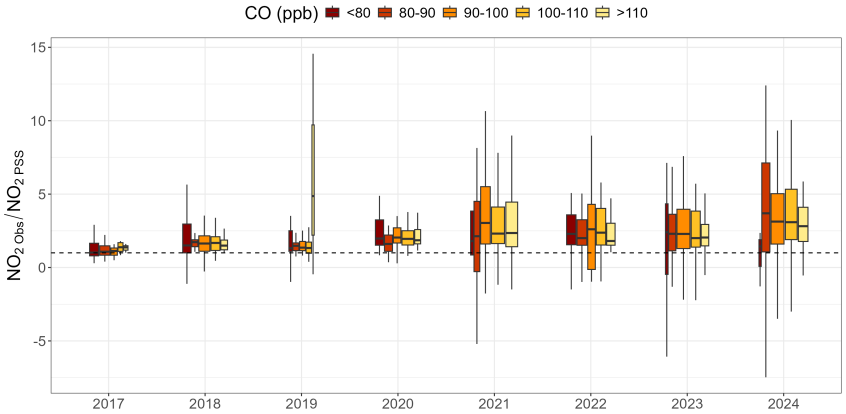

Figure 4.15: Box plot of the daily averaged $NO_{2\ Obs}/NO_{2\ PSS}$ ratio between 2017 and 2024, coloured by CO mixing ratios. The dashed line indicates a ratio of 1. The width of the boxes indicates the amount of data available.

regardless of the amount of aged pollution at the CVAO.

This yearly $NO_{2\ Obs}/NO_{2\ PSS}$ ratio increase, indicating an increase in PSS underestimation, could be due to changes in IO and BrO, which have not been measured at the site since 2007, with the average values from the 2006/2007 measurements used in this analysis. Differences between box modelled and measured HO_2 and RO_2 values could also lead to discrepancies between the measured and PSS NO_2, however comparison with the measured values from the PEROXY campaign indicates that it is likely that the box modelled values used are overestimating rather than underestimating actual values.

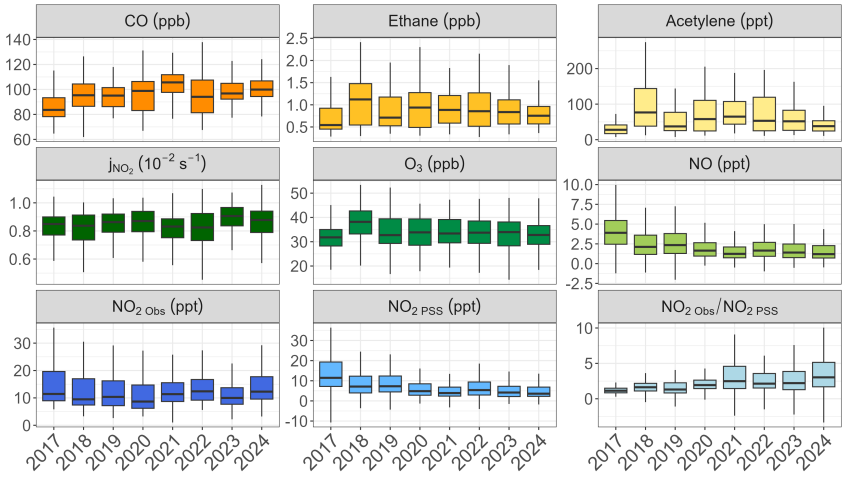

Figure 4.16: Daily averaged midday (11:00-15:00 UTC) values for measured CO, ethane, acetylene (RO_2 and HO_2 precursors), j_{NO_2}, O_3, NO and NO_2, along with the PSS NO_2 and the $NO_{2\ Obs}/NO_{2\ PSS}$ ratio between 2017 and 2024.

Measurement errors could also result in a discrepancy in the $NO_{2\ Obs}/NO_{2\ PSS}$ ratio, and this was investigated by looking at the species used to calculate $NO_{2\ PSS}$ (eq. 4.1). Figure 4.16 shows how species that affect NO_2 have changed between 2017 and 2024, including the measured terms of this eq. 4.1 (NO, O_3 and j_{NO_2}) and HO_2 and RO_2 precursors (CO, ethane and acetylene).

An increase in CO is also seen over this time period, which could have led to an increase in HO_2 mixing ratios, though without measurements it is impossible to say for certain. The key driver, however, does appear to be the decrease in NO between 2017 and 2024 which is not reflected in NO_2 mixing ratios. This results in $NO_{2\ PSS}$ mixing ratios decreasing and therefore increases the $NO_{2\ Obs}/NO_{2\ PSS}$ ratio, as the PSS underestimation of measured NO_2 increases.

NO_x instrumental changes

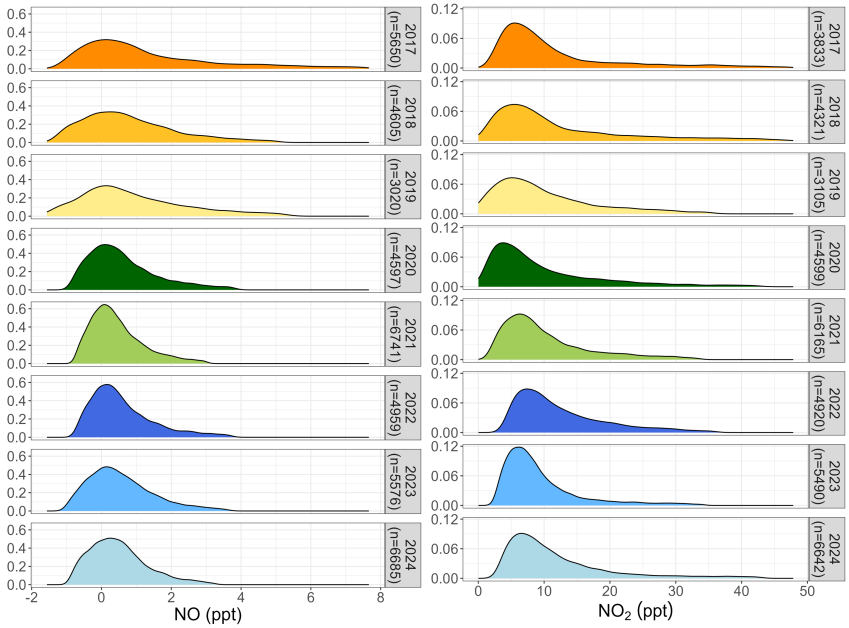

Figure 4.17: Yearly NO and NO_2 probability density functions with the upper and lower 5% of data removed. Amount of data available for each year is shown in the facet labels.

High NO mixing ratios between 2015 and 2017 were discussed in section 4.3.2, with figure 4.7 in particular showing that there is a wider range of values in these years. The probability density functions for NO and NO_2 (figure 4.17) show that between 2017 and 2019 the spread in both NO and NO_2 mixing ratios were broader and in general the same pattern is seen in both NO and NO_2,

however a much more distinct shift is visible in NO data distribution after 2020. Data availability could play a part in this, with low data coverage in 2019 in particular, however even when only looking at the later half of the year, when 2019 data coverage is good, the same probability density functions are seen.

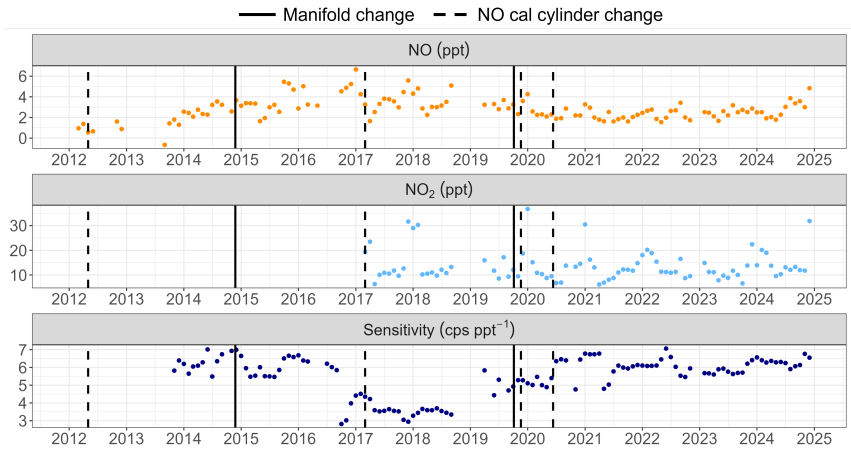

Figure 4.18: Monthly averaged NO and NO_2 mixing ratios and NO sensitivity. The solid lines indicate when the manifold was changed at the CVAO, the dashed lines indicate when the NO cal cylinder was replaced.

It is possible that instrumental or data processing changes could have affected the data, leading to artificially high or low values. Chapter 2 describes in detail the NO_x instrument and processing at the CVAO and highlights changes made to the processing code which were implemented from 2022 onwards, however when comparing data processed with both the old and the new version of the processing code minimal differences were noted (figure 2.17). In order to verify whether any instrumental changes at the CVAO could have affected the data, the monthly NO, NO_2 and NO sensitivity timeseries are shown alongside physical changes that have been made to the NO_x instrument at the CVAO in figure 4.18. The glass manifold used by all instruments at the CVAO is changed roughly every five years (solid black lines in figure 4.18) and following each change a comparison is performed to ensure that there hasn't been a step change in the mixing ratios for any of the sampled species. The two manifold changes that were performed between 2012 and 2024 do not appear to have affected the data. Changes in the NO calibration cylinder were also highlighted in figure 4.18 (dashed black lines) and are summarised in table 4.3.

The cylinder mixing ratio has always been around 5 ppm, which is then diluted to 40 ppb (discussed in section 2.2.4), and changes to the calibration

Table 4.3: A summary of NO calibration cylinder changes at the CVAO

Cylinder in use	Cylinder NO concentration
1st May 2012	5.05 ppm
1st March 2017	5.09 ppm
12th November 2019	5.17 ppm
19th November 2019	5.09 ppm
11th June 2020	5.17 ppm

cylinder concentration are accounted for in the data processing. While the difference between the calibration value and measurement values (tens of ppt) is large, it has not changed during the instrument's operation so is unlikely to have caused the increase in NO mixing ratios between 2015 and 2017. An increase in mixing ratios between 2012 and 2017 is seen, which then appears to decrease once the NO calibration cylinder is changed, however at this time other changes were also made to the NO_x instrument at the CVAO: the NO_2 diode converter was installed, allowing for reliable measurements of NO_2 to be collected, and the Nafion was installed, to dry ambient air. The drop in NO mixing ratios could therefore be in part attributed to a reduction in the effect of humidity on measurements. Figure 4.18 also shows the NO sensitivity (in cps ppt^{-1}) over the years, with a period of low sensitivity seen between the end of 2016 and 2019 which could also indicate that the instrument was not operating in its optimal conditions leading to more noisy data. From 2020 to 2024, the narrower spread of NO data, with values close to the LOD, appears therefore to be genuine, as the data processing was performed in the same way and there were no external changes to the instrument.

4.4 Conclusion

The NO timeseries collected at the CVAO between 2012 and 2024, and the NO_2 timeseries collected between 2017 and 2024 were presented. Both NO and NO_2 diurnal cycles show seasonality, with the highest values measured in winter when air masses reaching the site have higher African and European contributions and the lowest values measured in spring/summer when the air is predominantly clean North Atlantic.

Examining the trends in NO and NO_2 timeseries reveals a strong correlation between the mixing ratios seen and the amount of clean North Atlantic air,

African air and European air reaching the CVAO, with mixing ratios increasing over periods when the African and European air masses are more predominant and decreasing when the North Atlantic air mass is the predominant one. Changes in NO_x mixing ratios within the different air masses over the years broadly show that changes in emissions over these three different regions are reflected in the mixing ratios seen at the CVAO, though more work is required to understand how changes in meteorology and air composition in more polluted regions affect NO_x over the oceans.

NO_x was shown to be an important source of O_3 over the oceans, though the main factor affecting O_3 mixing ratios is its photolysis and reaction with water vapour. This loss mechanism dominates the O_3 production seen from NO_x and NO_x mixing ratios are still well below the O_3 compensation point, though it is important that long-term measurements and trend analyses are carried out in order to monitor changes in trace gas mixing ratios in the MBL.

NO_2 PSS analysis revealed that our current understanding of the photochemical processes involved in the cycling between NO and NO_2 in the marine MBL is incomplete. Using measured, rather than box modelled, values for HO_2 and RO_2 collected in February 2023 during the PEROXY campaign at the CVAO did not decrease the discrepancy between measured and PSS NO_2, implying that if any missing RO_2 is oxidising NO to NO_2, it currently cannot be detected by the FAGE. Decreasing NO mixing ratios between 2017 and 2024 lead to a decrease in $NO_{2\ PSS}$ mixing ratios over this time period that was not seen in measured NO_2 mixing ratios. The decrease in NO mixing ratios could in part be caused by instrumental changes, however more work is required to determine how large an effect these changes had on the measurement. Data from 2020 onwards are stable, however NO mixing ratios are very low, close to the instrument's LOD, making it difficult to perform a conclusive PSS analysis.

More measurements, especially of BrO, IO and HOCl, would help investigate the chemistry at play here, as halogens have been shown to be important to the chemical cycling over the oceans.

Chapter 5

HONO measurements from the CVAO: an investigation into factors affecting particulate nitrate photolysis

5.1 Introduction

The photolysis of nitrous acid, HONO (R 5.1), is an important source of the hydroxyl radical, OH, and nitrogen oxides (NO_x = NO + NO_2) in the clean, oceanic atmosphere, with the former being a key atmospheric oxidant and the latter being involved in the ozone cycle and the formation of secondary organic aerosols (discussed in detail in chapter 1).

$$\mathrm{HONO} + \mathrm{h}\nu \xrightarrow{j_{HONO}} \mathrm{NO} + \mathrm{OH} \qquad \text{(R 5.1)}$$

Understanding the production and loss pathways of HONO in the remote marine boundary layer (MBL) will therefore help improve our understanding of the atmosphere's oxidation capacity. The difficulties of measuring HONO in such a remote environment, where it is present at ppt levels, mean that there are substantial uncertainties surrounding the sources and sinks of HONO over the oceans.

In the remote MBL, the main loss pathway for HONO is photolysis (R 5.1), but it is also lost through dry deposition (R 5.2) and the reaction with OH (R 5.3). Studies have shown that the gas-phase reaction between NO and OH (R 5.4) is

only a small source of HONO in this environment and that the main source is instead photochemical [51, 66, 125–129].

$$\mathrm{HONO} \xrightarrow{k_{dep}} \tag{R 5.2}$$

$$\mathrm{HONO + OH \longrightarrow H_2O + NO_2} \tag{R 5.3}$$

$$\mathrm{NO + OH + M \longrightarrow HONO + M} \tag{R 5.4}$$

In more polluted regions, NO_2 uptake has been suggested as an important photochemical source [126, 130–132] and in rural and coastal environments soil emissions could explain missing HONO production [128, 133–135]. In the remote, clean, oceanic atmosphere, the key source of HONO is thought to be the photolysis of particulate nitrate, pNO_3^- [51, 66, 125, 129, 136–138]. Nitric acid, HNO_3, has long been considered a permanent sink for NO_x over the oceans, as its photolysis occurs on timescales that are too slow to be atmospherically relevant, however lab studies have shown that aqueous HNO_3, surface-adsorbed HNO_3 and pNO_3^- can undergo a much faster photolysis yielding HONO and NO_2 (R 5.5) [137, 139–144].

$$\mathrm{pNO_3^- + h\nu \xrightarrow{j_{pNO_3^-}} \mathit{x}\,HONO + \mathit{y}\,NO_2} \tag{R 5.5}$$

Uncertainty still surrounds the factors that result in the enhancement of pNO_3^- photolysis compared to HNO_3 photolysis, with this enhancement expressed as $f = \frac{j_{pNO_3^-}}{j_{HNO_3}}$, where $j_{\mathrm{pNO_3^-}}$ is the photolysis of pNO_3^- and $j_{\mathrm{HNO_3}}$ is the photolysis of gas-phase HNO_3. Field measurements and lab studies have proposed a wide range of values for the enhancement factor f, with some studies suggesting that the photolysis of pNO_3^- is not a significant source of HONO in the atmosphere [141, 142, 145, 146]. Different factors are thought to affect f, with studies focusing particularly on the effect relative humidity (RH) and aerosol composition have on f [136–138, 140–142, 145–154].

The pNO_3^- loading has been found to be inversely proportional to f, with stronger enhancements seen at smaller pNO_3^- concentrations [136, 137, 140]. Surface-bound NO_3^- photolyses more rapidly than bulk NO_3^-, due both to the alignment and orientation that nitrate molecules have at the surface, which leads to a large absorption cross section, and to incomplete solvent cage effects at the surface, which lead to higher quantum yields as the photolysis products can diffuse out of the solvent cages more rapidly making nitrate recombination less likely

[143, 144, 155, 156]. As such, the enhancement of pNO_3^- photolysis is dependant on the surface availability of pNO_3^-, and therefore likely on the partitioning between surface-bound and bulk nitrate. Molecular dynamic simulations have found contradicting results in terms of the surface propensity of nitrate anions [157, 158], however lab studies have shown that, due to the surface affinity of halide anions, cations are attracted to the surface, which in turn draw NO_3^- to the air/water interface [154, 159–162]. Andersen *et al.* and Rowlinson *et al.* (*in prep*) have used the Langmuir adsorption isotherm, the bulk pNO_3^- concentrations and the missing HONO production to develop parametrisations to capture the relationship between f and pNO_3^- loading [136].

As mentioned above, other factors are known to also affect f, with an increase in HONO and NO_2 production from pNO_3^- photolysis seen at higher RH, lower pH and in the presence of cations, halide anions and photosensitive organic compounds [137, 140, 146, 150–154, 161], however these effects have mainly been observed in lab studies and have not been quantified in atmospheric measurements, where a large variety of factors are at play.

This chapter presents two new sets of measurements of HONO at the Cabo Verde Atmospheric Observatory (CVAO) in February 2023 and September 2024, and compares them to previous HONO measurements conducted at the site [136, 163]. The ability of photostationary state (PSS) HONO values to reproduce measured HONO mixing ratios, when considering only gas-phase HONO production (R 5.4) and when including the photolysis of pNO_3^- (R 5.5) as a source of HONO, is also examined. The enhancement of pNO_3^- compared to HNO_3 is included through the parametrisations for f developed by Andersen *et al.* and Rowlinson *et al.* (*in prep*) [136]. As measurements of RH and the aerosol composition were also available during the measurement periods, analysis has been carried out to determine whether any other factors were affecting the enhancement of pNO_3^- during HONO measurements at the CVAO.

5.2 Experimental

Nitrous acid, HONO, was measured at the Cabo Verde Atmospheric Observatory (CVAO, described in section 2.2) in February 2023 and in September 2024 using a Long Path Absorption Photometer (LOPAP-03, QUMA Elektronik & Analytik GmbH). Section 5.2.1 describes the operating principle of the LOPAP, sections 5.2.2 and 5.2.3 describe the LOPAP experimental set-up and data processing

steps for the February 2023 and September 2024 campaigns, respectively, and section 5.2.5 describes supplementary measurements carried out at the CVAO alongside the HONO measurements.

5.2.1 The Long Path Absorption Photometer

Operating principle

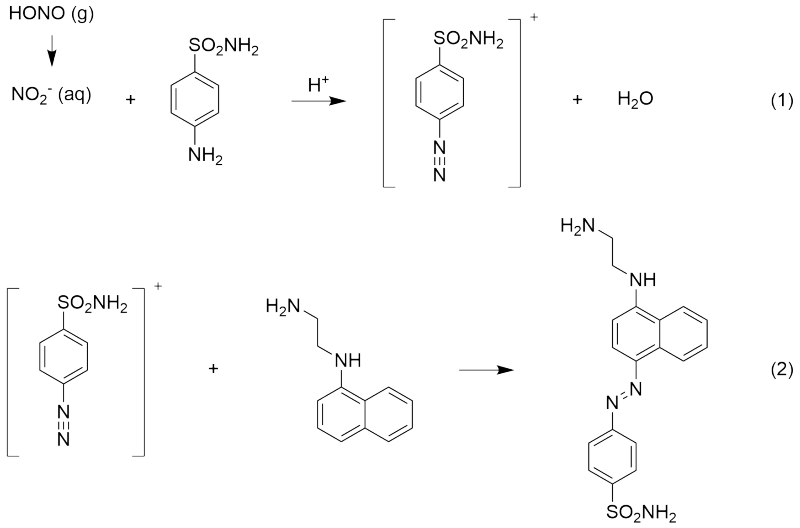

Figure 5.1: Reaction between aqueous NO_2^- and sulfanilamide (1) in the liquid reagent to produce a diazonium salt, which then reacts with N-(1-naphthyl)-ethylenediamine-dihydrochloride (2) to produce an azo dye.

The Long Path Absorption Photometer (LOPAP), first described in Heland *et al.*, utilises a wet chemistry technique to measure nitrous acid (HONO) [164]. Upon contact with an acidic sulfanilamide reagent (sulfanilamide in 1 M HCl, 10 g L^{-1}), gaseous HONO reacts rapidly with sulfanilamide to produce a diazonium salt, which then reacts with N-(1-naphthyl)-ethylenediamine-dihydrochloride, as shown in figure 5.1, yielding an azo dye [165]. The amount of azo-dye formed is proportional to the mixing ratio of HONO in the sampled air and can be quantified through spectroscopy.

Instrument design

This technique avoids measurement offsets due to heterogeneous reactions leading to the formation of HONO in sampling lines, by pumping reagent R1 (sulfanilamide dissolved in 1 M HCl) to the inlet box, where it reacts with HONO in

the sampled air in a glass stripping coil. Other NO_z species can also react with sulfanilamide to yield the diazonium salt, however due to the acidic nature of R1 (pH $\approx$ 0) their uptake to this solution is slow, and the reaction with sulfanilamide is not fast enough to overcome the slow uptake. By using two channels (figure 5.2), with two stripping coils placed in series, the offsets due to interfering species forming the diazonium salt can be quantified and removed from the final HONO mixing ratio. As the reaction between HONO and sulfanilamide is very fast (99.4% HONO uptake with a gas/liquid contact time of $\sim$ 30ms), practically all the HONO present in the sampled air is taken up in the first channel [166]. The uptake to reagent 1 for other NO_z species is much slower and is expected to be constant across the two channels. Therefore the signal in the first channel is from HONO and interfering species, the signal from the second channel is solely due to interfering species. By subtracting the signal from channel 2 from the signal from channel 1, an interference-free HONO measurement is obtained.

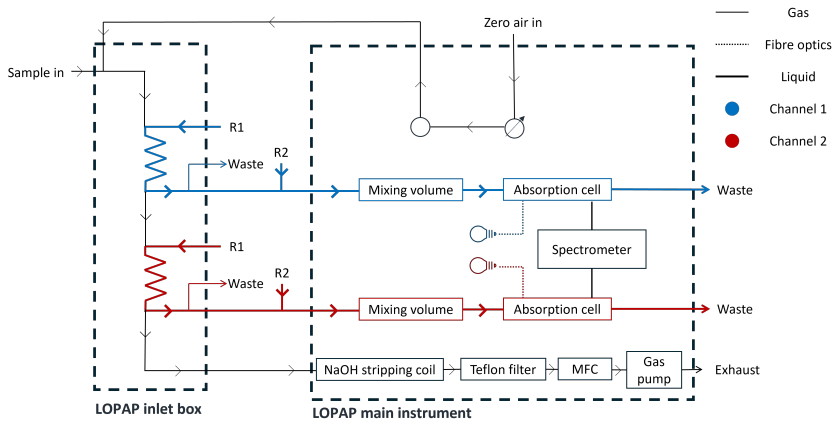

Figure 5.2: Schematic of the LOPAP. Thin, black lines indicate gas flows, coloured, bold lines indicate liquid flows, with blue indicating channel 1 and red indicating channel 2. Dotted lines indicate fibre optics.

After coming into contact with the sampled air in the inlet box, the solution containing the diazonium salt is pumped back down into the main instrument, where it mixes with reagent R2 (N-(1-naphthyl)-ethylenediamine-dihydrochloride dissolved in water) in the mixing volume. The azo-dye produced from reaction 2, shown in figure 5.1, is then pumped to the absorption cell, a long piece of Teflon tubing. LEDs (one for channel 1, one for channel 2) produce visible light, which is focused into the absorption cell tubing using fibre optics, undergoing multiple total reflections before it is absorbed by the liquid. At the end of the long piece of Teflon tubing, the light is detected by a spectrometer and

the absorption of the liquid, proportional to the amount of HONO in the sampled air, is measured. Air bubbles in the absorption cell tubing interfere with the reflections of light in the liquid and disrupt measurements, therefore debubblers are placed after the stripping coils in the inlet box and after the mixing volumes in the main instrument.

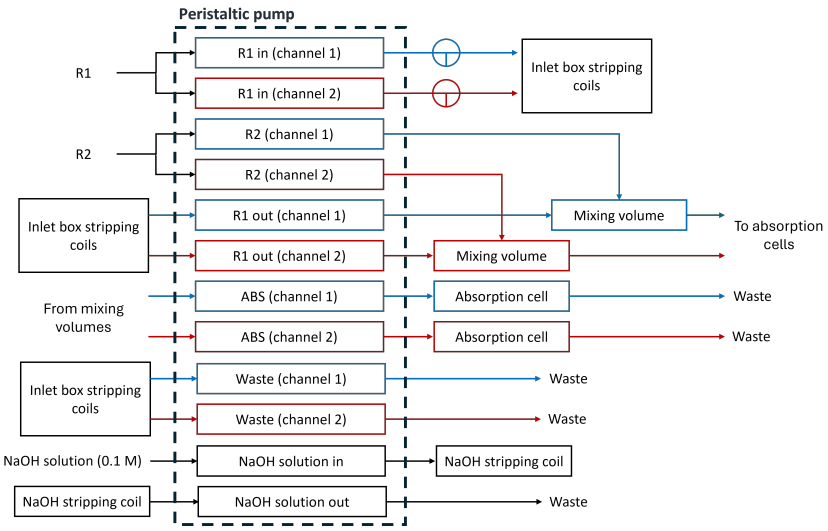

Figure 5.3: Schematic of the LOPAP peristaltic pump. Blue is used for channel 1, red is used for channel 2 and black is used for other flows (NaOH solution).

The schematics in figures 5.2 and 5.3 show the instrument and the peristaltic pump, used for the liquid flows. The gas pump for the LOPAP is housed within the main instrument, as is a mass flow controller (MFC), used to regulate the flow rate of the sampled air (with a range between 500 and 2000 mL min^{-1}). In order to protect the gas pump and the MFC from aerosol particles and HCl vapour in the air flow from the inlet box, a stripping coil containing a 0.1 M NaOH solution and a Teflon filter are placed upstream of the MFC and the gas pump.

Zeroing

As can be seen in figure 5.2, zero air (from a N_2 or a ZA gas cylinder) is used to zero the instrument at the inlet. A needle valve is used to adjust the flow of the ZA so that it is slightly above the instrument's flow rate, in order to overflow the inlet (ZA flow of 1200 mL min^{-1} if the instrument's pump is pulling 1000 mL min^{-1}). A solenoid valve is used to start and stop zeroes and can be set to automatically begin a zero measurement after a set amount of time. When sampling in regions with low HONO mixing ratios (such as the CVAO), the instrument should be

zeroed roughly every 6 hours.

Calibrations

In the field, calibrations are carried out using a liquid NO_2^- standard, rather than a gaseous HONO source, as detailed in Kleffmann *et al.* [166]. The calibration solution is made by diluting the NO_2^- standard using water and R1, resulting in a final calibration solution with a concentration of 0.01 mg/L. During a calibration, under ZA, R1 is replaced with the calibration solution and the absorption for a known amount of NO_2^- is measured. Calibrations need to be carried out when there are changes to any of the instrumental parameters (for example, new reagents, new 3-stop tubing in the peristaltic pump, changes to the LED intensity or changes to the integration times). This is done to ensure that calibrations are performed under the same conditions as the measurements. In general, reagents and peristaltic tubing are changed at the same time, along with the settings for LED intensity and integration times, however instrumental issues may arise that require any of these to be changed independently of the others.

Along with NO_2^- calibrations, the liquid flows also need to be calibrated. This is done by replacing R1 with water, closing the absorption cell pathway (to avoid air bubbles getting into the absorption cell) and turning the T-valves (shown in figure 5.3) so that the liquid does not flow up to the external sampling unit, but can instead be collected in a 5 mL volumetric flask. The amount of time it takes for the volumetric flask to fill up is measured and can then be used to calculate the liquid flow rate. The liquid flow calibrations are performed when changes are applied to the peristaltic pump, such as changing the liquid flow rate or the 3-stop tubing (which lasts roughly 3 weeks).

5.2.2 February 2023 measurements

Campaign instrument set-up

In February 2023, measurements of HONO, OH, hydroxy and peroxy radicals (HO_2 and RO_2) were taken at the CVAO, as part of the PEROXY measurement campaign, introduced in section 4.2.2. OH, HO_2 and RO_2 were measured using fluorescence assay by gas expansion (FAGE), by Dr Lisa Whalley, Dr Graham Boustead, Dr Samuel Seldon and Dr Rachel Lade, from the University of Leeds (see section 5.2.5). HONO was measured using the LOPAP, which was running

from 7th to 26th February.

Figure 5.4: LOPAP inlet (framed by the red box) on top of the FAGE container at the CVAO during the February 2023 campaign.

The LOPAP inlet box was placed on top of the FAGE container facing the prevailing wind (figure 5.4, roughly 3 m above ground level), to ensure that it was at the same sampling height as the HO_2, RO_2 and OH measurements. The instrument itself was placed in the guest lab at the CVAO, which was temperature controlled and kept at around 18° C. A refrigerated bath circulator (ARCTIC A10 Refrigerated Circulator, Thermo Scientific) was used with distilled water and a temperature set point of 15° C, to cool the stripping coil at the inlet and avoid any condensation in the gas line.

The gas flow was set at 1000 mL min^{-1} and the liquid flow was set at 10 rpm. After the campaign, the instrument's internal MFC (Bronkhorst, LOW-ΔP-FLOW F-201EV) was calibrated by measuring the gas flow at the inlet with a flow meter (Alicat, MB-50SLPM-D-ROHS/5M) across a range of set points (from 500 to 1500 mL min^{-1} in increments of 250 mL min^{-1}). The measured flow was ∼ 97% of the instrument's set point therefore a correction was applied to the gas flow when processing the data.

Campaign calibrations

During this campaign, the LOPAP was calibrated three times, using the same Titrisol nitrite standard (1000 mg of $NaNO_2$ in H_2O diluted to a 0.01 mg L^{-1} NO_2^- solution using water and R1) for all three calibrations. The first calibration was performed on 9th February, after measurements with the first of two batches of reagents began on 7th February. This calibration was carried out with the same integration times and LED intensities that had been used for the measurements on the previous days, however, due to air entering the absorption cell on the night of

8th February, the spectra were shifted. After the calibration was carried out, the integration times were changed to readjust the spectra, and a new calibration with these settings was conducted on 11th February. A new set of reagents was made up on 17th February, along with changes in the 3-stop tubing and integration times. The calibration with these new settings was carried out on 21st February.

Campaign zeroes

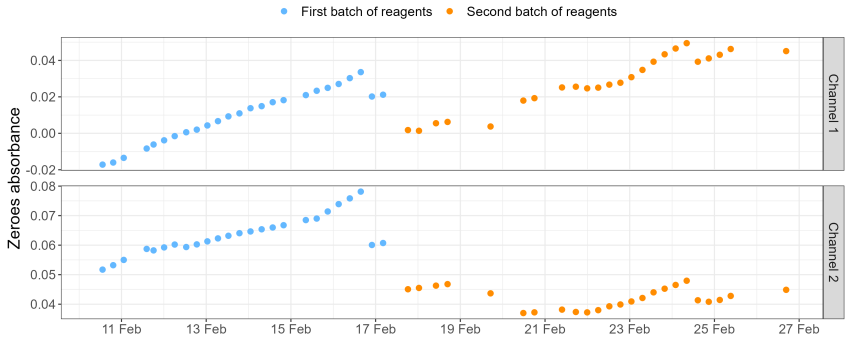

Figure 5.5: ZA zeroes measured in February 2023, divided into panels based on the measurement channel and coloured by the reagent batch used.

The instrument was zeroed with N_2 (N5 purity) every 6 hours for 30 minutes (figure 5.5). The upward baseline drift seen with both batches of reagents is thought to be due to an increase in absorbance as the Teflon tubing becomes dirtier and the 3-stop peristaltic tubing loses its elasticity. When changing between batches of reagents, the system is flushed with water for a few hours, the 3-stop tubing is changed and the absorption spectra are adjusted, therefore a step change in zeroes between reagent batches is expected. The other step changes seen in the zeroes occur after interruptions in measurements due to instrumental issues, mainly air bubbles entering the absorption cell. In order to remove the air bubbles, water is pushed through the absorption cell using a syringe, likely cleaning the absorption cell in the process.

Figure 5.5 shows that the ZA zeroes in channel 2 are significantly lower with the second batch of reagents, however this is not the case for the ZA zeroes in channel 1. A larger number of instrumental issues were encountered with the second batch of reagents, including a power cut on the evening of 18th February.

The plot in figure 5.6 shows the 5-minute averaged timeseries of HONO measured at the CVAO in February 2023, zeroed both with ZA values and night-time (between 21:00 and 04:00 UTC) values. Previous HONO measurements in

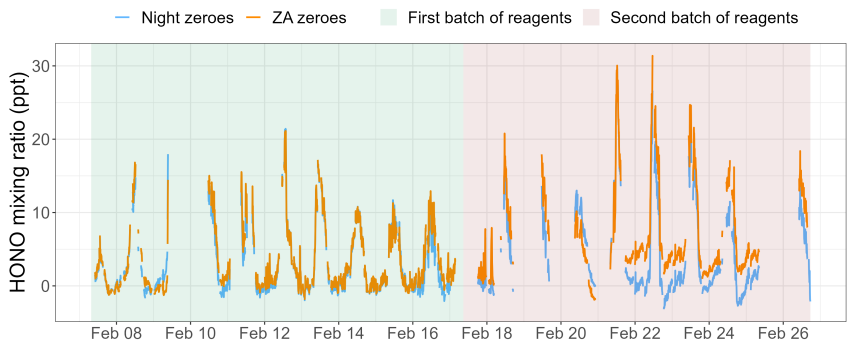

Figure 5.6: Five minute average HONO mixing ratios timeseries, zeroed using ZA (orange) and nighttime (blue) values, with background shading to indicate if data were collected using the first or second batch of reagents.

the clean, remote MBL show that nighttime HONO mixing ratios are expected to tend towards 0 ppt, as the main HONO production pathways (R 5.4 and R 5.5, discussed in section 5.1) are photochemical or involve reaction with OH whereas loss through dry deposition (R 5.2) occurs at night and depletes HONO without it being able to regenerate in the absence of sunlight [136, 138, 163]. Using nighttime values to zero measurements made with the first batch of reagents does not result in a large difference compared to the HONO mixing ratios calculated when zeroing with ZA values. HONO mixing ratios calculated using the ZA values for the second batch of reagents, however, show mixing ratios between 2.5 and 5 ppt at night, clearly diverging from the HONO mixing ratios calculated using nighttime zeroes. Given the lower ZA zeroes in channel 2 with the second batch of reagents (figure 5.5) and previous studies, as well as measurements during this campaign with the first batch of reagents, showing that nighttime HONO in this environment is expected to be around 0 ppt, HONO mixing ratios for the second batch of reagents have been calculated using nighttime values as zeroes.

5.2.3 September 2024 measurements

HONO was measured at the CVAO between 6th and 19th September 2024. The instrument was placed in the guest lab, as described in section 5.2.2, and the inlet was placed on a wooden crate attached to the guest lab roof, at roughly the same height and orientation as during the February 2023 campaign (figure 5.7). The liquid flow was set at 10 rpm and the gas flow was set at 1000 mL min^{-1}, however during the campaign there were problems with the gas flow, discussed below.

Figure 5.7: The LOPAP inlet box placement during the September 2024 measurement campaign.

Gas flow issues

Prior to the campaign, the internal MFC was calibrated, showing that the measured gas flow at the inlet (measured with an Alicat, MB-50SLPM-D-ROHS/5M flow meter) was $\sim 83\%$ of the set point. During the measurement campaign, the gas flow was checked using a red-y flow meter (GCR-B9EA-BA15) and it was seen to vary from 800 to 1500 mL min^{-1} throughout the measurement period. The MFC in the instrument is not set up to log gas flow, and there were no MFCs available at the CVAO that could be set up to log the gas flow. The red-y flow meter was plumbed into the instrument, upstream of the internal MFC, and the gas flow values were noted roughly every 30 minutes whilst on-site. Once the instrument was back in York, the internal MFC was calibrated using a gas flow calibrator (Mesa Defender 530+ M) both at the inlet and upstream of the internal MFC, where the flow meter had been placed whilst at the CVAO. These measurements showed that, across the range of set points, the gas flow was $\sim 10\%$ lower at the inlet, likely due to leaks between glass and Teflon tubing.

Figure 5.8 shows the measured gas flows at the CVAO, corrected to account for the lower flows at the inlet compared to flows measured upstream of the internal MFC. During the campaign, it appears that the gas flows varied with the time of day, potentially indicating that a change in temperature, pressure or humidity across the day was affecting either the LOPAP's internal MFC or the red-y flow meter used to measure flows.

Measurements in the lab after the September 2024 campaign, using an Alicat flow meter set up to log the gas flow at the inlet, show that over four days

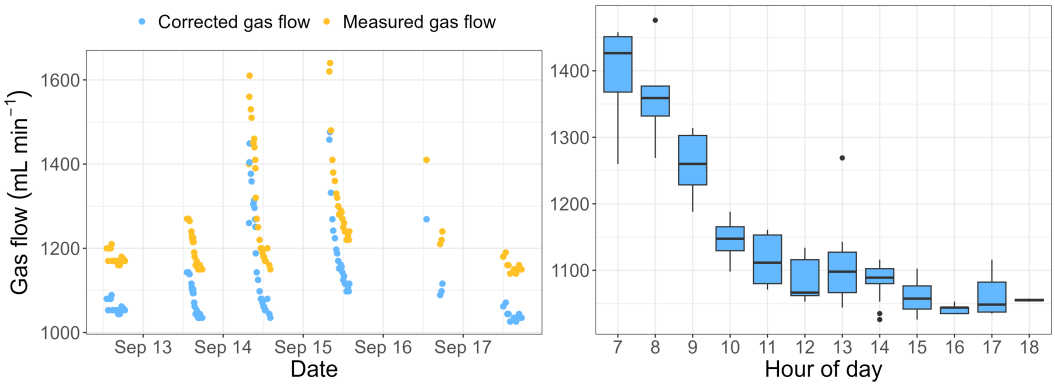

Figure 5.8: Timeseries of manually logged gas flows during the September 2024 campaign, corrected to account for the lower measurements at the instrument's inlet compared to upstream of the LOPAP's MFC (left) and a boxplot of gas flows measured during different hours of the day (right).

the gas flow does not show much variability (figure 5.9). The flow meter was also measuring temperature and pressure, and whilst these did not show much variation in a temperature controlled lab, the lowest gas flows were seen when the temperature was lowest. A clear increase in the gas flow was seen when the liquid flows were stopped around 16:00 on 10th January (marked by the red line in figure 5.9), indicating that perhaps disruptions to the liquid flow whilst out in the field, caused by blockages, could also have affected the gas flow, however the change in gas flow seen in the lab was much smaller than the range of gas flows seen during the campaign.

Whilst the lab tests did not conclusively find the reason behind the fluctuations in the gas flow, the values measured during the campaign are considered genuine

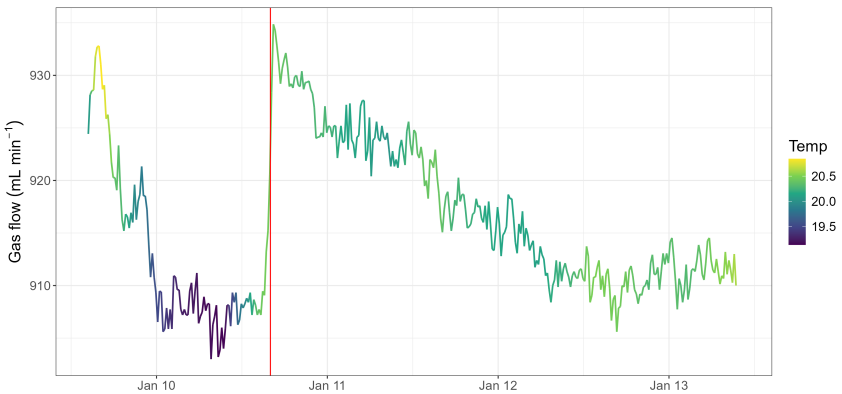

Figure 5.9: Timeseries of gas flows at the LOPAP inlet, logged using an external flow meter, coloured by temperature in °C. The red line indicates when liquid flows were stopped in the instrument.

and the average of the measured gas flows, 1128 mL min^{-1}, was used as the gas flow throughout the campaign during data processing. The HONO mixing ratios were also calculated using the hourly averaged gas flow values, shown in the boxplot in figure 5.8, and there was very little difference between the HONO mixing ratios calculating assuming a constant or a changing gas flow, as shown in figure 5.10. As there are no measurements of overnight changes in the gas flow during the campaign and the difference between the two data processing methods is small, the HONO measurements have been processed using a gas flow of 1128 mL min^{-1}.

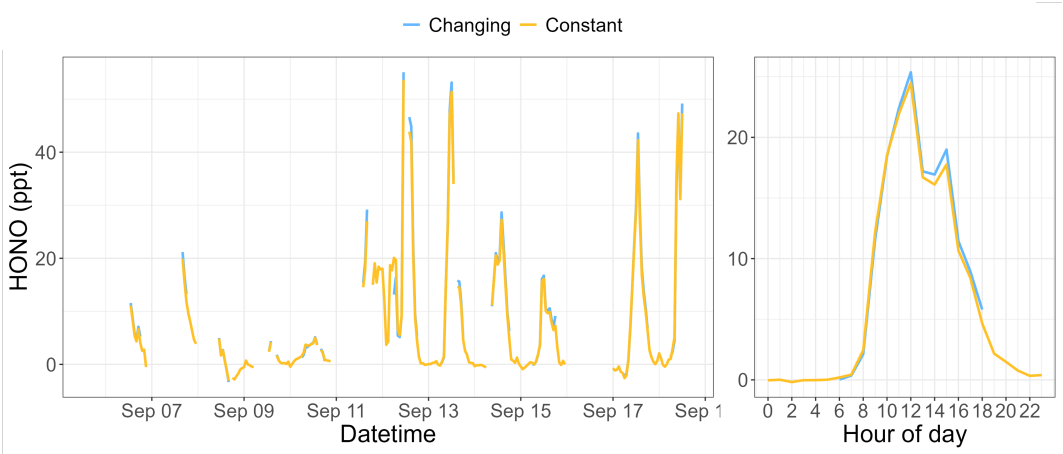

Figure 5.10: Hourly averaged timeseries (on the left) and diurnal cycle (on the right) of HONO mixing ratios calculated assuming the gas flow was constant during the measurement period (in yellow) and assuming that the gas flow varied with hour of day (shown in the boxplot in figure 5.9, in blue here).

Campaign calibrations

The instrument was calibrated three times during this campaign, using a nitrite standard solution ($NaNO_2$ in H_2O, 1000 mg L^{-1}, traceable to SRM from NIST), diluted to 0.01 mg L^{-1} using water and R1. The first calibration was performed on 9th September, after measurements began on 5th September. A second calibration was performed on 13th September, after the first discrepancy with the gas flow was spotted. A final calibration was carried out on 14th September, following an adjustment in the spectra integration times, which had shifted due to air bubbles entering into the absorption cells. Only one set of reagents was used during this campaign.

Campaign zeroes

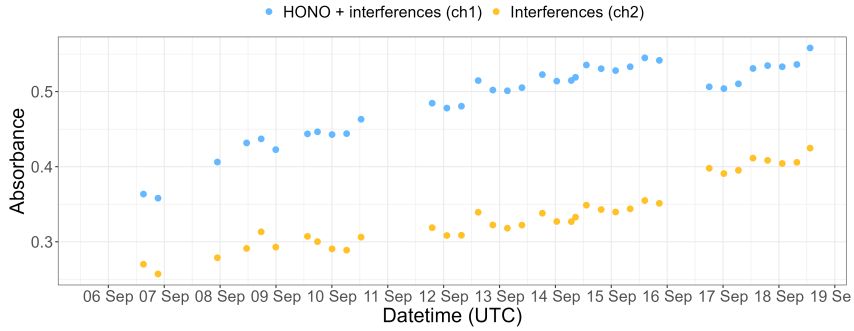

Figure 5.11: Average values from ZA zeroes measured in September 2024 in channel 1 (blue) and channel 2 (yellow).

The LOPAP was zeroed with N_2 (N5 purity) for 30 minutes every 5 hours and 45 minutes. The flow of zero air (ZA) was adjusted using a needle valve to overflow the inlet (ZA flow $\sim$ 1200 mL min^{-1}), however as discussed above, the LOPAP's gas flow was variable during the campaign therefore there could be instances when the ZA was not overflowing the inlet during a zero. The ZA flow was increased to 1800 mL min^{-1} on 11th September when the variable gas flows were first noticed, however, as shown in figure 5.11, the averaged zero values from this campaign appear to show a diurnal trend, especially when compared to measurements from the February 2023 campaign (figure 5.5).

Figure 5.12 shows the 5-minute averaged HONO mixing ratios from the September 2024 campaign, zeroed with ZA and nighttime values. When using the ZA zeroes to process the data, nighttime values are around 5 ppt (excluding measurements from 11th and 12th September, during a local pollution event). This is similar to the nighttime values measured during the second half of the February 2023 campaign (figure 5.6) and could perhaps be indicative of an instrumental issue. A different N_2 cylinder was used in both campaigns, and between the campaigns a leak was identified in the ZA line and fittings on the solenoid valve were replaced. Measurements from the first half of February 2023, as well as previous HONO measurements at the CVAO have shown that in this environment HONO is expected to be virtually zero overnight (except in the case of local emissions), therefore the nighttime values have been used to zero these measurements.

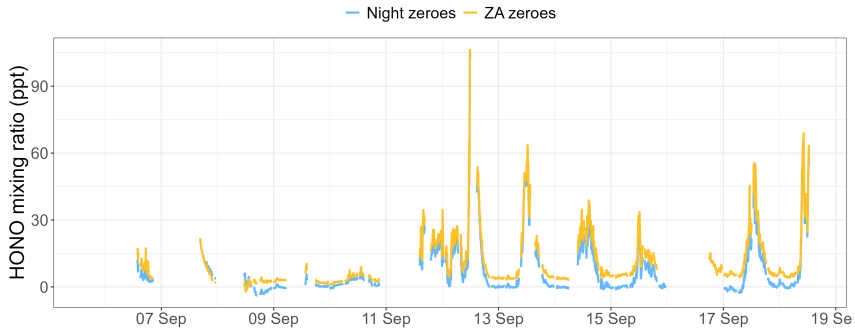

Figure 5.12: Five minute average timeseries of HONO mixing ratios during the September 2024 campaign, measured using nighttime (blue) and ZA (yellow) values to process the raw data.

5.2.4 HONO uncertainty analysis

Uncertainties in HONO measurements arise from the precision of the instrument and uncertainties in the calibration (equation 5.1). The uncertainties due to the gas and liquid flows are included in the calibration uncertainty, as the NO_2^- concentration during the calibration is calculated based on the diluted NO_2^- standard concentration, the liquid flows and the gas flows (equation 5.2).

$$\text{HONO Uncertainty} = \sqrt{\text{Precision}^2 + \text{Cal uncertainty}^2} \tag{5.1}$$

The precision of the instrument is determined from the noise during zeroes (2σ during ZA zeroes for the first half of the February 2023 campaign and nighttime zeroes for the remainder of the February 2023 campaign and the September 2024 campaign). As the HONO data is hourly averaged, the precision of the instrument was calculated by looking at the variability between one hour over night (between 22:00 and 23:00 UTC), to match the HONO averaging time.

Uncertainties in the calibration are due uncertainties in the NO_2^- concentration during the calibration, in the absorbance during the calibration and in the absorbance during the pre-calibration zero measurement. The uncertainties in the absorbance during the calibration and during the pre-calibration zero are calculated assuming a normal distribution of uncertainty, using $\frac{2\sigma}{\sqrt{\text{count}}}$ over the calibration and pre-cal zero periods. The NO_2^- concentration during the calibration is calculated from the concentration of the diluted NO_2^- standard, the gas flow and the liquid flow (equation 5.2).

$$\mathrm{NO_2^-cal\ conc\ (in\ ppt)} = \frac{\frac{\text{diluted } \mathrm{NO_2^-} \text{ conc} \times \text{liquid flow rate}}{\mathrm{NO_2^-} \text{molar mass} \times N_A}}{\text{gas flow rate} \times R \times N_A} \times 10^{12} \tag{5.2}$$

The NO_2^- standards used have an uncertainty of $\pm 0.7\%$, with a final uncertainty of $\pm 0.79\%$ once uncertainties in the glassware used for diluting the standard have been included. The internal MFC is quoted as having an accuracy of $\pm 1\%$ FS, therefore the uncertainty will be $\pm 2\%$ as the MFC range is 500 to 2000 L min^{-1} and the gas flow was set at 1000 mL min^{-1} during both campaigns. The uncertainty due to liquid flows is not easily quantifiable and was assumed to be $\pm 5\%$ based on work by Kleffmann *et al.*, who found that there was a relative uncertainty of $\pm 10\%$ in each channel, due to uncertainties in the gas flow rate, the liquid flow rate and the calibration [167]. The uncertainties associated with the calibration are all calculated as percentages so that they can be combined using error propagation, and then they are converted to ppt to be combined with the other uncertainties associated with LOPAP measurements. An added uncertainty term to account for the variation in gas flows during the September 2024 campaign was included in the form of the % difference between the mean gas flow and the measured gas flows during the campaign (calculated as $\sim 7\%$).

Table 5.1: A summary of the mean HONO limit of detection (LOD) (2σ, 30 s) and uncertainty during the February 2023 and September 2024 measurement campaigns.

Measurements	LOD (mean $\pm 2\sigma$)	Uncertainty (mean $\pm 2\sigma$)
Feb 2023, ZA zeroes	0.15 ± 0.22 ppt	0.33 ± 0.46 ppt
Feb 2023, night zeroes	0.85 ± 1.41 ppt	0.96 ± 1.41 ppt
Sep 2024, night zeroes	0.99 ± 0.77 ppt	1.50 ± 1.89 ppt

Table 5.1 shows the LOD and uncertainty ($\pm 2\sigma$) for HONO measured during the February 2023 and September 2024 campaigns, distinguishing between data that have been zeroed using ZA and night zeroes. The variability seen with an hour of overnight values is higher that the variability across a 30 minute zero. The higher LODs seen with nighttime values are likely due to the longer period used to zero the instrument (an hour compared to 30 minutes). This indicates low stability in the measurements conducted using the LOPAP, which can be attributed to irregularities in the gas and liquid flows, as well as small blockages or air bubbles, all of which may affect the measurements.

5.2.5 Supplementary measurements

A full description of NO_x measurements at the CVAO can be found in chapter 2, which also gives an overview of the CVAO (section 2.2.1) and the met data (relative humidity, wind speed and wind direction) collected at the site (see table 2.1) and used in this chapter.

Photolysis rates

The photolysis rates (j_{HONO} and j_{HNO_3}) were calculated using Python code written by Dr Lisa Whalley (University of Leeds), which uses absorption cross sections and quantum yields to determine photolysis rates based on the measured solar UV flux at the CVAO using a 2-pi sr quartz diffuser coupled to an Ocean Optics spectrometer (described fully in section 4.2.1). During periods when data were lost due to instrumental issues (between the 15th and the 20th February 2023 and between 13th and 16th September 2024) j_{HONO} and j_{HNO_3} were calculated using the monthly correlation of photolysis rates with solar radiation for each hour between 09:00 and 17:00. The slope of this correlation is used as the error for the calculated j_{HONO} and j_{HNO_3}. Further details can be found in appendix A.

OH measurements

The PEROXY measurement campaign, which took place in February 2023 is introduced in section 4.2.2. Briefly, OH measurements were collected by Dr Lisa Whalley, Dr Graham Boustead, Dr Samuel Seldon and Dr Rachel Lade from the University of Leeds, using FAGE, described in Dr Samuel Seldon's thesis [103]. During this campaign, OH measurements had a 2σ accuracy of 21%. OH measurements were not collected during the September 2024 campaign, so the mean midday OH from February 2023 (2×10^6 molecules cm^3) was used when analysing these data.

Aerosol measurements

Aerosol composition data from the CVAO, which are measured by the Leibniz Institute for Tropospheric Research (TROPOS), were used in the analysis presented in this chapter. The instruments and methods used to collect aerosol filters and determine the ion concentrations are described in Fomba *et al.* [168]. Aerosol pH was determined by measuring the water-soluble extract of the filters using a

Sartorius PP-20 pH meter, described fully in Fomba *et al.* (*in prep*). Measured pH values have been compared with those estimated by the E-AIM model and have been found to be in good agreement.

5.3 Results

5.3.1 February 2023 HONO measurements

The hourly HONO and NO_x timeseries for February 2023 are shown in figure 5.13. During the campaign, wind speeds ranged from 3.8 to 11.8 m s^{-1} and the wind direction was always north-eastern (between 25° and 80°), meaning that baseline data were measured throughout the campaign and no periods had to be flagged as affected by local contamination (see section 2.2.1 for the baseline criteria at the CVAO).

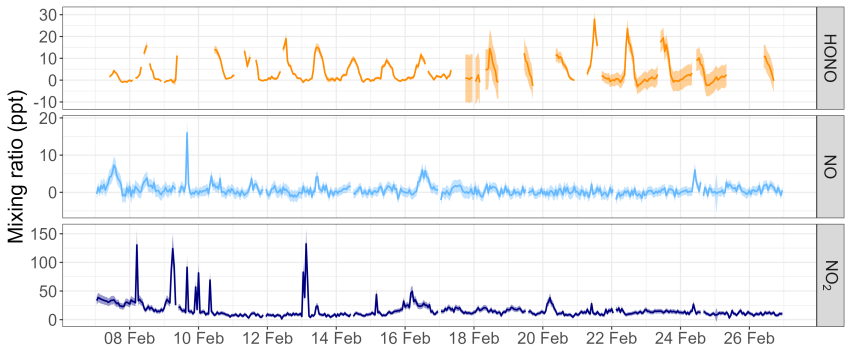

Figure 5.13: Hourly average HONO, NO and NO_2 mixing ratios during the February 2023 measurement campaign, with the shaded area representing ± measurement uncertainty.

The highest HONO concentrations are seen between 21st and 23rd February, days that also have significant Saharan influence (between 18% and 27%, shown in figure 5.14). However, the air masses reaching the site on 7th and 8th February also have high Saharan influence (31% and 27%, respectively), but this does not result in higher HONO mixing ratios on these days.

Figure 5.15 shows that during the campaign, there is no clear relationship between the amount of Saharan air reaching the site and the mean midday (between 11:00 and 15:00 UTC) HONO, NO and NO_2 mixing ratios during this campaign. In particular, HONO mixing ratios on days where there was a significant amount of Saharan influence (>10%) show a very wide spread. Of the

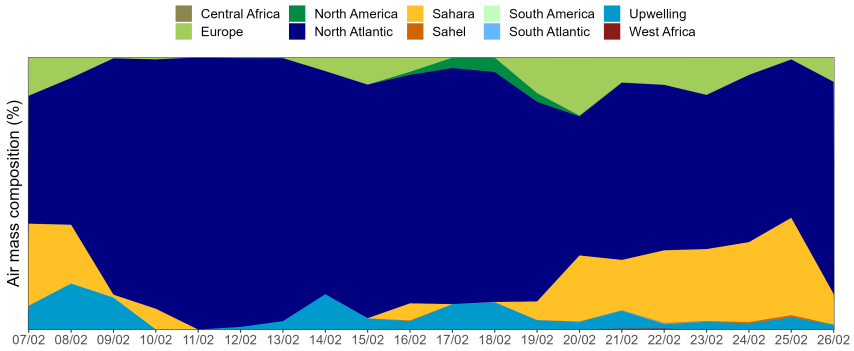

Figure 5.14: Daily air masses at the CVAO during the February 2023 measurement campaign. The map defining the regions is shown in figure 2.3

17 days during which midday HONO measurements are available, 9 had more than 10% Saharan air reaching the site, so the broad spread could in part be due to the fact that more data points are considered. Different amounts of European air reach the site on days that have significant (>10%) Saharan influence, meaning that some aged pollution has reached the site and could also be affecting HONO and NO_x mixing ratios.

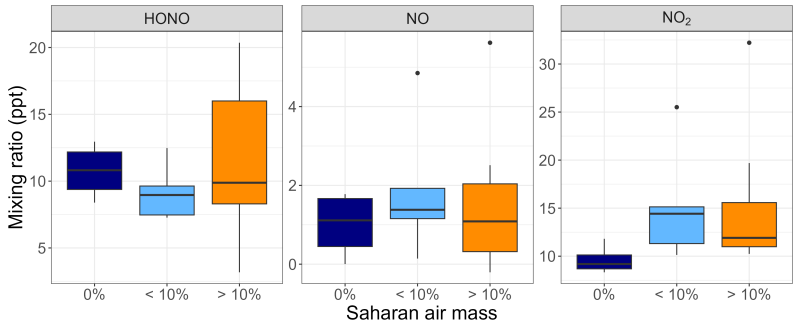

Figure 5.15: Daytime NO, NO_2 and HONO mixing ratios on days with no Saharan influence, low Saharan influence and significant Saharan influence (between 10% and 35%).

The lack of a clear relationship between HONO and Saharan air masses could indicate that mineral oxides (TiO_2 or ZnO) in Saharan dust acting as photocatalysts and initiating photochemical processes that lead to HONO and NO_x production are not a significant source in the remote MBL, as had been proposed previously [169, 170]. The amount of datapoints are not enough to conduct a full air mass composition study, as was performed on the NO_x data in section 4.3.2.

Diurnals from February 2023 are shown in figure 5.16. The NO_2 peak in

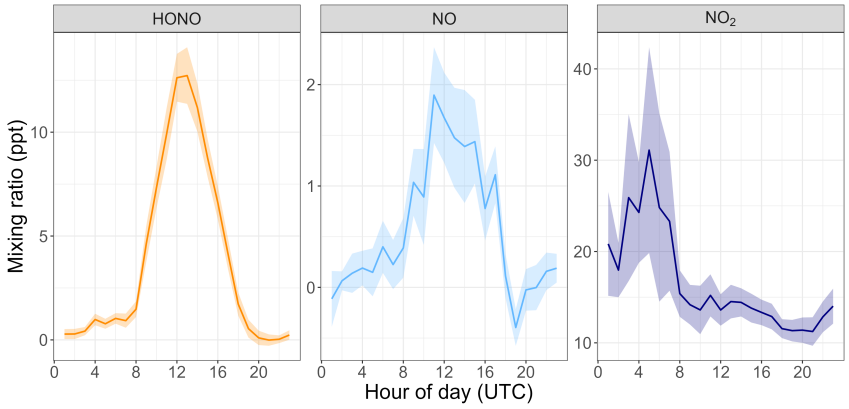

Figure 5.16: Diurnal plots of HONO, NO and NO_2 during the February 2023 measurement campaign, with shaded areas representing ± SE.

the morning is driven by NO_2 spikes early in the campaign (between 8th and 13th February), which are not seen in the HONO or NO measurements. Both HONO and NO diurnals have a midday maximum and a nighttime minimum, around 0 ppt, confirming that in the clean marine atmosphere, the main source for both HONO and NO is photochemical. The fact that the midday peak is much higher for HONO than it is for NO further suggests that the main source of HONO at the CVAO is not the reaction between OH and NO (R 5.4), but instead that an alternative photochemical pathway exists, as discussed in section 5.1.

5.3.2 September 2024 HONO measurements

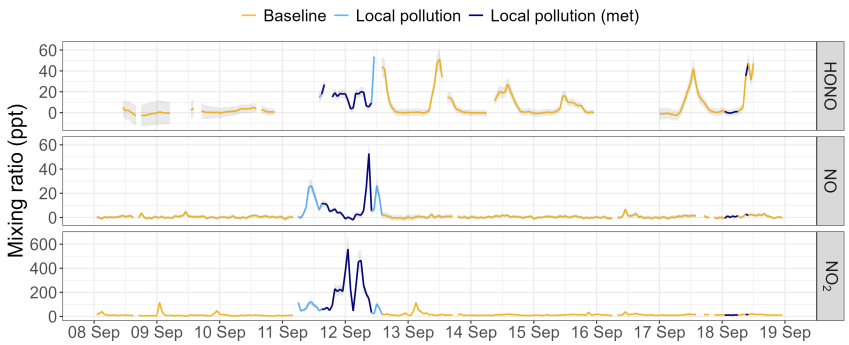

Figure 5.17: Hourly average HONO, NO and NO_2 mixing ratios during the February 2024 measurement campaign, with the shaded area representing ± measurement uncertainty. Data in yellow were collected during baseline conditions, data in blue were collected during a local pollution event (identified using wind speed and direction in dark blue and using mixing ratios in light blue).

HONO, NO and NO_2 timeseries measured at the CVAO during the September 2024 campaign (between 8th and 19th September) are shown in figure 5.17. The data have been coloured based on whether they were were measured during baseline conditions or during a local pollution event. Very high mixing ratios of NO, NO_2 and HONO were observed between the 11th and the 13th September, with low wind speeds (> 2 m s^{-1}) and wind reaching the site from over the island. High mixing ratios of all three species are also observed for a few hours slightly before and after the pollution event, therefore these data have also been flagged since during these periods wind speeds were still quite low or the wind direction was close to 100°.

Figure 5.18 shows a plot of the baseline HONO and NO_x data from the campaign. HONO mixing ratios are still high during 12th and 13th September, however there is no evidence that these high mixing ratios are caused by local pollution, as NO mixing ratios are stable below 5 ppt and the spike seen in NO_2 does not correspond with the higher HONO mixing ratios.

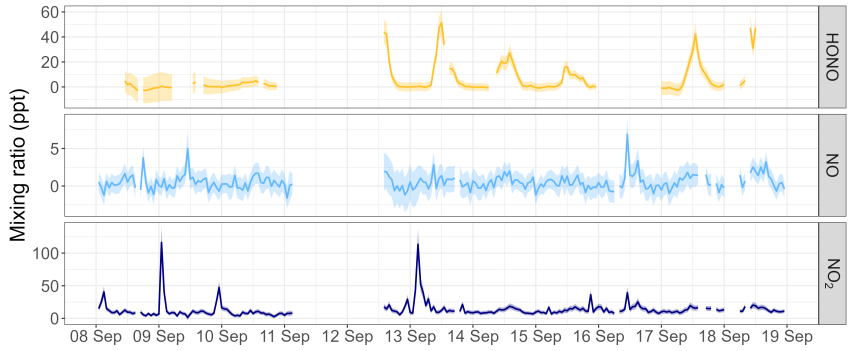

Figure 5.18: Hourly average baseline HONO, NO and NO_2 mixing ratios during the September 2024 measurement campaign, with the shaded area representing ± measurement uncertainty.

The air masses reaching the CVAO during the campaign (shown in figure 5.19) predominantly travelled to the site over the ocean, with very little Saharan, European and North American influence, therefore with little aged pollution reaching the site. There is no indication therefore that higher Saharan dust loadings were reaching the site on the days when higher HONO mixing ratios were seen.

It is possible that contamination inside the LOPAP from the local pollution event resulted in artificially higher HONO mixing ratios in the following days, however the fact that a diurnal cycle is still clear in this period would imply that a

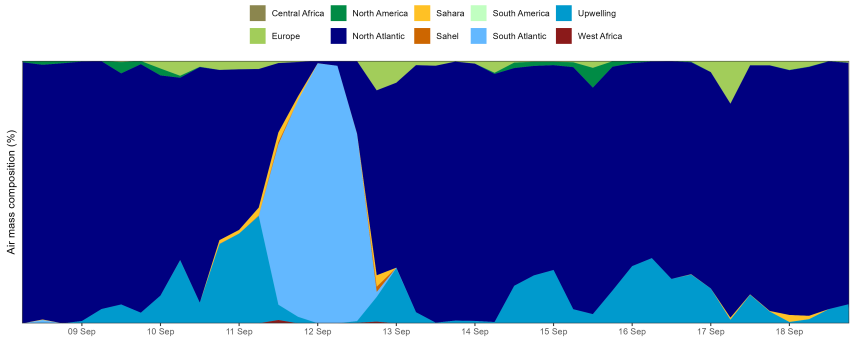

Figure 5.19: Daily air masses at the CVAO during the September 2024 measurement campaign. The map defining the regions is shown in figure 2.3

constant contamination is not affecting HONO measurements. The instrument appeared to be operating well during this period, other than issues with the gas flow described in section 5.2.3. Figure 5.8 shows that during the 12th and 13th September the measured LOPAP gas flows were between 1000 and 1200 mL min^{-1}. The HONO data presented have been processed using a constant gas flow of 1128 mL min^{-1}, the average of the gas flows measured during the campaign, which is quite close to the gas flows measured on the 12th and 13th September, therefore it is unlikely that the high HONO values are caused by incorrect gas flow values used to process the data. The HONO mixing ratios from these two days are therefore being treated as genuine, since no reason to remove them has been identified.

Baseline HONO, NO and NO_2 diurnals from the campaign are shown in figure 5.20. As with the diurnals from February 2023, a clear midday peak is seen in HONO and NO, with nighttime values returning to around zero. The peaks in the early morning in the NO_2 diurnal for the campaign are driven by spikes on the nights of 9th and 13th September.

5.3.3 Previous HONO measurements at the CVAO

HONO measurements have been made at the CVAO in November/December 2015 and during the Atmospheric Reactive Nitrogen over the remote Atlantic (ARNA) campaigns in August 2019 and February 2020 [136, 163]. Measurements during ARNA were conducted both from the CVAO and from the FAAM BAe-146-301 atmospheric research aircraft, whereas measurements from November/December 2015 were only carried out at the CVAO. Unfortunately, during the February 2020 measurement campaign, there was a problem with the fibre op-

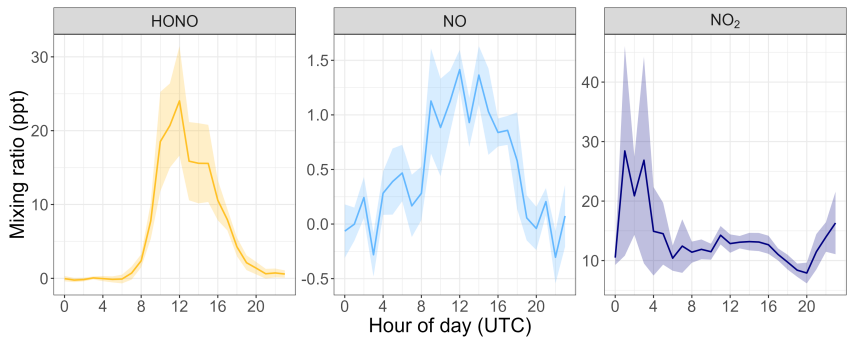

Figure 5.20: Baseline diurnal plots of HONO, NO and NO_2 during the September 2024 measurement campaign, with shaded areas representing ± standard error.

tic cable in the LOPAP's second channel and therefore the ground measurements from this campaign are not considered reliable and are not shown here.

HONO ground measurements at the CVAO

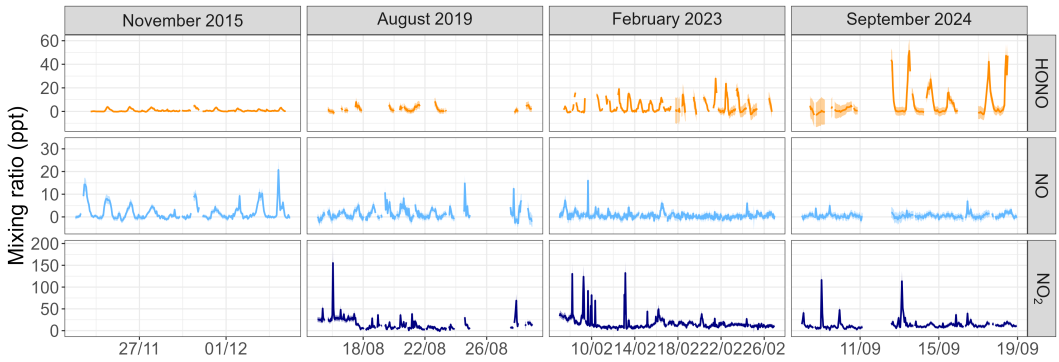

Figure 5.21: Hourly timeseries of HONO, NO and NO_2 measured during the February 2023 and September 2024 campaign and during previous campaigns at the CVAO. NO_2 data for November 2015 are not available. Shaded area represent ± measurement uncertainty.

Timeseries for HONO, NO and NO_2 during the previous HONO ground campaigns are shown in figure 5.21, alongside data from February 2023 and September 2024, filtered to remove periods when wind speed and direction indicated the site was sampling local pollution. NO_2 data from 2015 are not shown as measurements before 2017 are not considered reliable. The data gaps in HONO in August 2019 are largely due to instrumental issues, rather than local pollution, as can be seen by the fact that most of the NO_x data have not been removed.

Comparing the HONO diurnals from all campaigns (figure 5.22) highlights how much higher HONO mixing ratios were in February 2023 and in September 2024 compared to the previous campaigns. The higher mixing ratios seen in September 2024 are discussed in section 5.3.2 and the large standard error on these measurements show that there is a lot of variability associated with them. As described in section 2.2.1, higher NO_x mixing ratios are seen in autumn and winter at the CVAO. During these seasons, the air masses reaching the site have a higher European and African influence, which could help explain the difference in magnitude between HONO measurements in February and August. The measurements from August 2019 were also collected from the top of the 7.5 m tower, as opposed to from the top of a shipping container (roughly 3 m above ground level) for the other campaigns, which could lead to some differences in the mixing ratios seen.

Intercomparisons between different HONO instruments have generally agreed on HONO variability, but divergences are seen when looking at the magnitude of mixing ratios [171, 172]. During all ground-based campaigns at the CVAO, HONO was measured using a LOPAP, however two different instruments were used, one for the November 2015 and August 2019 campaigns (University of Birmingham) and another for February 2023 and September 2024 campaigns (University of York). As discussed in section 5.2.1, the LOPAP measurement technique should be free from interferences, as the use of a wet chemical sampling technique avoids heterogeneous HONO reactions and the use of a two channel system allows for signal from any interfering species to be quantified and removed. The difference in mixing ratios seen across the four campaigns could be due to instrumental problems leading either to the measurement offsets being overestimated in November 2015 and in August 2019 or being underestimated in February 2023 and September 2024. As HONO displays a diurnal cycle across all four campaigns, the interfering species would also be expected to display a diurnal cycle, as values peak at midday and are close to zero overnight. Previous studies have tested interferences from NO, NO_2, O_3, HNO_3, PAN, volatile organic compounds (VOCs) and reactions between O_3, NO_x and SO_2, and found a maximum real (after the signal from channel 2 had been subtracted from channel 1) interference of 0.06% from HNO_3, showing that the two channel system is able to effectively remove signals from interfering species [164, 167]. In February 2023 and September 2024 the average interferences were 29% and 42% of the channel 1 value, respectively, in line with previously reported values, with higher

interferences seen in September 2024 due to the local pollution event [166, 173]. The average interferences from November 2015 and August 2018 are not known, but if they were higher than seen previously, this could indicate that during these campaigns interferences were overestimated, potentially due to difference in instrument setup or concentrations of the sampling reagents. It is therefore possible that the differences seen between the campaigns are due to instrumental biases, however without any evidence of this, the measurements are treated as real.

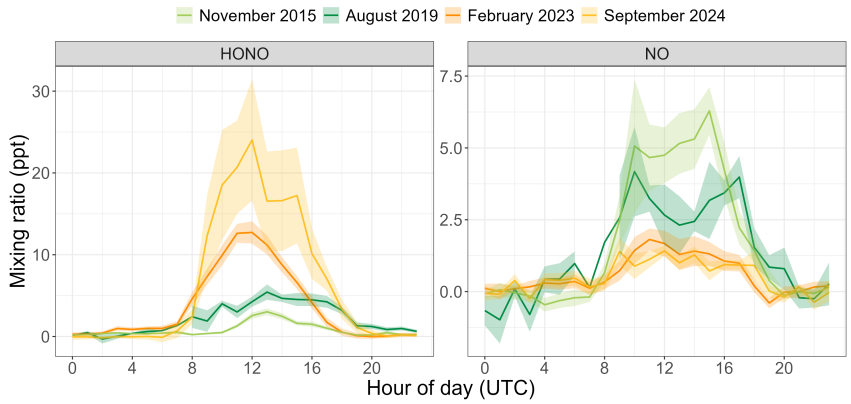

Figure 5.22: Baseline diurnal HONO and NO cycles measured at the CVAO during the different measurement campaigns that have taken place at the site.

Whilst the HONO measurements are highest in February 2023 and September 2024, the NO mixing ratios are the lowest of all the campaigns in these months, and measurements from November 2015 behave in the opposite manner, with the lowest HONO mixing ratios and the highest NO mixing ratios. The variability in the HONO/NO ratios seen across the different campaigns implies that NO levels are not a direct control for HONO mixing ratios in the remote MBL.

HONO measurements during ARNA

An overview of the ARNA summer (August 2019) and winter (February 2020) flight campaigns is given in Andersen *et al.*, with four flights taking place during the summer campaign and eight flights taking place during the winter campaign, all measuring HONO, NO, NO_2, O_3, aerosol composition and surface area and pNO_3^- over the ocean around the CVAO [136]. Figure 5.23 shows the HONO, NO and NO_2 mixing ratios measured during both ARNA flight campaigns,

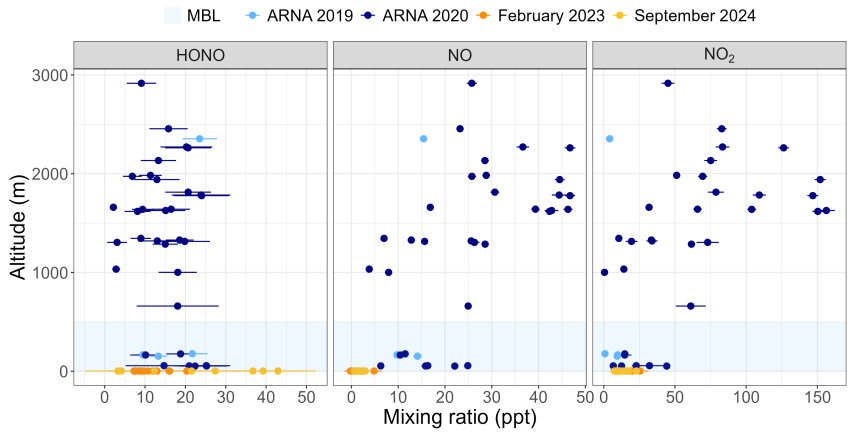

Figure 5.23: Mean HONO, NO and NO_2 mixing ratios measured during SLRs during ARNA flights and midday (11:00–15:00 UTC) daily averaged ground-based measurements from February 2023 and September 2024, coloured by measurement campaign. Error bars indicate ± measurement uncertainty and the shaded blue region indicates the MBL.

averaged over each straight-and-level run (SLR) carried out during the flights, and during the February 2023 and September 2024 ground campaigns.

Table 5.2 summarises the HONO, NO and NO_2 values measured on the ground, in the MBL (below 500 m) and above the MBL. NO and NO_2 show a clear increase as the altitude increases, whereas HONO mixing ratios remain fairly constant across its vertical profile. Both NO_2 and HONO ground measurements are similar to the measurements made on the aircraft in the MBL, whereas NO ground measurements are significantly lower than MBL aircraft measurements.

Table 5.2: Mean ± 1σ HONO, NO and NO_2 mixing ratios on the ground (only midday values used), in the MBL and above the MBL, measured during ARNA, the February 2023 and the September 2024 ground campaign.

Measurement height	HONO (ppt)	NO (ppt)	NO_2 (ppt)
Ground (Feb 2023)	11.6 ± 3.7	1.3 ± 1.2	13.2 ± 4.4
Ground (Sep 2024)	23.4 ± 15.7	1.5 ± 0.7	14.8 ± 4.6
MBL	18.2 ± 5.9	14.3 ± 5.7	16.8 ± 13.0
Above MBL	14.3 ± 6.5	28.4 ± 13.2	70.8 ± 47.5

5.3.4 Photostationary state analysis

The midday (11:00 to 15:00 UTC) HONO lifetime, τ_{HONO}, can be calculated using the known loss pathways (R 5.1-R 5.3) for HONO in the remote MBL (eq.

5.3).

$$\tau_{HONO} = \frac{1}{j_{HONO} + k_2 \times [OH] + k_{dep}} \tag{5.3}$$

Measurements of photolysis rate constants are carried out at the CVAO (described in section 5.2.5) and OH was measured during the February 2023 campaign with the average midday value from this campaign, 2×10^6 molecules cm^{-3}, used for September 2024 analysis. The reaction rate for R 5.3 was taken from Atkinson *et al.* [121] and the reaction rate for the dry deposition of HONO (R 5.2), k_{dep}, was calculated using equation 5.4.

$$\mathrm{k_{dep}} = \frac{\nu_{dep}}{H} \tag{5.4}$$

The deposition velocity, ν_{dep}, used to calculate k_{dep} was 1 cm s^{-1} [138]. The effective boundary layer height, H, used was calculated by multiplying the photolytic HONO lifetime, $\tau_{HONO\ photo} = \frac{1}{j_{HONO}}$, by the HONO Deardroff velocity (0.3 m s^{-1}) measured during SLRs at roughly 100 ft during the ARNA flights in August 2019 [136].

During the February 2023 measurement campaign, the mean midday τ_{HONO} was 13 minutes and during the September 2023 the mean midday τ_{HONO} was 11 minutes. We can therefore assume that for both campaigns the PSS was reached and use known HONO production (R 5.4) and loss (R 5.1–R 5.3) mechanisms to calculate PSS HONO mixing ratios. The measured and PSS HONO mixing ratios can be compared to determine whether there is a missing photochemical source and if including renoxification via the photolysis of pNO_3^- helps balance the HONO production and loss.

Photostationary state without photochemical HONO source

The reactions involved in the production and loss of HONO in the remote MBL are shown in the introduction (section 5.1), however, as discussed, there is still some uncertainty regarding HONO sources. During the February 2023 and September 2024 campaigns, the species involved in the production and loss of HONO were measured at the CVAO (see sections 2.2.1 and 5.2.5), with the reaction rates k_1 and k_2 taken from Atkinson *et al.* [121] and the reaction rate for the dry deposition of HONO, k_{dep}, calculated as described above (eq. 5.4).

$$\mathrm{HONO_{PSS}} = \frac{k_1 \times [OH] \times [NO]}{j_{HONO} + k_2 \times [OH] + k_{dep}} \tag{5.5}$$

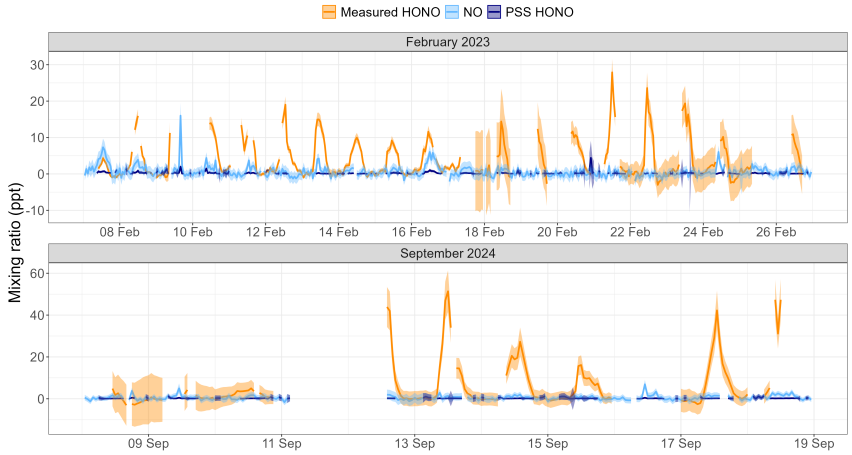

Figure 5.24: Timeseries of hourly HONO (orange), NO (light blue) and PSS HONO (dark blue), calculated using equation 5.5, during the February 2023 and September 2024 campaigns. Shaded area represents ± measurement uncertainty.

HONO PSS calculations that don't include any photochemical production (eq. 5.5), as shown in figure 5.24 (in dark blue), are not able to accurately reflect measured HONO values (in orange) during the February 2023 and the September 2024 campaigns. Even on days with higher NO mixing ratios (7th and 16th February) the reaction between NO and OH (R 5.4) is not enough to account for the measured HONO mixing ratios. This further confirms a missing photochemical source for HONO in the remote MBL.

HONO production from NO_2 uptake

Studies in polluted environments have suggested that the uptake of NO_2 onto illuminated aerosols containing TiO_2 could be an additional source of HONO [126, 130–132], with the mechanism proposed by Dupart *et al.* shown in reactions R 5.6-R 5.10 below [132].

$$\mathrm{TiO_2 + h\nu \longrightarrow e^-_{CB} + h^+_{VB}} \tag{R 5.6}$$

$$\mathrm{h^+_{VB} + H_2O \longrightarrow H^+ + OH} \tag{R 5.7}$$

$$\mathrm{e^-_{CB} + O_2 \longrightarrow O_2^-} \tag{R 5.8}$$

$$\mathrm{NO_2 + O_2^- \,(or\, e^-_{CB}) \longrightarrow NO_2^- + O_2} \tag{R 5.9}$$

$$NO_2^- + H^+ \longrightarrow HONO \quad \text{(R 5.10)}$$

In the clean atmosphere, however, this mechanism has been shown to not be a significant source of HONO [51, 136, 138, 169]. A rough calculation using equation 5.6, with an upper-limit uptake coefficient, $\gamma_{NO_2 \rightarrow HONO}$, of 10^4 (from Dyson *et al.* [130]) and an aerosol total surface area of 215 μm^2 cm^{-3} (measured at the CVAO by Jiang *et al.* [169]) was used to estimate what impact NO_2 uptake could have on HONO production at the CVAO.

$$\frac{d[HONO]}{dt} = k[NO_2] = \frac{\gamma_{NO_2 \rightarrow HONO} \times SA \times v}{4} \times [NO_2] \quad (5.6)$$

For February 2023 the maximum HONO production from NO_2 was 0.9 ppt h^{-1}, with a mean production of 0.1 ppt h^{-1}, and for September 2024 the maximum and mean production from NO_2 uptake were 0.8 and 0.09 ppt h^{-1}. Therefore, reactions R 5.6–R 5.10 do not represent a significant HONO source in this environment.

HONO production from pNO_3^- photolysis

Various studies in the remote MBL have, as discussed in the introduction (section 5.1), proposed that renoxification via the photolysis of pNO_3^- is the key source of HONO over the oceans. The updated equation for calculating the PSS HONO, including the photolysis of pNO_3^-, is shown in equation 5.7. An enhancement factor, $f = \frac{j_{pNO_3^-}}{j_{HNO_3}}$, is included to account for the enhanced photolysis of pNO_3^- compared to that of HNO_3.

$$HONO_{PSS} = \frac{k_1 \times [OH] \times [NO] + j_{HNO_3} \times f \times [pNO_3^-]}{j_{HONO} + k_2 \times [OH] + k_{dep}} \quad (5.7)$$

While many studies agree that renoxification is an important HONO source in the remote MBL, the factors affecting the value of f are still not fully understood, with a wide range of values for f being proposed based on both field measurements and laboratory studies. In recent work by Andersen *et al.* and Rowlinson *et al.* (*in prep*), the relationship between the enhanced photolysis of pNO_3^- and the concentration of pNO_3^- has been captured in new parameterisations for f, based on the Langmuir adsorption isotherm [136].

$$f_{Andersen} = \frac{385.7}{1 + 0.19 \times [pNO_3^-]} \quad (5.8)$$

$$f_{Rowlinson} = \frac{5.02 \times 10^8}{1 + 7.19 \times 10^5 \times [pNO_3^-]} \tag{5.9}$$

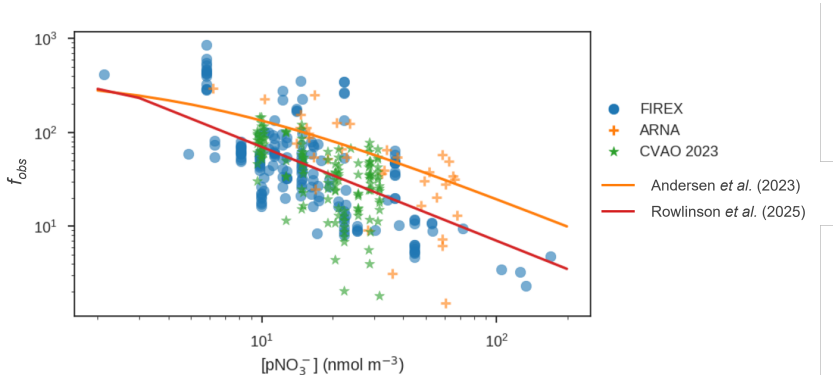

Figure 5.25: The Langmuir fit used to derive the Andersen and Rowlinson parametrisations. The Andsersen parametrisation was developed using data from ARNA (in orange), the Rowlinson parametrisation was developed using all plotted data. Plot by Dr Matthew Rowlinson.

These parameterisations were developed by plotting f_{obs} (eq. 5.10, with P_{HONO} representing HONO production without nitrate and L_{HONO} representing HONO loss mechanisms), which determines the enhancement needed to account for the missing HONO production, against measured pNO_3^- (in nmol m^{-3}) and finding the Langmuir fit (figure 5.25).

$$f_{obs} = \frac{P_{HONO} - L_{HONO}}{j_{HNO_3} \times [pNO_3^-]} \tag{5.10}$$

The Andersen parameterisation was developed using values from the ARNA flight campaigns (section 5.3.3) [136], whereas the Rowlinson parameterisation used, as well as the ARNA data, data from the Fire Influence on Regional to Global Environments and Air Quality (FIREX-AQ) campaign [174] and data from the February 2023 HONO measurements at the CVAO (shown in section 5.3.1).

Figure 5.26 shows the measured and parametrised HONO timeseries from both campaigns. Errors associated with the parametrised PSS HONO values have been estimated based on the error associated with measured HONO in each campaign, as there is no uncertainty associated with the parametrised enhancement factor.

It is clear that including the photolysis of pNO_3^- in the PSS results in a much better prediction of measured HONO values compared to using the PSS without

including pNO_3^- photolysis (figure 5.24), across both campaigns and parametrisations used. Both $f_{Andersen}$ and $f_{Rowlinson}$ do a better job estimating the HONO mixing ratios from February 2023 than those from September 2024. HONO mixing ratios in September 2024 exhibited much more variability compared to those in February 2023, as discussed in section 5.3.2, with some uncertainty surrounding the extremely high values seen on the 12th and 13th September. On days in September 2024 when HONO values were lower (10th, 14th and 15th September), similar to values seen in February 2023, both parametrisations do a good job of predicting the mixing ratios seen.

Table 5.3: Normalised mean biases (NMB) for the Andersen and Rowlinson parametrisations during the February 2023 and September 2024 campaigns, calculated from midday values (between 11:00 and 15:00 UTC).

Campaign	Andersen parametrisation	Rowlinson parametrisation
February 2023	27%	-37%
September 2024	-21%	-63%

Table 5.3 summarises the normalised mean bias (NMB) for both parametrisations from both campaigns, when looking at midday values (between 11:00 and 15:00 UTC). In both cases, the Andersen parametrisation does a better job at estimating measured HONO values, despite the fact that the Rowlinson parametrisation was developed using data from the February 2023 campaign. The Rowlinson parametrisation, however, used a more global dataset which spanned a

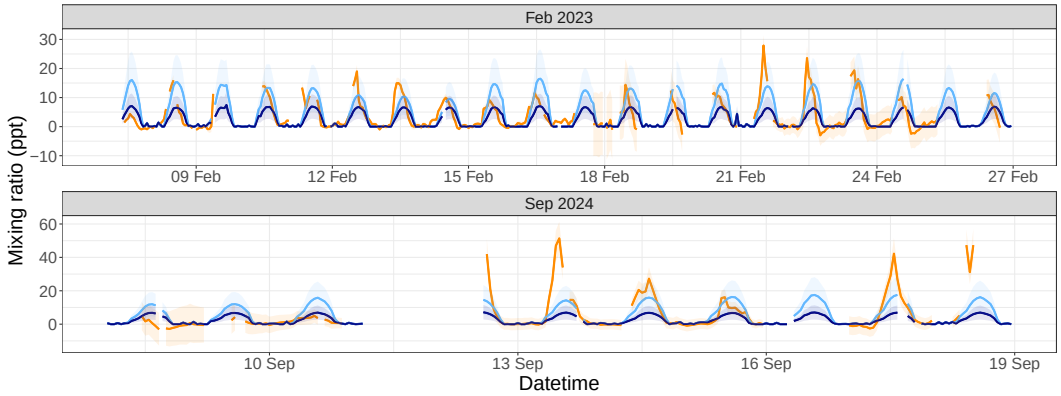

Figure 5.26: Measured HONO and PSS HONO calculated using $f_{Andersen}$ and $f_{Rowlinson}$ from the February 2023 and September 2024 campaigns. Uncertainties associated with measurements are represented by the shaded areas.

broader range of pNO_3^- and f_{obs}, which are therefore not as representative of the conditions in the tropical North Atlantic, whereas the Andersen parametrisation was developed using only data collected at the CVAO.

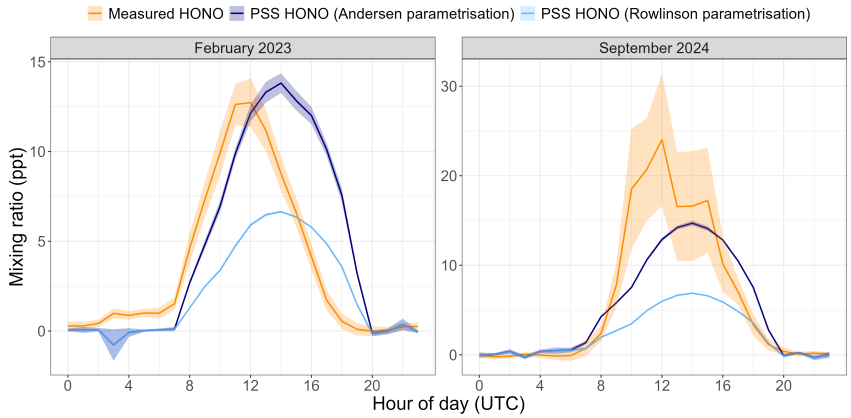

Figure 5.27: Diurnal cycle of measured HONO and PSS HONO calculated using $f_{Andersen}$ and $f_{Rowlinson}$. Shaded areas represent ± standard error.

While the Andersen parameterisation does a slightly better job at reproducing the measured HONO values, both parameterisations predict the midday maximum (figure 5.27), showing that including production due to renoxification accounts for the key photochemical source of HONO in the remote MBL. However, during both campaigns the parametrised diurnal is broader than the measured diurnal, which is likely a result of how both $f_{Andersen}$ and $f_{Rowlinson}$ have been calculated and used to determine the PSS HONO mixing ratio. Since aerosol filter samples were changed once a day and the parametrisations are only dependent on pNO_3^-, one f value is used for the whole day, calculated as the average enhancement between 11:00 and 15:00 UTC. In doing so, the enhancement of $j_{pNO_3^-}$ compared to j_{HNO_3} is considered constant over the whole day.

Figure 5.28 shows how f_{obs} varied throughout the day during both campaigns, with a greater enhancement seen in the morning, around 09:00-10:00 UTC. As mentioned above, pNO_3^- measurements from the CVAO are not available with an hourly time resolution, however modelled pNO_3^- diurnal profiles show that pNO_3^- concentrations decrease during the day, when the photolysis of pNO_3^- is included in the model, as pNO_3^- is being used up by its photolysis. An inverse relationship between pNO_3^- concentrations and f_{obs} has been seen in a number of studies, due to the relationship between bulk nitrate and surface-bound nitrate, with the photolysis of the latter being enhanced (see section 5.1). Throughout

the day, as surface-bound pNO_3^- is being photolysed, the enhancement will decrease. Previous studies have also seen a red shift in the absorption spectra of surface-adsorbed HNO_3 compared to gaseous HNO_3, and the effect this shift in the absorption spectrum of surface-adsorbed and particulate nitrate has in the atmosphere is not yet fully understood [143, 144, 148]. An increase in pNO_3^- photolysis could perhaps be seen at dawn and dusk, when the sunlight spectrum is more red-shifted, however the shape of the f_{obs} diurnal points only to a maximum at dawn, rather than at dawn and dusk. A lack of maxima at dusk could be due to low availability of surface-bound pNO_3^-, as it has been photolysed during the day, as shown by the modelled pNO_3^- diurnal.

It is clear from the differences between measured and PSS values, that the inclusion of $f_{parametrised}$ is not enough to fully capture all the factors that are affecting the pNO_3^- photolysis to yield HONO. Previous studies have found that the enhanced photolysis of pNO_3^- compared to HNO_3 is affected by other factors that have not been captured by the parameterisations, and the following section discusses what effects these factors are seen to have on HONO measurements from the CVAO.

5.3.5 Other factors affecting enhancement factors

The two parameterisations discussed in section 5.3.4 (eq. 5.8 and 5.9) only account for the fact that the enhancement of pNO_3^- compared to HNO_3 photolysis is greater at lower pNO_3^- concentrations, due to the increased photolysis rate seen with surface-bound nitrate compared to bulk nitrate (see section 5.1). Studies have shown that other factors also affect f, specifically the relative humidity (RH,

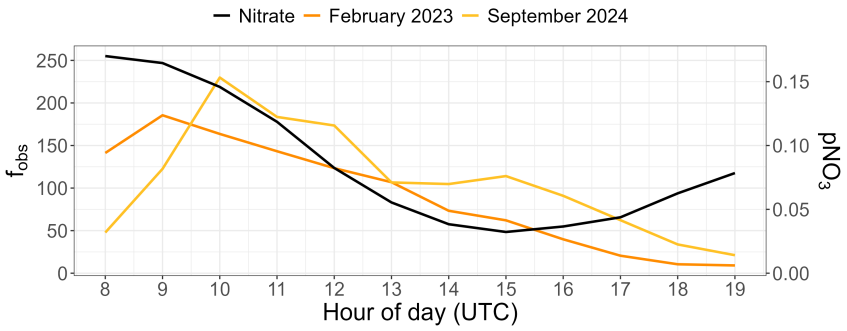

Figure 5.28: Daytime diurnal cycle (between 08:00 and 19:00 UTC) of f_{obs} (calculated with eq. 5.10) during the February 2023 (orange) and September 2024 (yellow) campaigns, and of pNO_3^- modelled for February 2023 (black).

%), the physicochemical properties and the composition of the aerosol particles [136, 137, 146, 153].

The ratio between the observed (eq. 5.10) and parametrised (eq. 5.8 and 5.9) enhancement factors, $\frac{f_{obs}}{f_{parametrised}}$, can be used to determine whether the enhancement of pNO_3^- is influenced by any of these factors. An f ratio of 1 would indicate that the parametrisation accurately calculates the enhancement factor, an f ratio greater than 1 points to an underestimation, likely meaning that other enhancing factors have not been accounted for, and an f ratio less than 1 points to an overestimation, indicating that factors that could be impeding the photolysis have not been properly considered.

The effect of RH on f

The effect of relative humidity (RH) on the enhancement of $j_{pNO_3^-}$ compared to j_{HNO_3} has mainly been examined in lab studies, as it is easy to conduct measurements across a wide range of RH and the effect of RH can be studied on artificial particles, without needing to account for potential enhancements being due to aerosol composition. A large number of studies have seen an increase in the production of HONO (or NO_2) from irradiated particles at higher RH [146, 147, 150, 151, 153]. Specifically, Jin *et al.* and Li *et al.* saw a marked increase in HONO (or NO_2) production above the deliquescence point of the particles they were studying [150, 151]. Above the deliquescence point (for sea salt aerosol this

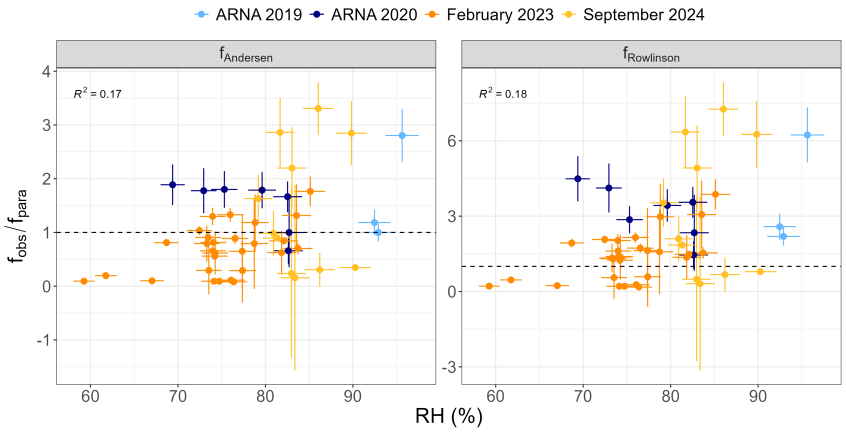

Figure 5.29: $f_{obs}/f_{parametrised}$ (using both $f_{Andersen}$ and $f_{Rowlinson}$) plotted against RH, coloured by the campaign during which the measurements were made. Dashed line indicates a ratio of 1. For the ARNA data, only measurements collected in the MBL have been used.

is roughly RH > 75%) aerosols are present as suspended droplets and products from the photolysis of pNO_3^- can diffuse out of the particle, leading to much higher yields that those seen with dry particles, where this cannot occur.

Andersen *et al.* were able to see this effect with the ARNA flight campaign field measurement, with lower f_{obs} seen in samples collected above the MBL (> 500 m) where the RH is much lower than at the surface [136].

Measurements made during the ground campaigns (figure 5.29, in orange and yellow) did not span a wide range of RH, however the f ratio does show an increase as RH increases, particularly when comparing the measurements made at around 60% RH with measurements made above 70%. The RH during the September 2024 campaign was higher than during the February 2023 campaign, which could perhaps explain why HONO mixing ratios were higher during this campaign. The broad range of f ratios seen at all RH however highlights that more factors are affecting the enhancement of pNO_3^- photolysis.

The effect of aerosol composition on f

As shown in figure 5.30, neither the $f_{Andersen}$ nor the $f_{Rowlinson}$ ratio show a clear correlation with any of the other aerosol components measured during the ARNA campaigns (only measurements collected in the MBL are shown here) or during the February 2023 and September 2024 ground campaigns. During the February 2023 and September 2024 ground campaigns, measurements of fluoride and methanesulfonic acid (MSA) were also collected, however they are not shown in figure 5.30 as they remained 0 and 0.01 μg m^{-3}, respectively, throughout the whole campaign.

A lack of correlation with nitrate is expected, as $f_{parametrised}$ already accounts for the relationship between f_{obs} and pNO_3^-, however as mentioned in section 5.1, previous lab studies have seen relationships between f and aerosol compositions, which were not seen in these data.

Both cations and halide anions have been shown to increase the surface affinity of pNO_3^-, which, as discussed above, is thought to be more photolytically active compared to bulk nitrate [140, 153, 154, 161]. Higher concentrations of halides and cations would therefore be expected to result in an increase in f, however no clear trend is visible for either of these species. This could be due to a limited number of measurements and a small range of values seen during the campaign.

Oxalate was only measured during the ground campaigns and again it does

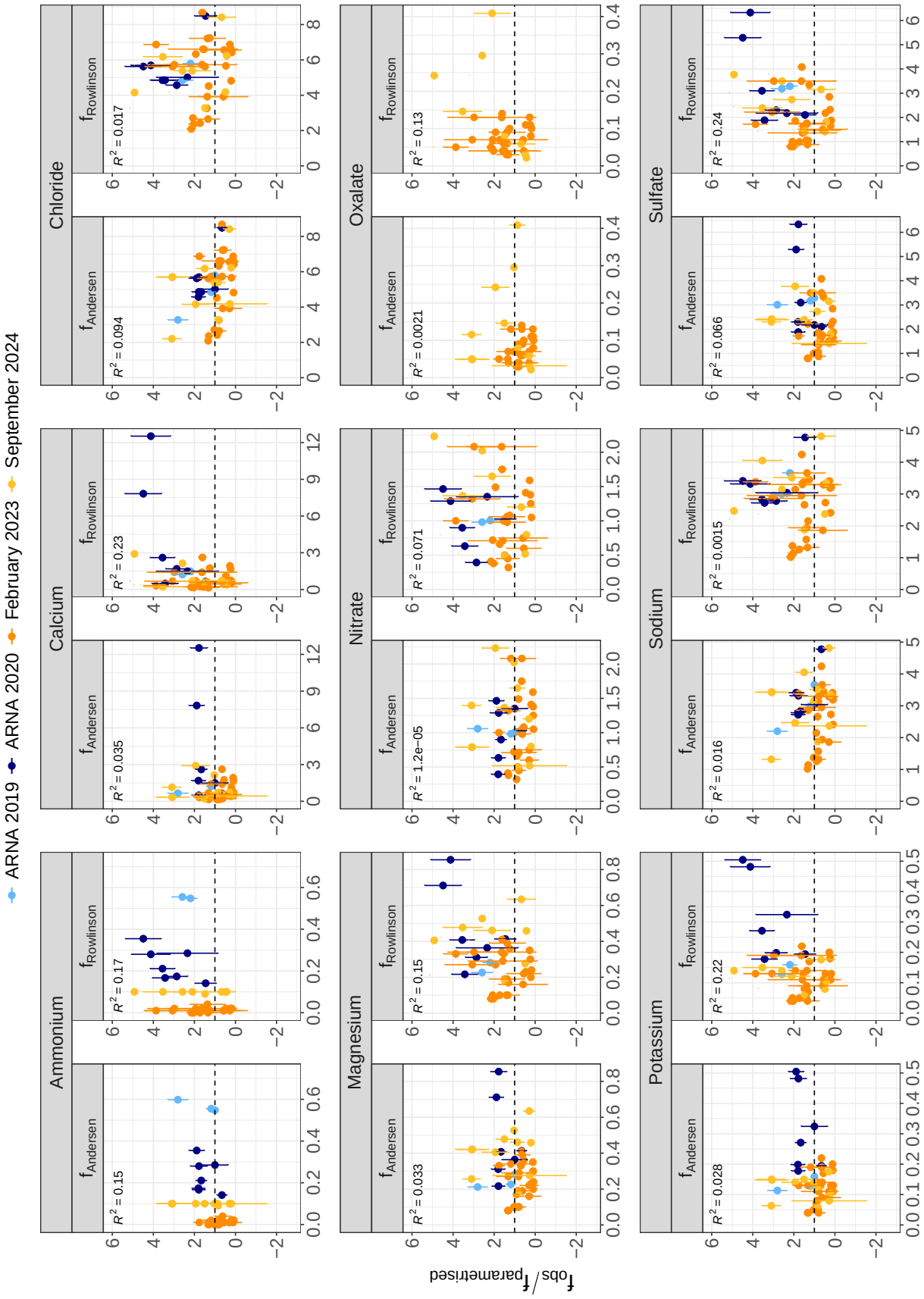

Figure 5.30: $f_{obs}/f_{parametrised}$ (using $f_{Andersen}$ and $f_{Rowlinson}$) plotted against the measured aerosol composition, coloured by campaign (only measurements made in the MBL from ARNA are included). Oxalate was not measured during ARNA. Dashed line indicates a ratio of 1.

not show any trend with changing f ratio. Li *et al.* saw an increase in HONO production from samples containing oxalic acid (OA) compared to pure $NaNO_3^-$ samples, attributed to OA acting as an OH scavenger and a source of protons for NO_2^- [151]. This study was conducted using sample films, rather than particles, as was done by Sommariva *et al.* who instead saw that adding oxalate to particles containing nitrate suppressed the photolysis of pNO_3^-, though thought this could simply be due to the oxalate coating on the particles covering the nitrate [153].

The effect of aerosol pH on f

pH has been shown to affect the enhancement of NO_3^- photolysis in lab based studies, where experiments can be carried out with a wide range of pH values [139, 140, 147, 148, 150, 152]. The photolysis of pNO_3^- can yield NO_2 and O^- (R 5.11) or NO_2^- and $O(^3P)$ and HONO can then be produced through the protonation of NO_2^- (R 5.12), with this process enhanced when the pH is lower than the pK_a of HONO (pH < 3.2) [139, 140, 152].

$$NO_3^- + h\nu \longrightarrow NO_2 + OH \qquad \text{(R 5.11)}$$

$$NO_3^- + h\nu \longrightarrow NO_2^- + O(^3P) \xrightarrow{H^+} HONO \qquad \text{(R 5.12)}$$

Aerosol pH was only measured during the February 2023 campaign and did not span a wide range of values, between 5 and 6 (figure 5.31). A small decrease

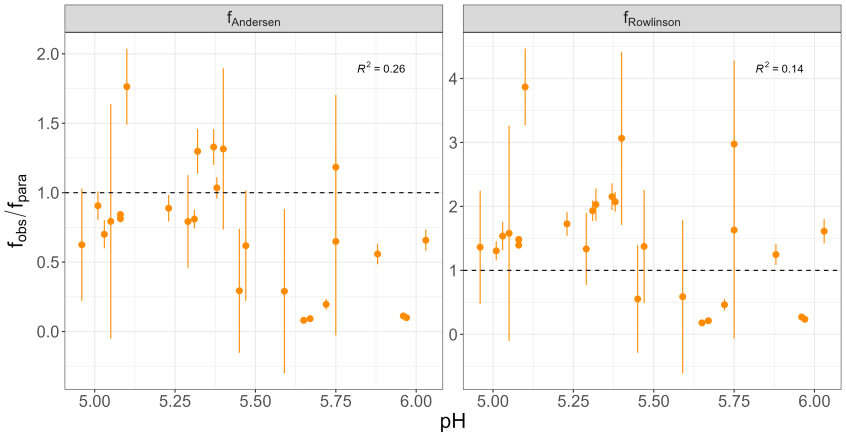

Figure 5.31: $f_{obs}/f_{parametrised}$ (using both $f_{Andersen}$ and $f_{Rowlinson}$) plotted against the aerosol pH, which is only available for the February 2023 measurement campaign. Dashed line indicates a ratio of 1.

in the f ratio is however still seen at higher pH, which is more pronounced with $f_{obs}/f_{Andersen}$ than with $f_{obs}/f_{Rowlinson}$, indicating that under more basic conditions the parametrisations could be overestimating f.

5.3.6 HONO production from NO_x

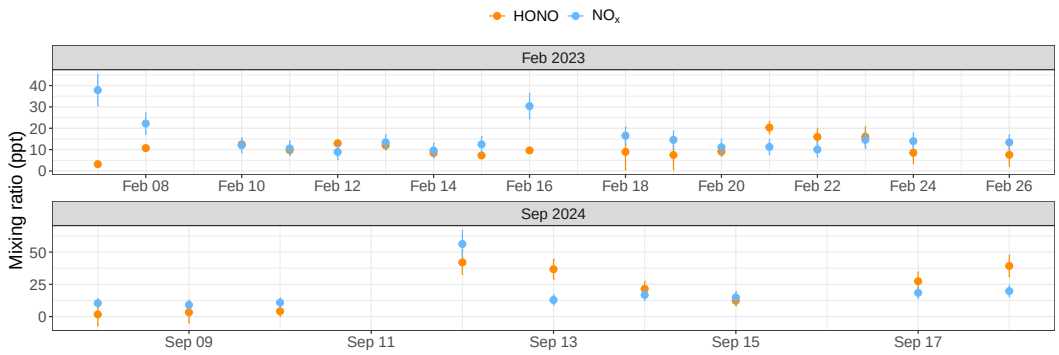

Figure 5.32: Midday (between 11:00 and 15:00 UTC) mixing ratios of HONO and NO_x during the February 2023 and September 2024 campaigns

As discussed in section 5.3.4, the photolysis of pNO_3^- is generally able to account for the missing source of HONO production (fig 5.26). However, the similar abundances of HONO and NO_x seen during both the February 2023 and the September 2024 campaigns (shown in figure 5.32) are unexpected based on the differing lifetimes of HONO and NO_x in the tropical MBL. The main loss pathway for HONO is its photolysis, which produces NO and OH (R 5.1), and around midday occurs on the timescale of $\sim$ 10 minutes (see section 5.3.4). On the other hand, the main loss pathway for NO_x, the reaction between OH and NO_2 to produce HNO_3, occurs on much longer timescales (roughly 6 to 12

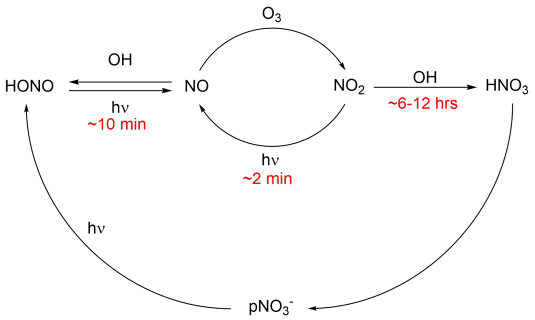

Figure 5.33: A broad summary of the reactive cycling that occurs in the tropical MBL, with the rough lifetime associated with each step in red.

hours in the tropical MBL). As discussed in chapter 1, HNO_3 is then removed through wet and dry deposition and is able to re-enter the reactive nitrogen cycle through the photolysis of pNO_3^-. Based on these lifetimes, the HONO produced from the photolysis of pNO_3^- would be expected to rapidly convert into NO_x, which will then slowly convert into HNO_3, which can then be taken up onto aerosols as pNO_3^- and produce HONO and NO_2 (summarised in figure 5.33).

Table 5.4: Mean midday (11:00-15:00 UTC) HONO production and loss during February 2023 and September 2024 from the reactions investigated in this study.N.B. Loss mechanisms are negative

HONO production/loss mechanisms	Feb 2023	Sep 2024
HONO photolysis	- 47 ppt h^{-1}	- 82 ppt h^{-1}
HONO deposition	- 1.6 ppt h^{-1}	- 2.7 ppt h^{-1}
NO + OH $\rightarrow$ HONO	0.7 ppt h^{-1}	0.8 ppt h^{-1}
NO_2 uptake	0.2 ppt h^{-1}	0.4 ppt h^{-1}
pNO_3^- photolysis (without f)	0.7 ppt h^{-1}	1 ppt h^{-1}
pNO_3^- photolysis ($f_{Andersen}$)	60 ppt h^{-1}	77 ppt h^{-1}
pNO_3^- photolysis ($f_{Rowlinson}$)	29 ppt h^{-1}	35 ppt h^{-1}

The fact that during the February 2023 and September 2024 campaigns HONO and NO_x have similar mixing ratios, could indicate that a fast mechanism (or mechanisms) able to convert NO_x into HONO is occurring. The HONO production and loss rates are summarised in table 5.4 and demonstrate that in this study the main source of HONO is the photolysis of pNO_3^-, with the reaction between OH and NO (R 5.4) and the heterogeneous uptake of NO_2, two mechanisms that convert NO_x into HONO, yielding less than 1 ppt h^{-1}. These mechanisms are therefore not enough to account for the similar HONO and NO_x mixing ratios, however other reactions leading to the production of HONO from NO_x have been reported and future work will investigate the importance of these reactions in the remote MBL [175–178].

5.4 Conclusion

Two new sets of HONO measurements have been collected at the CVAO, in February 2023 and September 2024. HONO mixing ratios measured during these two campaigns were higher than ground-based mixing ratios seen during

previous campaigns at the CVAO, in November 2015 and August 2019, but similar to mixing ratios measured in the MBL over the CVAO during the ARNA campaigns in August 2019 and February 2020. The difference in mixing ratios between the ground-based campaigns could be due to the seasonality of air masses reaching the CVAO, differences in sampling heights or instrumental biases, however as there is no evidence of potential biases, the measurements are treated as real. All ground-based campaigns show a clear diurnal cycle, with a midday maximum returning to zero overnight.

This diurnal cycle could be reproduced with PSS analysis only when the production of HONO from the photolysis of pNO_3^- was included, with the enhancement of pNO_3^- photolysis compared to gas-phase HNO_3 photolysis calculated using two parametrisations, $f_{Andersen}$ and $f_{Rowlinson}$. The parametrised PSS was not able to accurately replicate the magnitude of HONO mixing ratios seen, with $f_{Andersen}$ overestimating February 2023 mixing ratios and underestimating September 2024 mixing ratios and $f_{Rowlinson}$ underestimating values from both campaigns. The parametrisations also struggled to capture the day-to-day variation in HONO mixing ratios, likely because other factors are also affecting the enhancement factor f. Discrepancies between the shape of the diurnal, with PSS diurnals broader than measured diurnals, also point to missing factors that affect the size of the enhancement at different hours of the day, potentially caused by pNO_3^- depletion throughout the day and a red-shifted absorption spectrum for pNO_3^- compared to gaseous HNO_3.

Previous studies have found relationships between f and aerosol physicochemical properties, particularly increased enhancements at high RH, at low pH and in the presence of cations and halide anions. In this work, the ratio between the observed and parametrised f is used to determine if the parametrisations are over- or underestimating the enhancement under different conditions. A slight dependence on RH and on aerosol pH is seen in these data, with both parametrisations underestimating f at the highest RH, and with a decrease in f ratio as the aerosol pH increased, particularly with $f_{Andersen}$. No further trends were seen with any of the other aerosol ions measured during the two ground campaigns. Compared to lab studies, where it is possible to conduct experiments at specific RH, aerosol composition and pH, field measurement are measuring many different potentially competing factors at once, and extracting the key factors that affect f is complicated are requires more measurements of HONO in this environment.

Future work will also focus on understanding the role pNO_3^- photolysis plays in the reactive nitrogen cycle, with the similar NO_x and HONO mixing ratios measured during the February 2023 and the September 2024 campaigns potentially indicating an unaccounted for pathway able to convert NO_x into HONO.

Chapter 6

Conclusion

The Cabo Verde Atmospheric Observatory (CVAO, 16° 51' 49" N, 24° 52' 02" W), in the tropical North Atlantic Ocean, and the Kennaook/Cape Grim Baseline Air Pollution Station (KCG BAPS, 40° 41' 00" S, 144° 41' 22" E) on the north-western tip of Tasmania in the Southern Ocean, are unique World Meteorological Organization-Global Atmospheric Watch (WMO-GAW) sites where long-term NO_x measurements have been collected using an Air Quality Design (AQD) chemiluminescence instrument, capable of measuring the low NO_x mixing ratios that are seen over the ocean. These two sites, and the NO_x instrumentation and data processing used there, have been presented in chapters 2 and 3. Chapter 2 presents the CVAO and the NO_x measurements collected there, specifically focusing on the improvements made to the NO_x processing code used at the CVAO. More streamlined processes and better data filtering routines have been implemented, leading to the easy removal of measurement cycles where large spikes are seen, due to instrumental error, without affecting normal measurements. These improvements have resulted in the identification of a baseline shift in NO_2 as being caused by instrumental issues rather than by changes in mixing ratios over the ocean and has avoided NO_2 trends being misinterpreted. The outlier treatment has also improved the data processing and will lead to a more accurate examination of the causes behind spikes seen in the data, which cannot be attributed to instrumental issues. An increase in measurement uncertainty between 2021 and 2024 has been attributed to an increase in the instrument's limit of detection (LOD) due to photomultiplier tube (PMT) temperature issues. The CVAO NO_x instrument has been running continuously since October 2006 and has been able to operate with such low LODs thanks in part to its Peltier

coolers, which have kept the PMTs at a stable temperature around $-30°C$, thus minimising dark counts and maximising sensitivity. Due to recent temperature issues, the instrument could be improved by updating this cooling system so that colder temperatures can once again be reached and maintained. Another planned instrumental update is to set up the second channel (which is currently not operational) to continually measure NO, which will provide the opportunity to better understand the reason for the spikes seen in the measurement and provide validation for measurements from the first channel. The opportunity to perform an intercomparison between NO_x measured at the CVAO using the AQD chemiluminescence instrument and using an NO laser-induced fluorescence (LIF) instrument would further validate these measurements and would confirm that NO_x offset corrections are being correctly applied, as well as revealing what details are being missed by the higher LOD seen with the chemiluminescence technique compared to the LIF technique.

The first ever comparison between two measurements of NO_x over the remote ocean conducted with the same instrument in two different hemispheres is presented in chapter 3, between the CVAO and Kennaook/Cape Grim Baseline Air Pollution Station (KCG BAPS) NO_x measurements. The comparison revealed that the data processing routines at the two sites followed the same principles and yielded very similar results, thus validating these processes. It also revealed the challenges faced when measuring NO_x at such low mixing ratios and the difficulties of quantifying measurement offsets, particularly at the KCG BAPS where both clean baseline air and polluted air from the Australian mainland is sampled, with baseline air only being measured $\sim 30\%$ of the time. The treatment of measurement offsets is of particular importance for these sites, as even a small unaccounted for offset could represent a large percentage of the total measurement when working at such low mixing ratios. The use of a new offset determination method for NO_2 has been presented, based on the assumption that when using a 30 day rolling window the lowest point represents a period when NO_2 is zero at the site and can therefore be taken as the measurement offset and used to correct NO_2 photolytic and thermal interferences, which cannot be detected using NO_x-free air. A suitable offset determination method is yet to be found for NO measurements at the KCG BAPS, given the interfering role NO_x emissions from the soil may be playing on measurements at this site.

The measurements presented in chapters 4 and 5 were both collected at the CVAO and both explore different potential sources of NO_x in the remote

marine boundary layer (MBL). In chapter 4, NO_x mixing ratios at the CVAO are examined and trends between 2012 and 2024 reveal that a key driver for the amount of NO_x detected at the CVAO are the changes in air mass composition, with noticeably higher NO mixing ratios in years when African and European air masses were more significant. Interannual variability within each air mass did not reveal as clear a set of patterns, though decreases were observed in NO_x in European and North Atlantic air masses in 2020, potentially due to the COVID-19 pandemic. NO_2 photostationary state (PSS) analysis using measured (NO_x, O_3, photolysis rates), historical (IO and BrO) and box modelled (HO_2 and RO_2, with measured values for February 2023) values revealed the same PSS underestimation that has been reported previously, thought to be due to a missing oxidant converting NO to NO_2 [19, 68, 87]. Analysis performed using measured HO_2 and RO_2 suggested that peroxy radicals do not appear to be the source of this missing oxidant, though a better understanding of the role unclassical mechanisms and the limitations of the fluorescence assay by gas expansion (FAGE) measurement technique in terms of not measuring all RO_2 is required. Plans to measure halogen oxides at the CVAO in January 2026 will provide an up to date value for these species which may help reconcile measured and PSS NO_2. Problems with current and historical NO_x measurements also need to be considered, with further analysis revealing a decrease in NO mixing ratios which lead to a decrease in $NO_{2\ PSS}$ between 2017 and 2024, though there were no obvious cause within instrumental and data processing changes that occurred in this period. As NO values approach the instrument's LOD, it becomes increasingly difficult to conclusively perform this analysis, once again highlighting how challenging measuring in these remote environments is.

The new HONO mixing ratios collected in February 2023 and in September 2024, presented in chapter 5, are higher than previous ground-based HONO measurements (November/December 2015 and August 2019) but similar to to mixing ratios measured during the Atmospheric Reactive Nitrogen over the remote Atlantic (ARNA) flight campaigns in August 2019 and February 2020. These discrepancies could be caused by seasonality or different instrumental conditions across the campaigns, though no evidence was found for any instrumental bias and previous studies have shown that HONO measurements using a Long Path Absorption Photometer (LOPAP) have a maximum interference of 0.006%. Using measured values of NO, OH and photolysis rates (j_{HONO} and j_{HNO_3}), $HONO_{PSS}$ was calculated and demonstrated to be unable to reproduce measured

values without the inclusion of pNO_3^- photolysis. The enhanced photolysis rate of pNO_3^- compared to HNO_3 was parametrised using enhancement factors from both Andersen *et al.* and Rowlinson *et al.* (*in prep*) [136]. These parametrisations broadly captured the HONO diurnal cycle, but the Andersen parametrisation overestimated February 2023 values and both parametrisations underestimated September 2024 values, with the Rowlinson parametrisation also underestimating February 2023 mixing ratios. The PSS diurnal cycle was also broader than the observed cycle, which may be caused by differences in pNO_3^- concentrations throughout the day or by differences between the HNO_3 and pNO_3^- absorption spectrum. There were no obvious relationships between the enhancement factors and relative humidity or aerosol properties, though these have been reported in lab studies [137, 140, 146–148, 150–153, 159, 161, 179]. The range of values measured during a field campaign are dependent on the conditions, and real world experiments are significantly more complicated than those created in a lab setting, therefore the lack of clear evidence for any driving or impeding factors does not imply these factors don't exist. More measurements of HONO in the MBL are needed to understand what the key drivers are. Further work also needs to be conducted to understand if there are any missing mechanisms that convert NO_x into HONO and could therefore explain the similar mixing ratios between these two species, as based on their lifetimes HONO mixing ratios would be expected to be lower than NO_x mixing ratios.

Appendix A

Calculated photolysis rates

When spectral radiometer data is unavailable, monthly correlations of photolysis rates with solar radiation for each hour between 09:00 and 17:00 are used to calculate the photolysis rates. The plots below show this for j_{HONO} and j_{HNO_3} from September 2024.

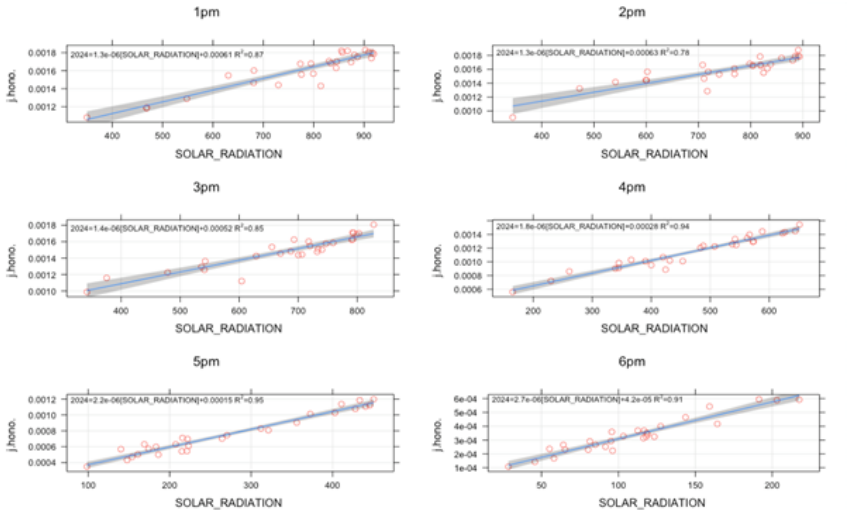

Figure A.1: Correlation of j_{HONO} and solar radiation between 13:00 and 18:00 for September.

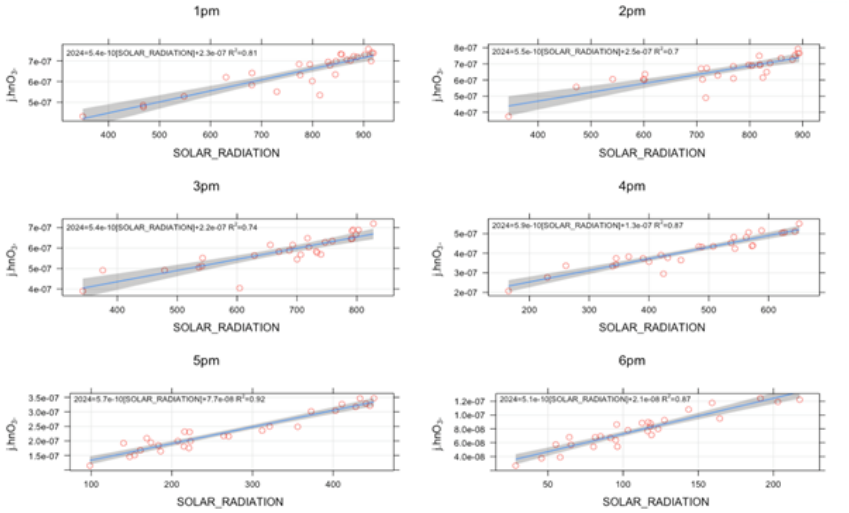

Figure A.2: Correlation of j_{HNO_3} and solar radiation between 13:00 and 18:00 for September.

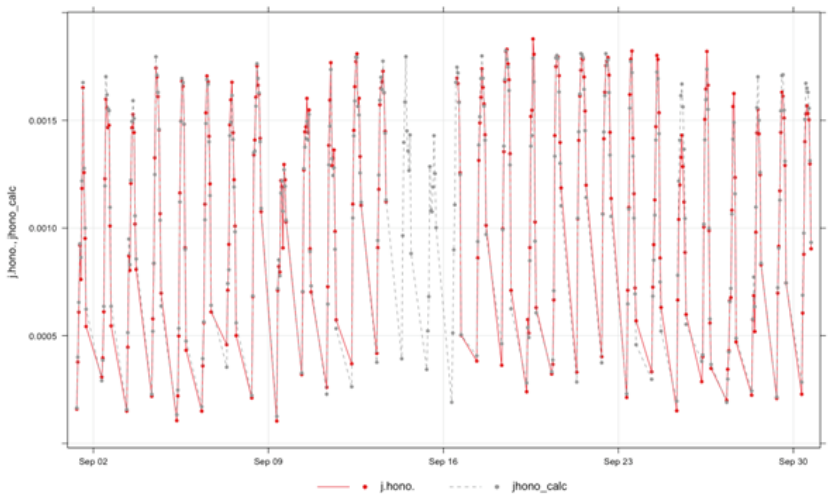

Figure A.3: Timeseries of measured and calculated j_{HONO} values for September 2024.

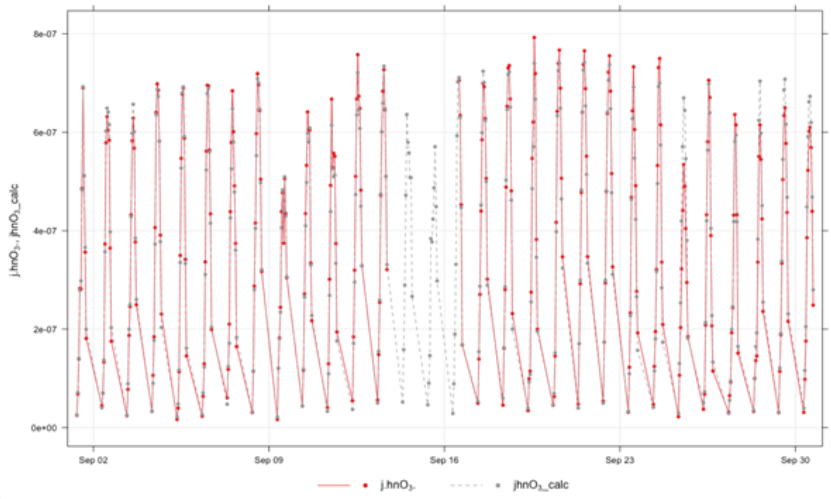

Figure A.4: Timeseries of measured and calculated j_{HNO_3} values for September 2024.

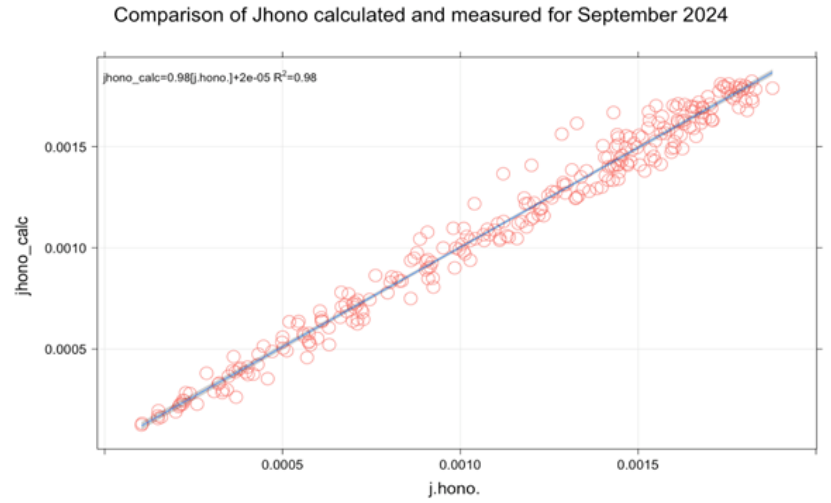

Figure A.5: Comparison of measured and calculated j_{HONO} values for September 2024. The error for calculated j_{HONO} is determined from the error on the slope (2% in this case).

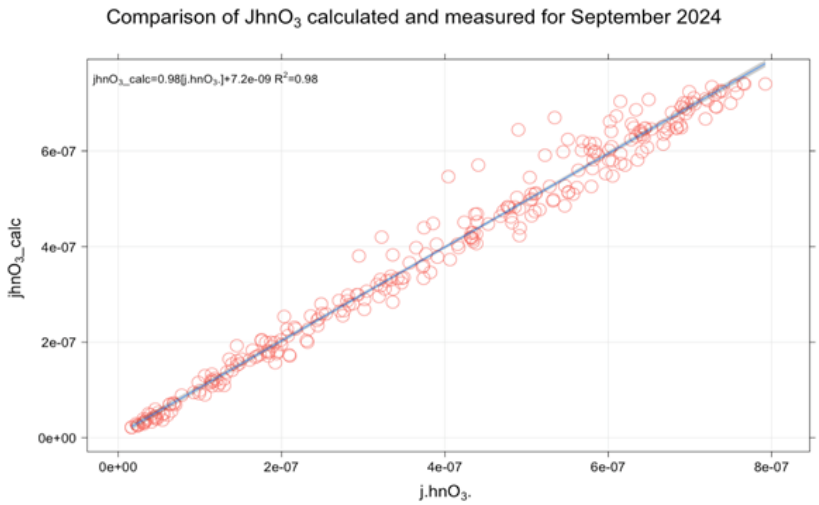

Figure A.6: Comparison of measured and calculated j_{HNO_3} values for September 2024. The error for calculated j_{HNO_3} is determined from the error on the slope (2% in this case).

Appendix B

Reaction mechanisms added to the MCM

Table B.1: Photolysis rates of halogens added to the MCM.

Photolysis	Reference
$BrO + h\nu \longrightarrow Br + O$	Atkinson *et al.* [121]
$HOBr + h\nu \longrightarrow Br + OH$	Atkinson *et al.* [121]
$BrONO_2 + h\nu \longrightarrow BrO + NO_2$	Atkinson *et al.* [121]
$BrONO_2 + h\nu \longrightarrow Br + NO_3$	Atkinson *et al.* [121]
$BrNO_2 + h\nu \longrightarrow Br + NO_2$	Atkinson *et al.* [121]
$HOI + h\nu \longrightarrow I + OH$	Atkinson *et al.* [121]
$IO + h\nu \longrightarrow I + O$	Atkinson *et al.* [121]
$OIO + h\nu \longrightarrow I + O_2$	Atkinson *et al.* [121]

Table B.2: Halogen thermal decomposition reaction mechanisms added to the MCM.

Reaction	Reaction rate (s^{-1})	Reference
$BrONO_2 + \Delta \longrightarrow BrO + NO_2$	$2.8 \times 10^{13} \times \exp(-12360/T)$	Orlando and Tyndall [180]

Table B.3: Halogen bimolecular reaction mechanisms added to the MCM.

Reaction	Reaction rate (cm^{-3} $molecule^{-1}$ s^{-1})	Reference
$Br + O_3 \longrightarrow BrO + O_2$	$1.6 \times 10^{-11} \times \exp(-780/T)$	Burkholder *et al.* [181]
$BrO + HO_2 \longrightarrow HOBr + O_2$	$4.5 \times 10^{-12} \times \exp(460/T)$	Burkholder *et al.* [181]
$Br + HO_2 \longrightarrow HBr + O_2$	$4.8 \times 10^{-12} \times \exp(-310/T)$	Burkholder *et al.* [181]
$HBr + OH \longrightarrow Br + H_2O$	$5.5 \times 10^{-12} \times \exp(200/T)$	Burkholder *et al.* [181]
$BrO + NO \longrightarrow Br + NO_2$	$8.8 \times 10^{-12} \times \exp(260/T)$	Burkholder *et al.* [181]
$BrO + BrO \longrightarrow 2\,Br + O_2$	$2.4 \times 10^{-12} \times \exp(40/T)$	Burkholder *et al.* [181]
$BrO + BrO \longrightarrow Br_2 + O_2$	$2.8 \times 10^{-12} \times \exp(860/T)$	Burkholder *et al.* [181]
$Br + CH_3CHO \longrightarrow HBr + CH_3CO$	$1.8 \times 10^{-11} \times \exp(-460/T)$	Atkinson *et al.* (2006) [182]
$Br + HCHO \longrightarrow HBr + HCO$	$7.7 \times 10^{-12} \times \exp(-580/T)$	Atkinson *et al.* (2006) [182]
$BrO + IO \longrightarrow Br + OIO$	$1.5 \times 10^{-11} \times \exp(510/T) \times 0.8$	Atkinson *et al.* (2007) [183]
$BrO + IO \longrightarrow Br + I$	$1.5 \times 10^{-11} \times \exp(510/T) \times 0.2$	Atkinson *et al.* (2007) [183]
$I + HO_2 \longrightarrow HI + O_2$	$1.5 \times 10^{-11} \times \exp(-1090/T)$	Burkholder *et al.* [181]
$HI + OH \longrightarrow I + H_2O$	3.0×10^{-11}	Burkholder *et al.* [181]
$IO + NO \longrightarrow I + NO_2$	$8.6 \times 10^{-12} \times \exp(230/T)$	Burkholder *et al.* [181]
$I + O_3 \longrightarrow IO + O_2$	$2.0 \times 10^{-11} \times \exp(-830/T)$	Burkholder *et al.* [181]
$IO + HO_2 \longrightarrow HOI + O_2$	$1.4 \times 10^{-11} \times \exp(540/T)$	Atkinson *et al.* (2007) [183]
$HOI + OH \longrightarrow IO + H_2O$	5.0×10^{-12}	Riffault *et al.* [184]
$IO + IO \longrightarrow I + OIO$	$5.4 \times 10^{-11} \times \exp(180/T) \times 0.38$	Atkinson *et al.* (2007) [183]
$IO + IO \longrightarrow I_2O_2$	$5.4 \times 10^{-11} \times \exp(180/T) \times 0.62$	Atkinson *et al.* (2007) [183]
$IONO_2 + M \longrightarrow IO + NO_2 + M$	$1.1 \times 10^{15} \times \exp(12060/T)$	Atkinson *et al.* (2007) [183]
$OIO + OIO \longrightarrow$ products	1.5×10^{-10}	Gomez *et al.* [185]
$IO + OIO \longrightarrow$ products	1.5×10^{-10}	Gomez *et al.* [185]

Table B.4: Termolecular reaction mechanisms added to the MCM.

Reaction	$\mathbf{n = (1 + \log_{10}(k_0 \times [M]/k_\infty))^2)^{-1}}$ $\mathbf{k = (k_0[M]/(1 + k_0[M]/k_\infty)) \times 0.6^n}$	**Reference**
$OH + OH + M \longrightarrow H_2O_2 + M$	$k_0 = 6.9 \times 10^{-31} \times (T/298)^{-1}$ $k_\infty = 2.6 \times 10^{-11}$	Burkholder *et al.* [181]
$BrO + NO_2 + M \longrightarrow BrONO_2 + M$	$k_0 = 5.5 \times 10^{-31} \times (T/298)^{-3.1}$ $k_\infty = 6.6 \times 10^{-11} \times (T/298)^{-2.9}$	Burkholder *et al.* [181]
$Br + NO_2 + M \longrightarrow BrNO_2 + M$	$k_0 = 4.3 \times 10^{-31} \times (T/298)^{-2.4}$ $k_\infty = 2.7 \times 10^{-11}$	Burkholder *et al.* [181]
$IO + NO_2 + M \longrightarrow IONO_2 + M$	$k_0 = 7.7 \times 10^{-31} \times (T/298)^{-3.5}$ $k_\infty = 7.7 \times 10^{-12} \times (T/298)^{-1.5}$	Burkholder *et al.* [181]

Bibliography

[1] *WMO confirms 2024 as warmest year on record at about 1.55°C above pre-industrial level*. URL: https://wmo.int/news/media-centre/wmo-confirms-2024-warmest-year-record-about-155degc-above-pre-industrial-level (visited on 04/09/2025).

[2] Intergovernmental Panel on Climate Change. *Climate Change 2023: Synthesis Report. Contribution of Working Groups I, II and III to the Sixth Assessment Report of the Intergovernmental Panel on Climate Change*. Ed. by H. Lee and J. Romero. Geneva, Switzerland, 2023. DOI: 10.59327/IPCC/AR6-9789291691647.

[3] *Wildfires and Climate Change*. URL: https://science.nasa.gov/wildfires-and-climate-change/ (visited on 04/09/2025).

[4] *Extreme weather: floods, droughts and heatwaves*. URL: https://www.eea.europa.eu/en/topics/in-depth/extreme-weather-floods-droughts-and-heatwaves (visited on 04/09/2025).

[5] World Health Organization. *WHO Global Air Quality Guidelines. Particulate Matter (PM2.5 and PM10), Ozone, Nitrogen Dioxide, Sulfur Dioxide and Carbon Monoxide*. Tech. rep. Licence: CC BY-NC-SA 3.0 IGO. Geneva: World Health Organization, 2021.

[6] World Health Organization. *Review of evidence on health aspects of air pollution - REVIHAAP Project*. Tech. rep. World Health Organization, 2013.

[7] *National Oceanic and Atmospheric Administration*. URL: https://www.noaa.gov/jetstream/atmosphere/layers-of-atmosphere (visited on 04/22/2025).

[8] D. J. Jacobs. *Introduction to atmospheric chemsitry*. Princeton University Press, 1999.

[9] M. J. Molina and F. S. Rowland. “Stratospheric sink for chlorofluoromethanes: chlorine atom catalysed destruction of ozone”. *Nature* 249 (1974). DOI: doi.org/10.1038/249810a0.

[10] J. Lelieveld, J. S. Evans, M. Fnais, D. Giannadaki, and A. Pozzer. “The contribution of outdoor air pollution sources to premature mortality on a global scale”. *Nature* 525 (2015), pp. 367–371. DOI: 10.1038/nature15371.

[11] S. Chapman. “On ozone and atomic oxygen in the upper atmosphere”. *The London, Edinburgh, and Dublin Philosophical Magazine and Journal of Science* 10 (1930), pp. 369–383. DOI: 10.1080/14786443009461588.

[12] J. E. Lovelock. “Atmospheric halocarbons and stratospheric ozone”. *Nature* 252 (1974), pp. 292–294. DOI: doi.org/10.1038/252292a0.

[13] P. J. Crutzen. “The influence of nitrogen oxides on the atmospheric ozone content”. *Quarterly Journal of the Royal Meteorological Society* 96 (1970), pp. 320–325. DOI: 10.1002/qj.49709640815.

[14] *UN Environment Programme: About the Montreal protocol*. URL: https://www.unep.org/ozonaction/who-we-are/about-montreal-protocol (visited on 04/10/2025).

[15] B. J. Finlayson-Pitts and J. N. Pitts Jr. *Chemistry of the Upper and Lower Atmosphere*. San Diego: Academic Press, 2000. DOI: 10.1016/B978-0-12-257060-5.X5000-X.

[16] D. W. Tarasick, T. K. Carey-Smith, W. K. Hocking, O. Moeini, H. He, J. Liu, M. K. Osman, A. M. Thompson, B. J. Johnson, S. J. Oltmans, and J. T. Merrill. “Quantifying stratosphere-troposphere transport of ozone using balloon-borne ozonesondes, radar windprofilers and trajectory models”. *Atmospheric Environment* 198 (2019), pp. 496–509. DOI: 10.1016/j.atmosenv.2018.10.040.

[17] S. Sillman. “The relation between ozone, NOx and hydrocarbons in urban and polluted rural environments”. *Atmospheric Environment* 33 (1999), pp. 1821–1845.

[18] J. D. Lee, S. J. Moller, K. A. Read, A. C. Lewis, L. Mendes, and L. J. Carpenter. “Year-round measurements of nitrogen oxides and ozone in the tropical North Atlantic marine boundary layer”. *Journal of Geophysical Research Atmospheres* 114 (2009). DOI: 10.1029/2009JD011878.

[19] Z. H. Beygi, H. Fischer, H. D. Harder, M. Martinez, R. Sander, J. Williams, D. M. Brookes, P. S. Monks, and J. Lelieveld. "Oxidation photochemistry in the Southern Atlantic boundary layer: Unexpected deviations of photochemical steady state". *Atmospheric Chemistry and Physics* 11 (2011), pp. 8497–8513. DOI: 10.5194/acp-11-8497-2011.

[20] S. Tiwari, A. Dahiya, and N. Kumar. "Investigation into relationships among NO, NO2, NOx, O3, and CO at an urban background site in Delhi, India". *Atmospheric Research* 157 (2015), pp. 119–126. DOI: 10.1016/j.atmosres.2015.01.008.

[21] K. Vellingiri, K. H. Kim, J. Y. Jeon, R. J. Brown, and M. C. Jung. "Changes in NOx and O3 concentrations over a decade at a central urban area of Seoul, Korea". *Atmospheric Environment* 112 (2015), pp. 116–125. DOI: 10.1016/j.atmosenv.2015.04.032.

[22] M. Xie, K. Zhu, T. Wang, P. Chen, Y. Han, S. Li, B. Zhuang, and L. Shu. "Temporal characterization and regional contribution to O 3 and NO x at an urban and a suburban site in Nanjing, China". *Science of the Total Environment* 551-552 (2016), pp. 533–545. DOI: 10.1016/j.scitotenv.2016.02.047.

[23] J. A. Logan. "Tropospheric ozone: Seasonal behavior, trends, and anthropogenic influence". *Journal of Geophysical Research: Atmospheres* 90 (1985), pp. 10463–10482. DOI: 10.1029/JD090iD06p10463.

[24] R. Atkinson. "Atmospheric chemistry of VOCs and NOx". *Atmospheric Environment* 34 (2000), pp. 2063–2101. DOI: 10.1016/S1352-2310(99)00460-4. URL: https://linkinghub.elsevier.com/retrieve/pii/S1352231099004604.

[25] K. A. Read, A. S. Mahajan, L. J. Carpenter, M. J. Evans, B. V. Faria, D. E. Heard, J. R. Hopkins, J. D. Lee, S. J. Moller, A. C. Lewis, L. Mendes, J. B. McQuaid, H. Oetjen, A. Saiz-Lopez, M. J. Pilling, and J. M. Plane. "Extensive halogen-mediated ozone destruction over the tropical Atlantic Ocean". *Nature* 453 (2008), pp. 1232–1235. DOI: 10.1038/nature07035.

[26] R. Sommariva, W. J. Bloss, N. Brough, N. Carslaw, M. Flynn, A.-L. Haggerstone, D. E. Heard, J. R. Hopkins, J. D. Lee, A. C. Lewis, G. McFiggans, P. S. Monks, S. A. Penkett, M. J. Pilling, J. M. C. Plane, K. A. Read, A. Saiz-Lopez, A. R. Rickard, and P. I. Williams. "OH

and HO2 chemistry during NAMBLEX: roles of oxygenates, halogen oxides and heterogeneous uptake". *Atmospheric Chemistry and Physics* 6 (2006), pp. 1135–1153. DOI: 10.5194/acp-6-1135-2006. URL: https://acp.copernicus.org/articles/6/1135/2006/.

[27] L. K. Whalley, K. L. Furneaux, A. Goddard, J. D. Lee, A. Mahajan, H. Oetjen, K. A. Read, N. Kaaden, L. J. Carpenter, A. C. Lewis, J. M. C. Plane, E. S. Saltzman, A. Wiedensohler, and D. E. Heard. "The chemistry of OH and HO 2 radicals in the boundary layer over the tropical Atlantic Ocean". *Atmos. Chem. Phys* 10 (2010), pp. 1555–1576. URL: www.atmos-chem-phys.net/10/1555/2010/.

[28] J. S. Levine, T. R. Augustsson, I. C. Andersont, J. M. Hoell, and D. A. Brewer. "Tropospheric sources of NOx: Lightning and biology". *Atmospheric Environment (1967)* 18 (1984), pp. 1797–1804. DOI: 10.1016/0004-6981(84)90355-X.

[29] L. W. Horowitz and D. J. Jacob. "Global impact of fossil fuel combustion on atmospheric NOx". *Journal of Geophysical Research Atmospheres* 104 (1999), pp. 23823–23840. DOI: 10.1029/1999JD900205.

[30] M. Val Martín, R. E. Honrath, R. C. Owen, G. Pfister, P. Fialho, and F. Barata. "Significant enhancements of nitrogen oxides, black carbon, and ozone in the North Atlantic lower free troposphere resulting from North American boreal wildfires". *Journal of Geophysical Research Atmospheres* 111 (2006). DOI: 10.1029/2006JD007530.

[31] M. Galanter, H. Levy, and G. R. Carmichael. "Impacts of biomass burning on tropospheric CO, NOx, and O3". *Journal of Geophysical Research Atmospheres* 105 (2000), pp. 6633–6653. DOI: 10.1029/1999JD901113.

[32] S. Solomon, D. Qin, M. Manning, Z. Chen, M. Marquis, K. Averyt, M. Tignor, and H. Miller, eds. *Climate Change 2007: The Physical Science Basis. Contribution of Working Group I to the Fourth Assessment Report of the Intergovernmental Panel on Climate Change*. Cambridge, United Kingdom and New York, NY, USA: Cambridge University Press, 2007, p. 996.

[33] C. Granier, B. Bessagnet, T. Bond, A. D'Angiola, H. D. van der Gon, G. J. Frost, A. Heil, J. W. Kaiser, S. Kinne, Z. Klimont, S. Kloster, J. F. Lamarque, C. Liousse, T. Masui, F. Meleux, A. Mieville, T. Ohara, J. C. Raut, K. Riahi, M. G. Schultz, S. J. Smith, A. Thompson, J. van Aardenne,

G. R. van der Werf, and D. P. van Vuuren. “Evolution of anthropogenic and biomass burning emissions of air pollutants at global and regional scales during the 1980–2010 period”. *Climatic Change* 109 (2011), pp. 163–190. DOI: 10.1007/s10584-011-0154-1.

[34] V. Masson-Delmotte, P. Zhai, A. Pirani, S. Connors, C. Péan, S. Berger, N. Caud, Y. Chen, L. Goldfarb, M. Gomis, M. Huang, K. Leitzell, E. Lonnoy, J. Matthews, T. Maycock, T. Waterfield, O. Yelekçi, R. Yu, and B. Zhou, eds. *Climate Change 2021: The Physical Science Basis. Contribution of Working Group I to the Sixth Assessment Report of the Intergovernmental Panel on Climate Change*. Cambridge, United Kingdom and New York, NY, USA: Cambridge University Press, p. 2391. DOI: 10.1017/9781009157896.

[35] K. Miyazaki, H. Eskes, K. Sudo, K. Folkert Boersma, K. Bowman, and Y. Kanaya. “Decadal changes in global surface NOx emissions from multi-constituent satellite data assimilation”. *Atmospheric Chemistry and Physics* 17 (2017), pp. 807–837. DOI: 10.5194/acp-17-807-2017.

[36] B. A. Nault, J. L. Laughner, P. J. Wooldridge, J. D. Crounse, J. Dibb, G. Diskin, J. Peischl, J. R. Podolske, I. B. Pollack, T. B. Ryerson, E. Scheuer, P. O. Wennberg, and R. C. Cohen. “Lightning NOx Emissions: Reconciling Measured and Modeled Estimates With Updated NOx Chemistry”. *Geophysical Research Letters* 44 (2017), pp. 9479–9488. DOI: 10.1002/2017GL074436.

[37] L. T. Murray. “Lightning NO x and Impacts on Air Quality”. *Current Pollution Reports* 2 (2016), pp. 115–133. DOI: 10.1007/s40726-016-0031-7. URL: http://link.springer.com/10.1007/s40726-016-0031-7.

[38] U. Schumann and H. Huntrieser. “The global lightning-induced nitrogen oxides source”. *Atmospheric Chemistry and Physics* 7 (2007), pp. 3823–3907. DOI: 10.5194/acp-7-3823-2007. URL: https://acp.copernicus.org/articles/7/3823/2007/.

[39] K. Hui, Y. Yuan, B. Xi, and W. Tan. *A review of the factors affecting the emission of the ozone chemical precursors VOCs and NOx from the soil*. 2023. DOI: 10.1016/j.envint.2023.107799.

[40] L. Jaeglé, L. Steinberger, R. V. Martin, and K. Chance. “Global partitioning of NOx sources using satellite observations: Relative roles of fossil fuel combustion, biomass burning and soil emissions”. *Faraday Discussions* 130 (2005), pp. 407–423. DOI: 10.1039/b502128f. URL: https://xlink.rsc.org/?DOI=b502128f.

[41] G. C. Vinken, K. F. Boersma, J. D. Maasakkers, M. Adon, and R. V. Martin. “Worldwide biogenic soil NOx emissions inferred from OMI NO2 observations”. *Atmospheric Chemistry and Physics* 14 (2014), pp. 10363–10381. DOI: 10.5194/acp-14-10363-2014.

[42] A. K. Georgoulias, R. A. Van Der, P. Stammes, K. Folkert Boersma, and H. J. Eskes. “Trends and trend reversal detection in 2 decades of tropospheric NO2 satellite observations”. *Atmospheric Chemistry and Physics* 19 (2019), pp. 6269–6294. DOI: 10.5194/acp-19-6269-2019.

[43] W. Yi, X. Wang, T. He, H. Liu, Z. Luo, Z. Lv, and K. He. “The high-resolution global shipping emission inventory by the Shipping Emission Inventory Model (SEIM)”. *Earth System Science Data* 17 (2025), pp. 277–292. DOI: 10.5194/essd-17-277-2025. URL: https://essd.copernicus.org/articles/17/277/2025/.

[44] O. C. Zafiriou and M. McFarland. “Nitric oxide from nitrite photolysis in the central equatorial Pacific”. *Science* 86 (1981), pp. 3173–3182. DOI: 10.1029/JC086iC04p03173. URL: https://agupubs.onlinelibrary.wiley.com/doi/10.1029/JC086iC04p03173.

[45] C. Y. Liu, W. H. Feng, Y. Tian, G. P. Yang, P. F. Li, and H. W. Bange. “Determination of dissolved nitric oxide in coastal waters of the Yellow Sea off Qingdao”. *Ocean Science* 13 (2017), pp. 623–632. DOI: 10.5194/os-13-623-2017.

[46] Y. Tian, G. P. Yang, C. Y. Liu, P. F. Li, H. T. Chen, and H. W. Bange. “Photoproduction of nitric oxide in seawater”. *Ocean Science* 16 (2020), pp. 135–148. DOI: 10.5194/os-16-135-2020.

[47] H. B. Singh, L. J. Salas, and W. Viezee. “Global distribution of peroxyacetyl nitrate”. *Nature* 321 (1986), pp. 588–591. DOI: 10.1038/321588a0. URL: https://www.nature.com/articles/321588a0.

[48] I. Bridier, F. Caralp, H. Loirat, R. Lesclaux, B. Veyret, K. H. Becker, A. Reimer, and F. Zabel. "Kinetic and theoretical studies of the reactions acetylperoxy + nitrogen dioxide + M .dblarw. acetyl peroxynitrate + M between 248 and 393 K and between 30 and 760 torr". *The Journal of Physical Chemistry* 95 (1991), pp. 3594–3600. DOI: 10.1021/j100162a031. URL: https://pubs.acs.org/doi/abs/10.1021/j100162a031.

[49] S. M. Kane, F. Caloz, and M. T. Leu. "Heterogeneous uptake of gaseous N2O5 by (NH4)2SO4, NH4HSO4, and H2SO4 aerosols". *Journal of Physical Chemistry A* 105 (2001), pp. 6465–6470. DOI: 10.1021/jp010490x.

[50] T. Stavrakou, J. F. Müller, K. F. Boersma, R. J. Van Der A., J. Kurokawa, T. Ohara, and Q. Zhang. "Key chemical NOx sink uncertainties and how they influence top-down emissions of nitrogen oxides". *Atmospheric Chemistry and Physics* 13 (2013), pp. 9057–9082. DOI: 10.5194/acp-13-9057-2013.

[51] C. Ye, X. Zhou, D. Pu, J. Stutz, J. Festa, M. Spolaor, C. Tsai, C. Cantrell, R. L. Mauldin, T. Campos, A. Weinheimer, R. S. Hornbrook, E. C. Apel, A. Guenther, L. Kaser, B. Yuan, T. Karl, J. Haggerty, S. Hall, K. Ullmann, J. N. Smith, J. Ortega, and C. Knote. "Rapid cycling of reactive nitrogen in the marine boundary layer". *Nature* 532 (2016), pp. 489–491. DOI: 10.1038/nature17195.

[52] N. L. Ng, S. S. Brown, A. T. Archibald, E. Atlas, R. C. Cohen, J. N. Crowley, D. A. Day, N. M. Donahue, J. L. Fry, H. Fuchs, R. J. Griffin, M. I. Guzman, H. Herrmann, A. Hodzic, Y. Iinuma, J. L. Jimenez, A. Kiendler-Scharr, B. H. Lee, D. J. Luecken, J. Mao, R. McLaren, A. Mutzel, H. D. Osthoff, B. Ouyang, B. Picquet-Varrault, U. Platt, H. O. T. Pye, Y. Rudich, R. H. Schwantes, M. Shiraiwa, J. Stutz, J. A. Thornton, A. Tilgner, B. J. Williams, and R. A. Zaveri. "Nitrate radicals and biogenic volatile organic compounds: oxidation, mechanisms, and organic aerosol". *Atmospheric Chemistry and Physics* 17 (2017), pp. 2103–2162. DOI: 10.5194/acp-17-2103-2017. URL: https://acp.copernicus.org/articles/17/2103/2017/.

[53] U. Platt, D. Perner, and H. W. Pätz. "Simultaneous measurement of atmospheric CH2O, O3, and NO2 by differential optical absorption". *Journal of Geophysical Research: Oceans* 84 (1979), pp. 6329–6335. DOI: 10.1029/JC084iC10p06329.

[54] A. Fontijn, A. J. Sabadell, and R. J. Ronco. “Homogeneous chemiluminescent measurement of nitric oxide with ozone”. *Analytical Chemistry* 42 (1970), pp. 575–579.

[55] S. Penkett, S. Gilge, C. Plass-Deulmer, I. Galbally, N. Brough, J. Bottenheim, F. Flocke, H. Gerwig, J. Lee, M. Milton, F. Rohrer, T. Ryerson, M. Steinbacher, K. Torseth, and R. Wieglosz. “WMO/GAW Expert Workshop on Global Long-term Measurements of Nitrogen Oxides and Recommendiations for GAW Nitrogen Oxides Network”. *GAW Report 195*. Geneva, Switzerland: World Meteorological Organization (WMO), 2011.

[56] S. Reimann, R. Wegener, A. Claude, and S. Sauvage. *Updated Measurement Guideline for NOx and VOCs*. Tech. rep. ACTRIS, 2018.

[57] H. D. Osthoff, S. S. Brown, T. B. Ryerson, T. J. Fortin, B. M. Lerner, E. J. Williams, A. Pettersson, T. Baynard, W. P. Dubé, S. J. Ciciora, and A. R. Ravishankara. “Measurement of atmospheric NO2 by pulsed cavity ring-down spectroscopy”. *Journal of Geophysical Research: Atmospheres* 111 (2006). DOI: 10.1029/2005JD006942. URL: https://agupubs.onlinelibrary.wiley.com/doi/10.1029/2005JD006942.

[58] A. O’Keefe and D. A. G. Deacon. “Cavity ring-down optical spectrometer for absorption measurements using pulsed laser sources”. *Review of Scientific Instruments* 59 (1988), pp. 2544–2551. DOI: 10.1063/1.1139895. URL: https://pubs.aip.org/rsi/article/59/12/2544/313248/Cavity-ring-down-optical-spectrometer-for.

[59] A. W. Rollins, P. S. Rickly, R. S. Gao, T. B. Ryerson, S. S. Brown, J. Peischl, and I. Bourgeois. “Single-photon laser-induced fluorescence detection of nitric oxide at sub-parts-per-trillion mixing ratios”. *Atmospheric Measurement Techniques* 13 (2020), pp. 2425–2439. DOI: 10.5194/amt-13-2425-2020.

[60] J. A. Thornton, P. J. Wooldridge, and R. C. Cohen. “Atmospheric NO2: In Situ laser-induced fluorescence detection at parts per trillion mixing ratios”. *Analytical Chemistry* 72 (2000), pp. 528–539. DOI: 10.1021/ac9908905.

[61] B. Tuzson, K. Zeyer, M. Steinbacher, J. B. McManus, D. D. Nelson, M. S. Zahniser, and L. Emmenegger. "Selective measurements of NO, NO2 and NOy in the free troposphere using quantum cascade laser spectroscopy". *Atmospheric Measurement Techniques* 6 (2013), pp. 927–936. DOI: 10.5194/amt-6-927-2013. URL: https://amt.copernicus.org/articles/6/927/2013/.

[62] A. A. Kosterev, A. L. Malinovsky, F. K. Tittel, C. Gmachl, F. Capasso, D. L. Sivco, J. N. Baillargeon, A. L. Hutchinson, and A. Y. Cho. "Cavity ringdown spectroscopic detection of nitric oxide with a continuous-wave quantum-cascade laser". *Applied Optics* 40 (2001), p. 5522. DOI: 10.1364/AO.40.005522.

[63] L. J. Carpenter, Z. L. Fleming, K. A. Read, J. D. Lee, S. J. Moller, J. R. Hopkins, R. M. Purvis, A. C. Lewis, K. Müller, B. Heinold, H. Herrmann, K. W. Fomba, D. Van Pinxteren, C. Müller, I. Tegen, A. Wiedensohler, T. Müller, N. Niedermeier, E. P. Achterberg, M. D. Patey, E. A. Kozlova, M. Heimann, D. E. Heard, J. M. Plane, A. Mahajan, H. Oetjen, T. Ingham, D. Stone, L. K. Whalley, M. J. Evans, M. J. Pilling, R. J. Leigh, P. S. Monks, A. Karunaharan, S. Vaughan, S. R. Arnold, J. Tschritter, D. Pöhler, U. Frieß, R. Holla, L. M. Mendes, H. Lopez, B. Faria, A. J. Manning, and D. W. Wallace. "Seasonal characteristics of tropical marine boundary layer air measured at the Cape Verde Atmospheric Observatory". *Journal of Atmospheric Chemistry* 67 (2010), pp. 87–140. DOI: 10.1007/s10874-011-9206-1.

[64] *World Data Centre for Reactive Gases (WDCRG)*. URL: https://www.gaw-wdcrg.org (visited on 04/07/2025).

[65] *World Data Centre for Greenhouse Gases (WDCGG)*. URL: https://gaw.kishou.go.jp (visited on 04/07/2025).

[66] C. Reed, M. J. Evans, L. R. Crilley, W. J. Bloss, T. Sherwen, K. A. Read, J. D. Lee, and L. J. Carpenter. "Evidence for renoxification in the tropical marine boundary layer". *Atmospheric Chemistry and Physics* 17 (2017), pp. 4081–4092. DOI: 10.5194/acp-17-4081-2017.

[67] S. T. Andersen, L. J. Carpenter, B. S. Nelson, L. Neves, K. A. Read, C. Reed, M. Ward, M. J. Rowlinson, and J. D. Lee. "Long-Term NOx measurements in the remote marine tropical troposphere". *Atmospheric*

Measurement Techniques 14 (2021), pp. 3071–3085. DOI: 10.5194/amt-14-3071-2021.

[68] S. T. Andersen, B. S. Nelson, K. A. Read, S. Punjabi, L. Neves, M. J. Rowlinson, J. Hopkins, T. Sherwen, L. K. Whalley, J. D. Lee, and L. J. Carpenter. "Fundamental oxidation processes in the remote marine atmosphere investigated using the NO-NO2-O3 photostationary state". *Atmospheric Chemistry and Physics* 22 (2022), pp. 15747–15765. DOI: 10.5194/acp-22-15747-2022.

[69] R. E. Davis, B. P. Hayden, D. A. Gay, W. L. Phillips, and G. V. Jones. "The North Atlantic Subtropical Anticyclone". *Journal of Climate* 10 (1997), pp. 728–744. DOI: 10.1175/1520-0442(1997)010<0728:TNASA>2.0.CO;2. URL: http://journals.ametsoc.org/doi/10.1175/1520-0442(1997)010%3C0728:TNASA%3E2.0.CO;2.

[70] C. Zellweger, M. Steinbacher, and B. Buchmann. "Evaluation of new laser spectrometer techniques for in-situ carbon monoxide measurements". *Atmospheric Measurement Techniques* 5 (2012), pp. 2555–2567. DOI: 10.5194/amt-5-2555-2012. URL: https://amt.copernicus.org/articles/5/2555/2012/.

[71] C. Zellweger, L. Emmenegger, M. Firdaus, J. Hatakka, M. Heimann, E. Kozlova, T. G. Spain, M. Steinbacher, M. V. van der Schoot, and B. Buchmann. "Assessment of recent advances in measurement techniques for atmospheric carbon dioxide and methane observations". *Atmospheric Measurement Techniques* 9 (2016), pp. 4737–4757. DOI: 10.5194/amt-9-4737-2016.

[72] R. Steinbrecher. *System and performance audit for non-methane volatile organic compounds: global GAW station - Cape Verde Atmospheric Observatory, Calhau, Cape Verde*. Tech. rep. WMO World Calibration Centre for VOC, Karlsruhe Institute of Technology, KIT/IMK-IFU, Garmisch-Partenkirchen, Germany, 2019.

[73] C. Reed, M. J. Evans, P. Di Carlo, J. D. Lee, and L. J. Carpenter. "Interferences in photolytic NO2 measurements: Explanation for an apparent missing oxidant?" *Atmospheric Chemistry and Physics* 16 (2016), pp. 4707–4724. DOI: 10.5194/acp-16-4707-2016.

[74] I. B. Pollack, B. M. Lerner, and T. B. Ryerson. "Evaluation of ultraviolet light-emitting diodes for detection of atmospheric NO2 by photolysis - chemiluminescence". *Journal of Atmospheric Chemistry* 65 (2010), pp. 111–125. DOI: 10.1007/s10874-011-9184-3. URL: http://link.springer.com/10.1007/s10874-011-9184-3.

[75] M. C. Peterson and R. E. Honrath. "NOx and NOy over the northwestern North Atlantic: Measurements and measurement accuracy". *Journal of Geophysical Research: Atmospheres* 104 (1999), pp. 11695–11707. DOI: 10.1029/1998JD100088. URL: https://agupubs.onlinelibrary.wiley.com/doi/10.1029/1998JD100088.

[76] B. Ridley and F. Grahek. "A small, low flow, high sensitivity reaction vessel for NO chemiluminescence detectors". *J. Atmos. Ocean. Tech.* 7 (1990), pp. 307–311. DOI: 10.1175/1520-0426.

[77] *JASMIN*. URL: https://jasmin.ac.uk (visited on 08/12/2024).

[78] D. Sivia and J. Skilling. *Data Analysis: A Bayesian Tutorial*. Oxford, United Kingdom: Oxford University Press, p. 2391. DOI: 10.1017/9781009157896.

[79] L. J. Gras and M. Keywood. "Cloud condensation nuclei over the Southern Ocean: Wind dependence and seasonal cycles". *Atmospheric Chemistry and Physics* 17 (2017), pp. 4419–4432. DOI: 10.5194/acp-17-4419-2017.

[80] R. S. Humphries, M. D. Keywood, J. P. Ward, J. Harnwell, S. P. Alexander, A. R. Klekociuk, K. Hara, I. M. Mcrobert, A. Protat, J. Alroe, L. T. Cravigan, B. Miljevic, Z. D. Ristovski, R. Schofield, S. R. Wilson, C. J. Flynn, G. R. Kulkarni, G. G. Mace, G. M. Mcfarquhar, S. D. Chambers, A. G. Williams, and A. D. Griffiths. "Measurement report: Understanding the seasonal cycle of Southern Ocean aerosols". *Atmospheric Chemistry and Physics* 23 (2023), pp. 3749–3777. DOI: 10.5194/acp-23-3749-2023.

[81] G. Mace, R. Marchand, M. Keywood, A. Protat, R. Humphries, S. Fiddes, C. Mccluskey, S. Siems, Y. Huang, P. May, and P.-L. Ma. *Cloud and Precipitation Experiment at Kennaook (Cape-K) Science Plan*. Tech. rep. 2023.

[82] I. Galbally. "Nitrogen Oxides (NO, NO_2, NO_y) measurements at Cape Grim: A technical manual". *Baseline Atmospheric Program (Australia): Technical Series*. Ed. by N. Derek, P. Krummel, and S. Cleland. Australian Bureau of Meteorology, CSIRO Oceans, and Atmosphere: Melbourne Australia, 2020, pp. 1–111. URL: https://doi.org/10.25919/dt6y-3q53.

[83] S. D. Chambers, A. G. Williams, F. Conen, A. D. Griffiths, S. Reimann, M. Steinbacher, P. B. Krummel, L. P. Steele, M. V. van der Schoot, I. E. Galbally, S. B. Molloy, and J. E. Barnes. "Towards a universal "Baseline" characterisation of air masses for high- and low-altitude observing stations using Radon-222". *Aerosol and Air Quality Research* 16 (2016), pp. 885–899. DOI: 10.4209/aaqr.2015.06.0391.

[84] M. H. Wilkening and W. E. Clements. "Radon 222 from the ocean surface". *Journal of Geophysical Research* 80 (1975), pp. 3828–3830. DOI: 10.1029/JC080i027p03828.

[85] S. Molloy and I. Galbally. "Analysis and Identification of a Suitable Baseline Definition of Tropospheric Ozone at Cape Grim, Tasmania". *Baseline Atmospheric Program Australia 2009-2010*. Ed. by N. Derek, P. Krummel, and S. Cleland. Australian Bureau of Meteorology, CSIRO Marine, and Atmospheric Research, 2014, pp. 7–16.

[86] P. Leighton. *Photochemistry of Air Pollution*. Oxford: Elsevier Science, 1961.

[87] K. Mannschreck, S. Gilge, C. Plass-Duelmer, W. Fricke, and H. Berresheim. *Atmospheric Chemistry and Physics Assessment of the applicability of NO-NO 2-O 3 photostationary state to long-term measurements at the Hohenpeissenberg GAW Station, Germany*. Tech. rep. 2004, pp. 1265–1277. URL: www.atmos-chem-phys.org/acp/4/1265/.

[88] M. M. Frey, N. Brough, J. L. France, P. S. Anderson, O. Traulle, M. D. King, A. E. Jones, E. W. Wolff, and J. Savarino. "The diurnal variability of atmospheric nitrogen oxides (NO and NO 2) above the Antarctic Plateau driven by atmospheric stability and snow emissions". *Atmospheric Chemistry and Physics* 13 (2013), pp. 3045–3062. DOI: 10.5194/acp-13-3045-2013.

[89] M. M. Frey, H. K. Roscoe, A. Kukui, J. Savarino, J. L. France, M. D. King, M. Legrand, and S. Preunkert. "Atmospheric nitrogen oxides (NO and NO2) at Dome C, East Antarctica, during the OPALE campaign". *Atmospheric Chemistry and Physics* 15 (2015), pp. 7859–7875. DOI: 10.5194/acp-15-7859-2015.

[90] L. K. Whalley, E. J. Slater, R. Woodward-Massey, C. Ye, J. D. Lee, F. Squires, J. R. Hopkins, R. E. Dunmore, M. Shaw, J. F. Hamilton, A. C. Lewis, A. Mehra, S. D. Worrall, A. Bacak, T. J. Bannan, H. Coe, C. J. Percival, B. Ouyang, R. L. Jones, L. R. Crilley, L. J. Kramer, W. J. Bloss, T. Vu, S. Kotthaus, S. Grimmond, Y. Sun, W. Xu, S. Yue, L. Ren, W. Joe, C. Nicholas Hewitt, X. Wang, P. Fu, and D. E. Heard. "Evaluating the sensitivity of radical chemistry and ozone formation to ambient VOCs and NOx in Beijing". *Atmospheric Chemistry and Physics* 21 (2021), pp. 2125–2147. DOI: 10.5194/acp-21-2125-2021.

[91] C. A. Cantrell, R. E. Shetter, J. G. Calvert, F. L. Eisele, E. Williams, K. Baumann, W. H. Brune, P. S. Stevens, and J. H. Mather. "Peroxy radicals from photostationary state deviations and steady state calculations during the Tropospheric OH Photochemistry Experiment at Idaho Hill, Colorado, 1993". *Journal of Geophysical Research Atmospheres* 102 (1997), pp. 6369–6378. DOI: 10.1029/96jd01703.

[92] I. Tadic, J. N. Crowley, D. Dienhart, P. Eger, H. Harder, B. Hottmann, M. Martinez, U. Parchatka, J. D. Pari, A. Pozzer, R. Rohloff, J. Schuladen, J. Shenolikar, S. Tauer, J. Lelieveld, and H. Fischer. "Net ozone production and its relationship to nitrogen oxides and volatile organic compounds in the marine boundary layer around the Arabian Peninsula". *Atmospheric Chemistry and Physics* 20 (2020), pp. 6769–6787. DOI: 10.5194/acp-20-6769-2020.

[93] P. S. Monks, L. J. Carpenter, S. A. Penkett, G. P. Ayers, R. W. Gillett, I. E. Galbally, and M. Meyer. *Fundamental ozone photochemistry in the remote marine boundary layer: the SOAPEX experiment, measurement and theory*. Tech. rep. 1998, pp. 3647–3664.

[94] D. Stone, L. K. Whalley, and D. E. Heard. "Tropospheric OH and HO2 radicals: Field measurements and model comparisons". *Chemical Society Reviews* 41 (2012), pp. 6348–6404. DOI: 10.1039/c2cs35140d.

[95] X. Yang, Y. Li, X. Ma, Z. Tan, K. Lu, and Y. Zhang. *Unclassical Radical Generation Mechanisms in the Troposphere: A Review*. 2024. DOI: 10.1021/acs.est.4c00742.

[96] X. Yang, H. Wang, K. Lu, X. Ma, Z. Tan, B. Long, X. Chen, C. Li, T. Zhai, Y. Li, K. Qu, Y. Xia, Y. Zhang, X. Li, S. Chen, H. Dong, L. Zeng, and Y. Zhang. "Reactive aldehyde chemistry explains the missing source of hydroxyl radicals". *Nature Communications* 15 (2024). DOI: 10.1038/s41467-024-45885-w.

[97] G. Chen, X. Fan, S. Yu, Y. J. Tham, Z. Lin, X. Ji, L. Xu, and J. Chen. "HOCl Formation Driven by Photochemical Processes Enhanced Atmospheric Oxidation Capacity in a Coastal Atmosphere". *Environmental Science & Technology* 59 (2025), pp. 5164–5171. DOI: 10.1021/acs.est.5c01363. URL: https://pubs.acs.org/doi/10.1021/acs.est.5c01363.

[98] M. J. Lawler, R. Sander, L. J. Carpenter, J. D. Lee, R. Von Glasow, R. Sommariva, and E. S. Saltzman. "HOCl and Cl2 observations in marine air". *Atmospheric Chemistry and Physics* 11 (2011), pp. 7617–7628. DOI: 10.5194/acp-11-7617-2011.

[99] M. M. van Herpen, Q. Li, A. Saiz-Lopez, J. B. Liisberg, T. Röckmann, C. A. Cuevas, R. P. Fernandez, J. E. Mak, N. M. Mahowald, P. Hess, D. Meidan, J. B. W. Stuut, and M. S. Johnson. "Photocatalytic chlorine atom production on mineral dust–sea spray aerosols over the North Atlantic". *Proceedings of the National Academy of Sciences of the United States of America* 120 (2023). DOI: 10.1073/PNAS.2303974120.

[100] *MCM photolysis parameters*. URL: https://mcm.york.ac.uk/MCM/rates/photolysis (visited on 01/22/2025).

[101] B. Bohn, D. E. Heard, N. Mihalopoulos, C. Plass-Dülmer, R. Schmitt, and L. K. Whalley. "Characterisation and improvement of j(O1D) filter radiometers". *Atmospheric Measurement Techniques* 9 (2016), pp. 3455–3466. DOI: 10.5194/amt-9-3455-2016.

[102] A. S. Mahajan, J. M. Plane, H. Oetjen, L. Mendes, R. W. Saunders, A. Saiz-Lopez, C. E. Jones, L. J. Carpenter, and G. B. McFiggans. "Measurement and modelling of tropospheric reactive halogen species over the tropical

Atlantic Ocean". *Atmospheric Chemistry and Physics* 10 (2010), pp. 4611–4624. DOI: 10.5194/acp-10-4611-2010.

[103] S. J. Seldon. "Advancing our understanding of peroxy radical chemistry in the atmosphere". PhD thesis. University of Leeds, 2025.

[104] T. M. Hard, R. J. O, C. Y. Chan, and A. A. Mehrabzadeh. "Tropospheric Free Radical Determination by FAGE". *Environ. Sci. Technol* 18 (1984). URL: https://pubs.acs.org/sharingguidelines.

[105] H. Fuchs, F. Holland, and A. Hofzumahaus. "Measurement of tropospheric R O2 and HO2 radicals by a laser-induced fluorescence instrument". *Review of Scientific Instruments* 79 (2008). DOI: 10.1063/1.2968712.

[106] M. E. Jenkin, J. C. Young, and A. R. Rickard. "The MCM v3.3.1 degradation scheme for isoprene". *Atmospheric Chemistry and Physics* 15 (2015), pp. 11433–11459. DOI: 10.5194/acp-15-11433-2015.

[107] R. Sommariva, S. Cox, C. Martin, K. Borońska, J. Young, P. K. Jimack, M. J. Pilling, V. N. Matthaios, B. S. Nelson, M. J. Newland, M. Panagi, W. J. Bloss, P. S. Monks, and A. R. Rickard. "AtChem (version 1), an open-source box model for the Master Chemical Mechanism". *Geoscientific Model Development* 13 (2020), pp. 169–183. DOI: 10.5194/gmd-13-169-2020.

[108] L. Saha, A. Kumar, S. Kumar, J. Korstad, S. Srivastava, and K. Bauddh. "The impact of the COVID-19 lockdown on global air quality: A review". *Environmental Sustainability* 5 (2022), pp. 5–23. DOI: 10.1007/s42398-021-00213-6.

[109] Z. S. Venter, K. Aunan, S. Chowdhury, and J. Lelieveld. "COVID-19 lockdowns cause global air pollution declines". *PNAS* 117 (2020). DOI: 10.1073/pnas.2006853117/-/DCSupplemental. URL: https://www.pnas.org.

[110] L. Menut, B. Bessagnet, G. Siour, S. Mailler, R. Pennel, and A. Cholakian. "Impact of lockdown measures to combat Covid-19 on air quality over western Europe". *Science of the Total Environment* 741 (2020). DOI: 10.1016/j.scitotenv.2020.140426.

[111] M. G. Adam, P. T. Tran, and R. Balasubramanian. *Air quality changes in cities during the COVID-19 lockdown: A critical review*. 2021. DOI: 10.1016/j.atmosres.2021.105823.

[112] O. G. Fawole, N. Yusuf, L. A. Sunmonu, A. Obafaye, D. K. Audu, L. Onuorah, C. F. Olusegun, A. Deme, and H. Senghor. "Impacts of COVID-19 Restrictions on Regional and Local Air Quality Across Selected West African Cities". *GeoHealth* 6 (2022). DOI: 10.1029/2022GH000597.

[113] T. Doumbia, C. Granier, N. Elguindi, I. Bouarar, S. Darras, G. Brasseur, B. Gaubert, Y. Liu, X. Shi, T. Stavrakou, S. Tilmes, F. Lacey, A. Deroubaix, and T. Wang. "Changes in global air pollutant emissions during the COVID-19 pandemic: A dataset for atmospheric modeling". *Earth System Science Data* 13 (2021), pp. 4191–4206. DOI: 10.5194/essd-13-4191-2021.

[114] Z. Han, Y. Zhang, Z. Liu, K. Zhang, Z. Wang, B. Luo, L. Xue, and X. Wang. "The impact of COVID-19 lockdown on surface air quality changes in major African countries". *EGUsphere [preprint]* (2024). DOI: 10.5194/egusphere-2024-2951. URL: https://egusphere.copernicus.org/preprints/2024/egusphere-2024-2951/.

[115] M. Kganyago and L. Shikwambana. "Did covid-19 lockdown restrictions have an impact on biomass burning emissions in sub-saharan africa?" *Aerosol and Air Quality Research* 21 (2021). DOI: 10.4209/aaqr.2020.07.0470.

[116] *NASA Air Quality Observations from Space*. URL: https://airquality.gsfc.nasa.gov/no2/world?field_region_target_id=90 (visited on 03/19/2025).

[117] D. J. Stewart, C. M. Taylor, C. E. Reeves, and J. B. Mcquaid. *Biogenic nitrogen oxide emissions from soils: impact on NO x and ozone over west Africa during AMMA (African Monsoon Multidisciplinary Analysis): observational study*. Tech. rep. 2008, pp. 2285–2297. URL: www.atmos-chem-phys.net/8/2285/2008/.

[118] C. Delon, C. E. Reeves, D. J. Stewart, D. Serça, R. Dupont, C. Mari, J.-P. Chaboureau, and P. Tulet. *Biogenic nitrogen oxide emissions from soils-impact on NO x and ozone over West Africa during AMMA (African Monsoon*

Multidisciplinary Experiment): modelling study. Tech. rep. 2008, pp. 2351–2363. URL: www.atmos-chem-phys.net/8/2351/2008/.

[119] Y. Wen, W. Xiaotong, H. Tingkun, L. Huan, L. Zhenyu, and H. Kebin. *Global shipping emissions for the years 2013 and 2016-2021 [Data set]*. 2024. DOI: https://doi.org/10.5281/zenodo.11069531.

[120] S. N. Sirimanne, R. Asariotis, M. Assaf, C. Bacrot, H. Benamara, L. R. Flour, P. Hansen, J. Hoffmann, O. Hoffmeister, T. Kulaga, L. Rodriguez, C. Struempfler, H. Tokuda, and F. Youssef. *Review of maritime transport 2024*. Tech. rep. United Nations Publications, New York, USA, 2024.

[121] R. Atkinson, D. L. Baulch, R. A. Cox, J. N. Crowley, R. F. Hampson, R. G. Hynes, M. E. Jenkin, M. J. Rossi, and J. Troe. *Atmospheric Chemistry and Physics Evaluated kinetic and photochemical data for atmospheric chemistry: Volume I - gas phase reactions of Ox, HOx, NOx and SOx species*. Tech. rep. 2004, pp. 1461–1738. URL: www.atmos-chem-phys.org/acp/4/1461/.

[122] D. E. Shallcross, K. E. Leather, A. Bacak, P. Xiao, E. P. Lee, M. Ng, D. K. Mok, J. M. Dyke, R. Hossaini, M. P. Chipperfield, M. A. H. Khan, and C. J. Percival. "Reaction between CH3O2 and BrO radicals: A new source of upper troposphere lower stratosphere hydroxyl radicals". *Journal of Physical Chemistry A* 119 (2015), pp. 4618–4632. DOI: 10.1021/jp5108203.

[123] S. Enami, T. Yamanaka, S. Hashimoto, M. Kawasaki, Y. Nakano, and T. Ishiwata. "Kinetic study of IO radical with RO2 (R = CH3, C 2H5, and CF3) using cavity ring-down spectroscopy". *Journal of Physical Chemistry A* 110 (2006), pp. 9861–9866. DOI: 10.1021/jp0619336.

[124] T. J. Dillon, M. E. Tucceri, and J. N. Crowley. "Laser induced fluorescence studies of iodine oxide chemistry: Part II. The reactions of IO with CH3O2, CF3O2 and O3". *Physical Chemistry Chemical Physics* 8 (2006), pp. 5185–5198. DOI: 10.1039/b611116e.

[125] P. Kasibhatla, T. Sherwen, M. J. Evans, L. J. Carpenter, C. Reed, B. Alexander, Q. Chen, M. P. Sulprizio, J. D. Lee, K. A. Read, W. Bloss, L. R. Crilley, W. C. Keene, A. A. Pszenny, and A. Hodzic. "Global impact of nitrate photolysis in sea-salt aerosol on NOx, OH, and O3 in the marine boundary layer". *Atmospheric Chemistry and Physics* 18 (2018), pp. 11185–11203. DOI: 10.5194/acp-18-11185-2018.

[126] F. Spataro and A. Ianniello. *Sources of atmospheric nitrous acid: State of the science, current research needs, and future prospects*. 2014. DOI: 10.1080/10962247.2014.952846.

[127] J. Kleffmann. *Daytime sources of nitrous acid (HONO) in the atmospheric boundary layer*. 2007. DOI: 10.1002/cphc.200700016.

[128] J. Wang, Y. Zhang, C. Zhang, Y. Wang, J. Zhou, L. K. Whalley, E. J. Slater, J. E. Dyson, W. Xu, P. Cheng, B. Han, L. Wang, X. Yu, Y. Wang, R. Woodward-Massey, W. Lin, W. Zhao, L. Zeng, Z. Ma, D. E. Heard, and C. Ye. "Validating HONO as an Intermediate Tracer of the External Cycling of Reactive Nitrogen in the Background Atmosphere". *Environmental Science and Technology* 57 (2023), pp. 5474–5484. DOI: 10.1021/acs.est.2c06731.

[129] C. Ye, D. E. Heard, and L. K. Whalley. "Evaluation of Novel Routes for NOx Formation in Remote Regions". *Environmental Science and Technology* 51 (2017), pp. 7442–7449. DOI: 10.1021/acs.est.6b06441.

[130] J. E. Dyson, G. A. Boustead, L. T. Fleming, M. Blitz, D. Stone, S. R. Arnold, L. K. Whalley, and D. E. Heard. "Production of HONO from NO2 uptake on illuminated TiO2 aerosol particles and following the illumination of mixed TiO2/ammonium nitrate particles". *Atmospheric Chemistry and Physics* 21 (2021), pp. 5755–5775. DOI: 10.5194/acp-21-5755-2021.

[131] Z. Liu, Y. Wang, F. Costabile, A. Amoroso, C. Zhao, L. G. Huey, R. Stickel, J. Liao, and T. Zhu. "Evidence of aerosols as a media for rapid daytime HONO production over China". *Environmental Science and Technology* 48 (2014), pp. 14386–14391. DOI: 10.1021/es504163z.

[132] Y. Dupart, L. Fine, B. D'Anna, and C. George. "Heterogeneous uptake of NO2 on Arizona Test Dust under UV-A irradiation: An aerosol flow tube study". *Aeolian Research* 15 (2014), pp. 45–51. DOI: 10.1016/j.aeolia.2013.10.001.

[133] V. Michoud, A. Colomb, A. Borbon, K. Miet, M. Beekmann, M. Camredon, B. Aumont, S. Perrier, P. Zapf, G. Siour, W. Ait-Helal, C. Afif, A. Kukui, M. Furger, J. C. Dupont, M. Haeffelin, and J. F. Doussin. "Study of the unknown HONO daytime source at a European suburban site during the MEGAPOLI summer and winter field campaigns". *Atmospheric*

Chemistry and Physics 14 (2014), pp. 2805–2822. DOI: 10.5194/acp-14-2805-2014.

[134] H. Meusel, U. Kuhn, A. Reiffs, C. Mallik, H. Harder, M. Martinez, J. Schuladen, B. Bohn, U. Parchatka, J. N. Crowley, H. Fischer, L. Tomsche, A. Novelli, T. Hoffmann, R. H. Janssen, O. Hartogensis, M. Pikridas, M. Vrekoussis, E. Bourtsoukidis, B. Weber, J. Lelieveld, J. Williams, U. Pöschl, Y. Cheng, and H. Su. "Daytime formation of nitrous acid at a coastal remote site in Cyprus indicating a common ground source of atmospheric HONO and NO". *Atmospheric Chemistry and Physics* 16 (2016), pp. 14475–14493. DOI: 10.5194/acp-16-14475-2016.

[135] M. Sörgel, E. Regelin, H. Bozem, J. M. Diesch, F. Drewnick, H. Fischer, H. Harder, A. Held, Z. Hosaynali-Beygi, M. Martinez, and C. Zetzsch. *Quantification of the unknown HONO daytime source and its relation to NO2*. 2011. DOI: 10.5194/acp-11-10433-2011.

[136] S. T. Andersen, L. J. Carpenter, C. Reed, J. D. Lee, R. Chance, T. Sherwen, A. R. Vaughan, J. Stewart, P. M. Edwards, W. J. Bloss, R. Sommariva, L. R. Crilley, G. J. Nott, L. Neves, K. Read, D. E. Heard, P. W. Seakins, L. K. Whalley, G. A. Boustead, L. T. Fleming, D. Stone, and K. W. Fomba. "Extensive field evidence for the release of HONO from the photolysis of nitrate aerosols". *Science Advances* 9 (2023). DOI: 10.1126/sciadv.add6266.

[137] C. Ye, N. Zhang, H. Gao, and X. Zhou. "Photolysis of Particulate Nitrate as a Source of HONO and NOx". *Environmental Science and Technology* 51 (2017), pp. 6849–6856. DOI: 10.1021/acs.est.7b00387.

[138] Y. Zhu, Y. Wang, X. Zhou, Y. F. Elshorbany, C. Ye, M. Hayden, and A. J. Peters. "An investigation into the chemistry of HONO in the marine boundary layer at Tudor Hill Marine Atmospheric Observatory in Bermuda". *Atmospheric Chemistry and Physics* 22 (2022), pp. 6327–6346. DOI: 10.5194/acp-22-6327-2022.

[139] K. B. Benedict, A. S. McFall, and C. Anastasio. "Quantum Yield of Nitrite from the Photolysis of Aqueous Nitrate above 300 nm". *Environmental Science and Technology* 51 (2017), pp. 4387–4395. DOI: 10.1021/acs.est.6b06370.

[140] M. Gen, Z. Liang, R. Zhang, B. R. Go Mabato, and C. K. Chan. *Particulate nitrate photolysis in the atmosphere*. 2022. DOI: 10.1039/d1ea00087j.

[141] C. Ye, H. Gao, N. Zhang, and X. Zhou. "Photolysis of Nitric Acid and Nitrate on Natural and Artificial Surfaces". *Environmental Science and Technology* 50 (2016), pp. 3530–3536. DOI: 10.1021/acs.est.5b05032.

[142] X. Zhou, H. Gao, Y. He, G. Huang, S. B. Bertman, K. Civerolo, and J. Schwab. "Nitric acid photolysis on surfaces in low-NOx environments: Significant atmospheric implications". *Geophysical Research Letters* 30 (2003). DOI: 10.1029/2003GL018620.

[143] J. Du and L. Zhu. "Quantification of the absorption cross sections of surface-adsorbed nitric acid in the 335-365 nm region by Brewster angle cavity ring-down spectroscopy". *Chemical Physics Letters* 511 (2011), pp. 213–218. DOI: 10.1016/j.cplett.2011.06.062.

[144] C. Zhu, B. Xiang, L. Zhu, and R. Cole. "Determination of absorption cross sections of surface-adsorbed HNO3 in the 290-330 nm region by Brewster angle cavity ring-down spectroscopy". *Chemical Physics Letters* 458 (2008), pp. 373–377. DOI: 10.1016/j.cplett.2008.04.125.

[145] P. S. Romer, P. J. Wooldridge, J. D. Crounse, M. J. Kim, P. O. Wennberg, J. E. Dibb, E. Scheuer, D. R. Blake, S. Meinardi, A. L. Brosius, A. B. Thames, D. O. Miller, W. H. Brune, S. R. Hall, T. B. Ryerson, and R. C. Cohen. "Constraints on Aerosol Nitrate Photolysis as a Potential Source of HONO and NO x". *Environmental Science and Technology* 52 (2018), pp. 13738–13746. DOI: 10.1021/acs.est.8b03861.

[146] Q. Shi, Y. Tao, J. E. Krechmer, C. L. Heald, J. G. Murphy, J. H. Kroll, and Q. Ye. "Laboratory Investigation of Renoxification from the Photolysis of Inorganic Particulate Nitrate". *Environmental Science and Technology* 55 (2021), pp. 854–861. DOI: 10.1021/acs.est.0c06049.

[147] F. Bao, M. Li, Y. Zhang, C. Chen, and J. Zhao. "Photochemical Aging of Beijing Urban PM2.5: HONO Production". *Environmental Science and Technology* 52 (2018), pp. 6309–6316. DOI: 10.1021/acs.est.8b00538.

[148] Y. Jiang, M. Xia, L. Xue, X. Wang, X. Zhong, Y. Liu, M. Kulmala, T. Ma, J. Wang, Y. Wang, J. Gao, and T. Wang. "Quantifying HONO Production from Nitrate Photolysis in a Polluted Atmosphere". *Envi-*

ronmental Science & Technology (2024). DOI: 10.1021/acs.est.4c06061. URL: https://pubs.acs.org/doi/10.1021/acs.est.4c06061.

[149] H. Jiang, F. Bao, J. Wang, J. Chen, Y. Zhu, D. Huang, C. Chen, and J. Zhao. "Direct Formation of Electronic Excited NO2 Contributes to the High Yield of HONO during Photosensitized Renoxification". *Environmental Science and Technology* 57 (2023), pp. 11144–11151. DOI: 10.1021/acs.est.3c01342.

[150] S. Jin, L. Kong, K. Yang, C. Wang, L. Xia, Y. Wang, J. Tan, and L. Wang. "Combined effects of high relative humidity and ultraviolet irradiation: Enhancing the production of gaseous NO2 from the photolysis of NH4NO3". *Science of the Total Environment* 838 (2022). DOI: 10.1016/j.scitotenv.2022.156480.

[151] Q. Li, S. Ma, Y. Liu, X. Wu, H. Fu, X. Tu, S. Yan, L. Zhang, C. George, and J. Chen. "Phase State Regulates Photochemical HONO Production from NaNO3/Dicarboxylic Acid Mixtures". *Environmental Science and Technology* 58 (2024), pp. 7516–7528. DOI: 10.1021/acs.est.3c10980.

[152] N. K. Scharko, A. E. Berke, and J. D. Raff. "Release of nitrous acid and nitrogen dioxide from nitrate photolysis in acidic aqueous solutions". *Environmental Science and Technology* 48 (2014), pp. 11991–12001. DOI: 10.1021/es503088x.

[153] R. Sommariva, M. S. Alam, L. R. Crilley, D. J. Rooney, W. J. Bloss, K. W. Fomba, S. T. Andersen, and L. J. Carpenter. "Factors Influencing the Formation of Nitrous Acid from Photolysis of Particulate Nitrate". *Journal of Physical Chemistry A* 127 (2023), pp. 9302–9310. DOI: 10.1021/acs.jpca.3c03853.

[154] L. M. Wingen, A. C. Moskun, S. N. Johnson, J. L. Thomas, M. Roeselová, D. J. Tobias, M. T. Kleinman, and B. J. Finlayson-Pitts. "Enhanced surface photochemistry in chloride-nitrate ion mixtures". *Physical Chemistry Chemical Physics* 10 (2008), pp. 5668–5677. DOI: 10.1039/b806613b.

[155] P. Nissenson, D. Dabdub, R. Das, V. Maurino, C. Minero, and D. Vione. "Evidence of the water-cage effect on the photolysis of NO3- and FeOH2+. Implications of this effect and of H2O2 surface accumulation on photochemistry at the air-water interface of atmospheric droplets". *Atmospheric*

Environment 44 (2010), pp. 4859–4866. DOI: 10.1016/j.atmosenv.2010.08.035.

[156] C. Zhu, B. Xiang, L. T. Chu, and L. Zhu. "308 nm photolysis of nitric acid in the gas phase, on aluminum surfaces, and on ice films". *Journal of Physical Chemistry A* 114 (2010), pp. 2561–2568. DOI: 10.1021/jp909867a.

[157] P. Salvador, J. E. Curtis, D. J. Tobias, and P. Jungwirth. "Polarizability of the nitrate anion and its solvation at the air/water interface". *Physical Chemistry Chemical Physics* 5 (2003), pp. 3752–3757. DOI: 10.1039/b304537d.

[158] L. X. Dang, T. M. Chang, M. Roeselova, B. C. Garrett, and D. J. Tobias. "On NO3- - H2 O interactions in aqueous solutions and at interfaces". *Journal of Chemical Physics* 124 (2006). DOI: 10.1063/1.2171375.

[159] N. K. Richards, L. M. Wingen, K. M. Callahan, N. Nishino, M. T. Kleinman, D. J. Tobias, and B. J. Finlayson-Pitts. "Nitrate ion photolysis in thin water films in the presence of bromide ions". *Journal of Physical Chemistry A* 115 (2011), pp. 5810–5821. DOI: 10.1021/jp109560j.

[160] N. K. Richards and B. J. Finlayson-Pitts. "Production of gas phase NO2 and halogens from the photochemical oxidation of aqueous mixtures of sea salt and nitrate ions at room temperature". *Environmental Science and Technology* 46 (2012), pp. 10447–10454. DOI: 10.1021/es300607c.

[161] W. Hua, D. Verreault, and H. C. Allen. "Surface electric fields of aqueous solutions of NH4NO3, Mg(NO3)2, NaNO3, and LiNO3: Implications for atmospheric aerosol chemistry". *Journal of Physical Chemistry C* 118 (2014), pp. 24941–24949. DOI: 10.1021/jp505770t.

[162] A. C. Hong, S. N. Wren, and D. J. Donaldson. "Enhanced surface partitioning of nitrate anion in aqueous bromide solutions". *Journal of Physical Chemistry Letters* 4 (2013), pp. 2994–2998. DOI: 10.1021/jz4015772.

[163] L. R. Crilley, L. J. Kramer, F. D. Pope, C. Reed, J. D. Lee, L. J. Carpenter, L. D. Hollis, S. M. Ball, and W. J. Bloss. "Is the ocean surface a source of nitrous acid (HONO) in the marine boundary layer?" *Atmospheric Chemistry and Physics* 21 (2021), pp. 18213–18225. DOI: 10.5194/acp-21-18213-2021.

[164] J. Heland, J. Kleffmann, R. Kurtenbach, and P. Wiesen. "A new instrument to measure gaseous nitrous acid (HONO) in the atmosphere". *Environmental Science and Technology* 35 (2001), pp. 3207–3212. DOI: 10.1021/es000303t.

[165] K. Grasshoff, M. Ehrhardt, and K. Kremling. *Methods of Seawater Analysis*. Third. Weinheim: Wiley-VCH, 1983.

[166] J. Kleffmann and P. Wiesen. *Atmospheric Chemistry and Physics Technical Note: Quantification of interferences of wet chemical HONO LOPAP measurements under simulated polar conditions*. Tech. rep. 2008, pp. 6813–6822. URL: www.atmos-chem-phys.net/8/6813/2008/.

[167] J. Kleffman, J. Heland, R. Kurtenbach, J. Lörzer, and P. Wiesen. "A new instrument (LOPAP) for the detection of nitrous acid (HONO)". *Environmental Science and Pollution Research* (2002), pp. 48–54.

[168] K. W. Fomba, K. Müller, D. Van Pinxteren, L. Poulain, M. Van Pinxteren, and H. Herrmann. "Long-term chemical characterization of tropical and marine aerosols at the Cape Verde Atmospheric Observatory (CVAO) from 2007 to 2011". *Atmospheric Chemistry and Physics* 14 (2014), pp. 8883–8904. DOI: 10.5194/acp-14-8883-2014.

[169] Y. Jiang, E. H. Hoffmann, A. Tilgner, M. B. Aiyuk, S. T. Andersen, L. Wen, M. van Pinxteren, H. Shen, L. Xue, W. Wang, and H. Herrmann. "Insights Into NOx and HONO Chemistry in the Tropical Marine Boundary Layer at Cape Verde During the MarParCloud Campaign". *Journal of Geophysical Research: Atmospheres* 128 (2023). DOI: 10.1029/2023JD038865.

[170] M. Ndour, P. Conchon, B. D'Anna, O. Ka, and C. George. "Photochemistry of mineral dust surface as a potential atmospheric renoxification process". *Geophysical Research Letters* 36 (2009). DOI: 10.1029/2008GL036662.

[171] L. R. Crilley, L. J. Kramer, B. Ouyang, J. Duan, W. Zhang, S. Tong, M. Ge, K. Tang, M. Qin, P. Xie, M. D. Shaw, A. C. Lewis, A. Mehra, T. J. Bannan, S. D. Worrall, M. Priestley, A. Bacak, H. Coe, J. Allan, C. J. Percival, O. A. Popoola, R. L. Jones, and W. J. Bloss. "Intercomparison of nitrous acid (HONO) measurement techniques in a megacity (Beijing)".

Atmospheric Measurement Techniques 12 (2019), pp. 6449–6463. DOI: 10.5194/amt-12-6449-2019.

[172] J. P. Pinto, J. Dibb, B. H. Lee, B. Rappenglück, E. C. Wood, M. Levy, R. Y. Zhang, B. Lefer, X. R. Ren, J. Stutz, C. Tsai, L. Ackermann, J. Golovko, S. C. Herndon, M. Oakes, Q. Y. Meng, J. W. Munger, M. Zahniser, and J. Zheng. "Intercomparison of field measurements of nitrous acid (HONO) during the SHARP campaign". *Journal of Geophysical Research* 119 (2014), pp. 5583–5601. DOI: 10.1002/2013JD020287.

[173] A. M. H. Bond, M. M. Frey, J. Kaiser, J. Kleffmann, A. E. Jones, and F. A. Squires. "Snowpack nitrate photolysis drives the summertime atmospheric nitrous acid (HONO) budget in coastal Antarctica". *Atmospheric Chemistry and Physics* 23 (2023), pp. 5533–5550. DOI: 10.5194/acp-23-5533-2023. URL: https://acp.copernicus.org/articles/23/5533/2023/.

[174] I. Bourgeois, J. Peischl, J. A. Neuman, S. S. Brown, H. M. Allen, P. Campuzano-Jost, M. M. Coggon, J. P. DiGangi, G. S. Diskin, J. B. Gilman, G. I. Gkatzelis, H. Guo, H. A. Halliday, T. F. Hanisco, C. D. Holmes, L. G. Huey, J. L. Jimenez, A. D. Lamplugh, Y. R. Lee, J. Lindaas, R. H. Moore, B. A. Nault, J. B. Nowak, D. Pagonis, P. S. Rickly, M. A. Robinson, A. W. Rollins, V. Selimovic, J. M. St. Clair, D. Tanner, K. T. Vasquez, P. R. Veres, C. Warneke, P. O. Wennberg, R. A. Washenfelder, E. B. Wiggins, C. C. Womack, L. Xu, K. J. Zarzana, and T. B. Ryerson. "Comparison of airborne measurements of NO, NO2, HONO, NOy, and CO during FIREX-AQ". *Atmospheric Measurement Techniques* 15 (2022), pp. 4901–4930. DOI: 10.5194/amt-15-4901-2022.

[175] X. Li, F. Rohrer, A. Hofzumahaus, T. Brauers, R. Häseler, B. Bohn, S. Broch, H. Fuchs, S. Gomm, F. Holland, J. Jäger, J. Kaiser, F. N. Keutsch, I. Lohse, K. Lu, R. Tillmann, R. Wegener, G. M. Wolfe, T. F. Mentel, A. Kiendler-Scharr, and A. Wahner. "Missing Gas-Phase Source of HONO Inferred from Zeppelin Measurements in the Troposphere". *Science* 344 (2014), pp. 292–296. DOI: 10.1126/science.1248999. URL: https://www.science.org/doi/10.1126/science.1248999.

[176] C. Ye, X. Zhou, D. Pu, J. Stutz, J. Festa, M. Spolaor, C. Cantrell, R. L. Mauldin, A. Weinheimer, and J. Haggerty. "Comment on "Missing gas-phase source of HONO inferred from Zeppelin measurements in the troposphere"". *Science* 348 (2015), pp. 1326–1326. DOI: 10.1126/science.

aaa1992. URL: https://www.science.org/doi/10.1126/science.aaa1992.

[177] T. J. Dillon and J. N. Crowley. "Reactive quenching of electronically excited NO2 and NO3 by H2O as potential sources of atmospheric HOx radicals". *Atmospheric Chemistry and Physics* 18 (2018), pp. 14005–14015. DOI: 10.5194/acp-18-14005-2018. URL: https://acp.copernicus.org/articles/18/14005/2018/.

[178] M. Song, X. Zhao, P. Liu, J. Mu, G. He, C. Zhang, S. Tong, C. Xue, X. Zhao, M. Ge, and Y. Mu. "Atmospheric NOx oxidation as major sources for nitrous acid (HONO)". *npj Climate and Atmospheric Science* 6 (2023), p. 30. DOI: 10.1038/s41612-023-00357-8. URL: https://www.nature.com/articles/s41612-023-00357-8.

[179] S. Ma, Q. Li, and Y. Zhang. "A comprehensive study on hygroscopic behaviour and nitrate depletion of NaNO3 and dicarboxylic acid mixtures: implications for nitrate depletion in tropospheric aerosols". *Atmospheric Chemistry and Physics* 22 (2022), pp. 10955–10970. DOI: 10.5194/acp-22-10955-2022.

[180] J. J. Orlando and G. S. Tyndall. "Rate Coefficients for the Thermal Decomposition of BrONO2 and the Heat of Formation of BrONO2". *The Journal of Physical Chemistry* 100 (1996), pp. 19398–19405. DOI: 10.1021/jp9620274.

[181] J. Burkholder, S. Sander, J. Abbatt, J. Barker, C. Cappa, J. Crounse, T. Dibble, R. Huie, C. Kolb, M. Kurylo, V. Orkin, C. Percival, D. Wilmouth, and P. Wine. *Chemical Kinetics and Photochemical Data for Use in Atmospheric Studies. Evaluation No. 19*. Tech. rep. Pasadena: Jet Propulsion Laboratory, 2019.

[182] R. Atkinson, D. L. Baulch, R. A. Cox, J. N. Crowley, R. F. Hampson, R. G. Hynes, M. E. Jenkin, M. J. Rossi, and J. Troe. "Evaluated kinetic and photochemical data for atmospheric chemistry: Volume II – gas phase reactions of organic species". *Atmospheric Chemistry and Physics* 6 (2006), pp. 3625–4055. DOI: 10.5194/acp-6-3625-2006.

[183] R. Atkinson, D. L. Baulch, R. A. Cox, J. N. Crowley, R. F. Hampson, R. G. Hynes, M. E. Jenkin, M. J. Rossi, and J. Troe. "Evaluated kinetic and photochemical data for atmospheric chemistry: Volume III – gas

phase reactions of inorganic halogens". *Atmospheric Chemistry and Physics* 7 (2007), pp. 981–1191. DOI: 10.5194/acp-7-981-2007.

[184] V. Riffault, Y. Bedjanian, and G. Poulet. "Kinetic and mechanistic study of the reactions of OH with IBr and HOI". *Journal of Photochemistry and Photobiology A: Chemistry* 176 (2005), pp. 155–161. DOI: 10.1016/j.jphotochem.2005.09.002.

[185] J. C. Gómez Martín, P. Spietz, and J. P. Burrows. "Kinetic and Mechanistic Studies of the I2/O3 Photochemistry". *The Journal of Physical Chemistry A* 111 (2007), pp. 306–320. DOI: 10.1021/jp061186c.